AN ABSTRACT OF THE THESIS OF

Alison Arnold for the degree of Master of Science in Medical Physics presented on May 29, 2014.

Title: Precise Lateral Dose Profile Measurements of Surface Interfaces of Hip Prostheses.

Abstract approved: ____

Richard Crilly

With the growing incidence of total hip replacements performed each year in the United States, the incidence of patients with prosthesis requiring radiotherapy is bound to increase. It is necessary to understand and quantify the effects of the high atomic number material prostheses used in total hip replacements on therapeutic radiation therapy (RT), specifically the surface interface absorbed dose. In order to understand the effect this will have on the implant it is necessary to have an accurate measurement of dose to the tissue affected by the presence of the prosthesis. In this study, Gafchromic™ (Covington, KY) EBT3 film was employed in the measurement setup to gather the precise surface interface absorbed dose associated with specific high atomic number materials typically used in hip prostheses. The materials used were a 1” stainless steel (SS) rod, a ½” stainless steel rod, a 1” titanium (Ti) rod, a ½” titanium rod, a Tri Lock® (Warsaw, IN) hip stem with Gription® (Warsaw, IN) coating, and an Anatomical Medullary Locking® (AML®) (Warsaw, IN) hip stem with Porocoat® (Warsaw, IN) coating. The average relative surface interface dose values gathered were greater for the 6 MV beam photon than the 18 MV photon beam, and the profile shape changed slightly with the addition of the porous coatings used on the hip stems. The results of this study provide a dosimetric basis for analysis of radiation effects involving the porous coating of modern hip prostheses for the continued research into the radiobiological effect of high atomic number material prostheses in the body on RT.

Precise Lateral Dose Profile Measurements of Surface Interfaces of Hip Prostheses

by
Alison Arnold

A THESIS

submitted to

Oregon State University

in partial fulfillment of
the requirements for the
degree of

Master of Science

Presented May 29, 2014
Commencement June 2014

Master of Science thesis of Alison Arnold presented on May 29, 2014

APPROVED:

Major Professor, representing Medical Physics

Head of the Department of Nuclear Engineering and Radiation Health Physics

Dean of the Graduate School

I understand that my thesis will become part of the permanent collection of Oregon State University libraries. My signature below authorizes release of my thesis to any reader upon request.

Alison Arnold, Author

ACKNOWLEDGEMENTS

I would like to thank the many people in my life whose support, encourage, and advisement helped make this research possible.

First, I would like to thank my advisor Dr. Richard Crilly for his patience, guidance, and the opportunity to work on such a unique project. I would also like to thank Dr. Krystina Tack for her guidance and support throughout my time in the Medical Physics program. Additionally, I would like to acknowledge and thank Dr. Wolfram Laub and all of the physicists at OHSU for their efforts to ensure I have a well-developed understanding of the theory and clinical practice of Medical Physics.

I would also like to thank Manfred Dittrich of the Oregon State University machine shop for his skills in wonderfully preparing the solid rods for experimental use and advice regarding my materials. I would like to acknowledge and thank DePuy Synthes for providing hip stems for my research. The hip stems provided a unique opportunity to investigate the effects of the structurally unique designs incorporated into prostheses. Thank you to Rickard Engineering Design for your skills with the precision water jet cutter in preparing the hip stems beautifully for experimental use.

I am forever grateful for the support and encouragement of my parents and family in my academic pursuits. To my fellow medical physics students, I will always appreciate the camaraderie and the many hours shared together pursuing this degree. Last, but not least, I would like to thank Joshua Graves for dealing with the brunt of my frustrations, stress, and fears throughout graduate school. Your constant support, love, and baked goods helped me stay sane and grounded.

TABLE OF CONTENTS

TABLE OF CONTENTS (Continued)

LIST OF FIGURES

LIST OF FIGURES (Continued)

LIST OF FIGURES (Continued)

LIST OF FIGURES (Continued)

LIST OF FIGURES (Continued)

LIST OF TABLES

APPENDIX

1. Introduction

According to the Center for Disease Control and Prevention (CDC), approximately 332,000 total hip replacements are performed each year ((CDC) 2010). The rate of total hip replacements performed each year increased 25% between 2000 and 2009 (Holzwarth and Cotogno 2012). This increasing trend is expected to continue in the coming years with a growing incidence of total hip replacements performed on patients younger than 65 (Lange, Briggs et al. 2014).

Hip prostheses are composed of different materials. Some are composed of a titanium alloy while others are a Co-Cr-Mo alloy. Hip prostheses have also been composed of stainless steel. Often, modern hip prostheses include a porous coating along the hip stem to encourage new bony growth into the prosthetic instead of cement.

Typically, patients undergoing a total hip replacement, or total hip arthroplasty (THA), will receive prophylactic radiation therapy to prevent heterotopic ossification (HO). HO is defined as the "process by which trabecular bone forms outside of the skeletal structure, occupying space in soft tissue where it does not normally exist" (Baird and Kang 2009). If HO occurs and is symptomatic, it commonly causes decreased range of motion of the hip and pain while in severe cases complete bony ankylosis may occur (Balboni, Gobezie et al. 2006).

Coventry et al. established that radiation therapy could be used to successfully prevent HO (Coventry and Scanlon 1981). Several studies have been performed to determine the necessary dose, fraction, and time frame of radiation delivery for successful prevention of HO in patients undergoing THA (Cooley and Goss 1958, Craven and Urist 1971, Coventry and Scanlon 1981, Lo, Healy et al. 1988, Sylvester, Greenberg et al. 1988, Kantorowitz, Miller et al. 1990, Pellegrini, Konski et al. 1992, Healy, Lo et al. 1995, Kolbl, Knelles et al. 1997, Seegenschmiedt, Keilholz et al. 1997, Childs, Cole et al. 2000, Seegenschmiedt, Makoski et al. 2001, Balboni, Gobezie et al. 2006, Chao, Lee et al.

2006, Balboni, Gaccione et al. 2007). It has been shown that prophylactic radiation therapy can be delivered pre-operatively (less than 4 hours before surgery) or post-operatively (less than 72 hours post-op). Typically fractionation and dose prescriptions for prophylactic radiation therapy are a single fraction of 7-8 Gy. At OHSU, prophylactic radiation therapy is employed post-operatively in a single fraction of 7 Gy.

With the growing incidence of total hip replacements performed each year in the United States, the incidence of patients with prosthesis requiring radiotherapy is bound to increase. Current treatment delivery types and dose calculation algorithms are limited in their capabilities, and hip prostheses used in THA push the boundaries of these limitations.

Hip prostheses introduce interface effects. Interface effects are the perturbation of radiation deposition volumes by the introduction of an inhomogeneity. These effects occur in the body between any interface between tissue and materials of greater atomic number (Z) than tissue. The high atomic number of hip prostheses increases the interface effects along with an increase in photoelectric effect and pair production interactions. The dose perturbations along a hip prosthesis in radiation therapy depend upon the incident photon energy, differences in the photon energy transfer coefficients, the atomic number, the mass density and thickness of the prosthesis, and the differences in multiple scatter of the secondary electrons (Reft, Alecu et al. 2003).

Current treatment planning systems apply methods to account for the interface effects as long as the composition of the prosthetic is known and the CT number to electron density conversion curve is suitable (Reft, Alecu et al. 2003). Treatment planning systems (TPS) often have an upper limit on the electron density used for heterogeneity corrections in the TPS dose calculation algorithm which may result in an inaccurate calculated dose distribution around the prosthesis. Studies have been performed to compare and evaluate the different types of dose calculation algorithms in the presence of a hip prosthesis (Eng

2000, Ding and Yu 2001, Keall, Siebers et al. 2003, Laub and Nusslin 2003). Monte Carlo methods are currently the most accurate dose calculation algorithm near high atomic number materials but are not yet clinically available. While Monte Carlo remains the most accurate method, the porous coating on hip prostheses is not modeled because of the challenges presented by its non-uniform shape and density. In therapeutic radiation therapy treatment planning, it is important to accurately understand and predict the dose distribution to evaluate the capabilities of the treatment planning systems available.

Studies have been performed to quantify the dose perturbation along a hip prosthesis, such as *Eng*. *Eng* performed a study to determine the dose through a solid titanium alloy hip prosthesis using a scanning film dosimeter system (Eng 2000). The film dosimeter is less than ideal for close dosimetry due to its limited placement options. The scanning film dosimeter does not provide measurements right up next to the prosthesis.

While many dose calculation algorithm modeling has been performed to quantify the dose and dose perturbations along hip prostheses, *Eng* is one of the few studies that attempted to physically measure them. With the development of Gafchromic™ (Covington, KY) EBT3 radiochromic film, it is now easier to physically measure the dose and dose perturbation along prostheses.

Gafchromic™ EBT3 radiochromic film has many positive aspects including weak energy dependence, near tissue equivalence, high spatial resolution, small thickness, and wide dynamic range. Also, EBT3 film can be shot from any angle, handled in light, cut to size, bent to shape, and immersed in water. The EBT3 film will also be able to account for the porous coating used in hip prostheses because of the unique placement possibilities with EBT3 film. The film can be sandwiched through the hip stem making it possible to obtain the profile through the entire hip stem including the porous coating.

The purpose of this study is to determine the dose at the interface of hip prostheses and the associated lateral dose perturbations using Gafchromic™ EBT3 film with a high resolution at the surface interface. It is important to understand the biological effects of high atomic number materials in the body during radiation therapy. This study will not look at the biological effects, but it will provide an initial data set for future studies. EBT3 film measurements were taken with a variety of materials including a 1” stainless steel rod, a 1” titanium rod, a ½” stainless steel rod, a ½” titanium rod, a Tri Lock® (Warsaw, IN) hip stem from DePuy Synthes (titanium alloy), and an Anatomical Medullary Locking® (AML®) (Warsaw, IN) hip stem from DePuy Synthes (Co-Cr-Mo alloy).

2. Background

2.1.Basics

Therapeutic radiation therapy is concerned with the absorbed dose to the tumor or cancer cells. It is also concerned with the absorbed dose to the surrounding normal tissue cells within the treatment field. Absorbed dose is defined as the average energy imparted by ionizing radiation per unit mass of the irradiated material in units of Gray (Gy) or Rad (older term) (Khan 2003).

Radiation in medical treatments refers to ionizing radiation meaning the incident energy is high enough to remove an orbital electron from an atom. While this current work focuses on photon ionizing radiation, electron, proton, neutron, and alpha particles also induce ionizing radiation. Photon radiation can be broken into two sub-groups, gamma rays and x-rays. X-ray can be broken down further into two types, bremsstrahlung and characteristic x-rays. Bremsstrahlung arises from energetic electron interactions within the atomic nucleus of the target material. Bremsstrahlung results in a spectrum of energies based on the interaction distance between the electron and the nucleus. Characteristic x-rays are generated by interacting with the orbiting electron shells. Modern radiation therapy primarily utilizes linear accelerators to treat patients using megavoltage (MV) x-rays. There are five possible interactions the x-rays may undergo as the beam enters the patient. The five possible interactions are coherent scattering, photoelectric effect, Compton (incoherent) scattering, pair production, and photodisintegration. The three most common interaction types in MV therapeutic radiation therapy are photoelectric effect, Compton scatter, and pair production.

The photoelectric effect occurs predominantly at low energy x-rays (less than 1 MeV) and is more relevant in diagnostic radiology than radiation therapy (Washington 2010). The photoelectric effect involves a photon interaction with an atom and an ejection of an orbital electron. When an x-ray photon undergoes the photoelectric effect, all of its energy except the binding energy of the electron is transferred to the ejected electron (Khan 2003). With an electron ejected from the atom, another electron in another shell may drop energy to fill the vacancy left, resulting in the emission of a characteristic x-ray or mono-energetic Auger electron (Khan 2003). The probability of photoelectric effect interaction occurring is dependent of Z^3/E^3 where Z is the atomic number of the material and E is the energy of the incident photon (Khan 2003).

Compton (incoherent) scattering is the predominant interaction that occurs in the radiation therapy treatment energy range. Compton scattering is independent of the atomic number Z and depends upon the electron density. The probability of Compton scattering interaction decreases slowly with increasing photon energy. In Compton scattering, an incident x-ray photon interacts with an outer orbital electron, or “free” electron, transferring some, but not all, of its energy to the electron. A “free” electron means that the binding energy of the electron is much less than the incident x-ray photon energy (Khan 2003). The electron absorbs some of the energy from the incident x-ray photon and is ejected from the atom, and the incident photon scattered from its incident path with a new energy and wavelength (Washington 2010). The energy of the scattered x-ray photon can be determined from the following equation (Khan 2003):

Equation 1

$$hv' = hv_o * \frac{1}{1 + \varepsilon(1 - cos\varphi)}$$

$$where$$

Equation 2

$$\varepsilon = \frac{hv_o}{m_e c^2} \ and \ m_e c^2 = 0.511 \ MeV$$

The energy of the ejected electron, also known as the Compton electron, can be determined from the following equation (Khan 2003):

Equation 3

$$E = \frac{\varepsilon(1 - cos\varphi)}{1 + \varepsilon(1 - cos\varphi)}$$

Pair production occurs only when the energy of the incident x-ray photon is greater than 1.022 MeV, and this energy is known as the threshold energy (Washington 2010). Pair production is dependent upon Z^2 and E^2. In pair production, the incident x-ray photon interacts strongly with the electromagnetic field of the atomic nucleus. The photon gives up all of its incident energy resulting in the production of an electron-positron pair (Khan 2003). The total energy of the electron-positron pair is the excess energy remaining after the threshold energy:

Equation 4

$$E_{ep} = hv - 1.022$$

The positron created in the pair loses energy as it traverses matter through ionization, excitation, or bremsstrahlung. When the positron nears the end of its range, it combines with a free electron resulting in two annihilation photons each with energy of 0.511 MeV. The two annihilation photons are travel in opposite directions (180°) (Khan 2003).

Photoelectric effect interactions will occur with lower energy photons. As the photon energy increases, the probability of photoelectric effect interaction decreases with an increasing probability of Compton scatter interactions. As the energy continues to increases, the probability of Compton scatter interaction is slowly replaced by pair production interactions. In radiation therapy, the most common interaction type is typically Compton scatter which is largely responsible for dose deposition in tissue.

The types of interactions that occur in radiation therapy are not solely dependent upon the energy of the photon beam. They are also dependent upon the atomic number and electron density of material (tissue, bone, air, etc.) the radiation will pass through. The photoelectric effect dominates at lower energies in high atomic number materials. Compton scatter is independent of the atomic number of the material but is dependent upon the electrons per gram of the material (electron density). Pair production dominates for energies greater than 10 MeV in high atomic number materials (Washington 2010).

While Compton scattering is the dominant interaction in typical therapeutic radiation therapy, this can change when introducing high atomic number materials in the form of prostheses. In comparison with the incidence of these interactions without the high-Z prosthesis, the prosthesis increases the incidence of photoelectric effects and pair production. The photoelectric effect will increases at lower energies with the presence of the hip prosthesis and become a significant interaction type in the therapeutic range. Pair production interactions will increase with the higher energies of the therapeutic range with the presence of the hip prosthesis.

2.2.Pelvic Radiation Therapy

The most commonly performed definitive pelvic radiation therapy treats prostate cancer. Radiation therapy treatments for prostate cancer have developed and evolved with the ever-advancing technologies available in radiation therapy. This development and evolution has increased the normal tissue sparing while maintaining accurate and successful treatments to the tumor or target volume.

Different dose calculation algorithms exist in treatment planning systems. Three types of model-based dose calculation algorithms include pencil beam (convolution), convolution-superposition, and Monte Carlo. This study will only provide a brief description and the pros and cons of each algorithm.

Monte Carlo is the most advanced and accurate dose calculation algorithm associated with treatment planning in the radiotherapy setting. Monte Carlo applies known probabilities and probability distributions coupled with a random number generator to simulate the movement of quanta of radiation moving through a medium. Taking the sum total of many of these pseudo stochastically generated events and utilizing the Law of Large Numbers (LLN) and the Central Limit Theorem (CLT) a solution to radiative transport problem can be derived numerically (DesRosiers 2013). The LLN states the average of the results coming from many trials should be close to the expected value, and typically, the average will become closer with increasing number of trials performed (DesRosiers 2013). Monte Carlo uses interaction probabilities of electrons and photons, and the influence of density and atomic number of materials are taken into account (Laub and Nusslin 2003). The following figure depicts a Monte Carlo simulation of particle tracks:

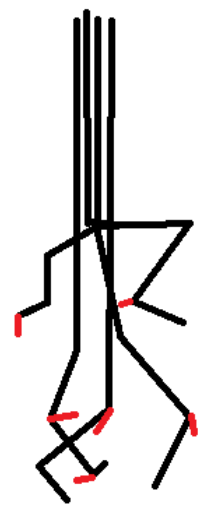

Figure 1: Monte Carlo

Monte Carlo calculations require an accurate modeling of an accelerator head model to give the parameters of the emitted photons. Monte Carlo is the most accurate method of dose calculation available today but requires a great deal of processing time to complete calculations making it impractical as a clinical treatment planning system (TPS). As cost for higher performance computing decreases and technology continues to evolve, it is hoped that Monte Carlo algorithms will be practical to implement as a clinical TPS in the future.

The pencil beam algorithm is one of the simpler dose calculation algorithms based on pre-calculated Monte Carlo pencil kernels. Pencil kernels are the “deposited energy in a semi-infinite medium from a point mono-directional beam” (Apipanyasopon 2012). In pencil beam, the treatment beam is assumed to be made up of many smaller, narrow “pencil beams” with the central axis of each pencil beam depositing some amount of dose which varies depending on the intensity and spectrum of the incident beam (Carolan 2010). Looking at a single pencil beam, the dose will spread out in a tear-shape when it hits the surface based on scattering and absorption processes the photon and secondary electrons undergo (Carolan 2010). This tear-shape distribution is known as the pencil dose kernel representing the dose at each point around the pencil beam. The following figure represents a pencil dose kernel (DesRosiers 2013):

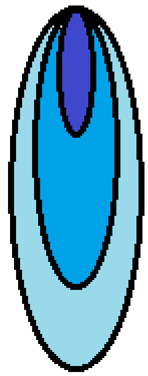

Figure 2: Pencil Dose Kernel

In order to determine the total dose distribution, the contribution for each point from each adjacent pencil beam making up the incident beam must be added together. This is done by superimposing the dose values for each pencil dose kernel on to each dose voxel and then summing the doses for the total dose at that point (Carolan 2010). The following figure depicts pencil beam superposition (Knoos 2013):

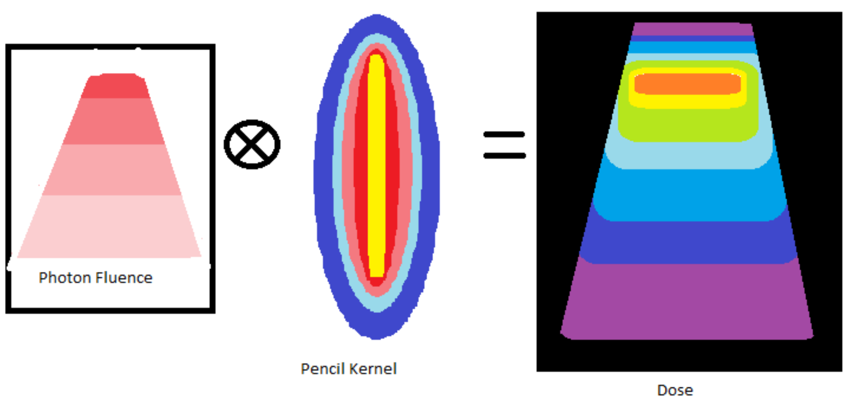

Figure 3: Pencil Beam

Heterogeneities are taken into account by applying a scaling factor to “stretch” or “squash” the shape of the dose kernel (Carolan 2010). The dose kernel is “stretched” when the density is reduced, such as in the lung, and the dose kernel is “squashed” when the density is increased, such as in bone. The following figure depicts the “stretching” and “squashing” of the pencil dose kernel (DesRosiers 2013):

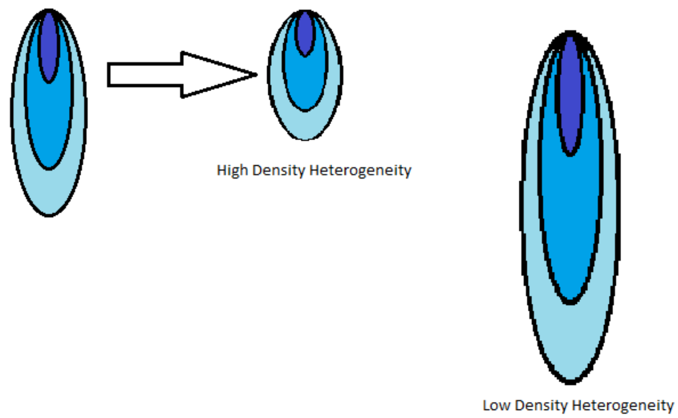

Figure 4: Heterogeneity Correction Method in Pencil Beam

The pencil beam algorithm has its drawbacks. Pencil beam calculates a 3D dose distribution from a 2D convolution. Scatter is not modeled well in pencil beam, and the lateral scatter is not even taken into account (DesRosiers 2013). The manner in which heterogeneities are handled is mostly an attenuation correction only. The dose kernels are spatially-invariant which is a source of some inaccuracy (DesRosiers 2013). Spatially-invariant means that the dose kernels are parallel to the surface and non-divergent (DesRosiers 2013). Further, the pencil beam algorithm does not accurately model material interfaces such as tissue to bone or bone to high atomic number prosthetic implant due to its inability to accurately account for the secondary electron production. *Laub and Nüsslin* showed that pencil beam modeling did not take into account the energy transport of secondary electrons leading to errors near surface and inhomogeneities, and pencil beam did not take into account atomic number variations of the different types of tissues (Laub and Nusslin 2003).

The most common and widely presently used dose calculation algorithm is convolution-superposition used in treatment planning systems. This method utilizes superposition in the same manner as pencil beam but also applies a 3D convolution instead of a 2D convolution. Convolution-superposition algorithms look at the primary photons separately from the scattered photons and secondary electrons, wherein it applies a modification for radiologic path length (Khan 2003). The radiologic path length is the distance corrected for electron density relative to water (Khan 2003). In convolution-superposition algorithms, range scaling by the electron density of the Monte Carlo-generated point kernels is used to modify dose point kernels initially based on water density medium (Khan 2003). The following figure depicts convolution-superposition (Knoos 2013):

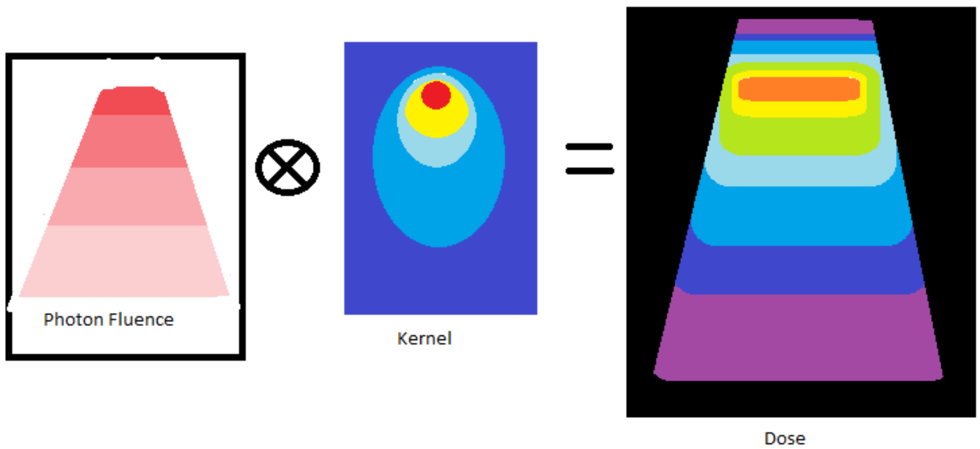

Figure 5: Convolution-superposition

Convolution-superposition algorithms have many advantages over pencil beam. Convolution-superposition algorithms utilize point kernels instead of pencil kernels resulting in a better modeling of scatter in 3D. A point kernel is the "deposited energy in an infinite medium around a primary interaction point" (Apipanyasopon 2012) depicted in the following figure:

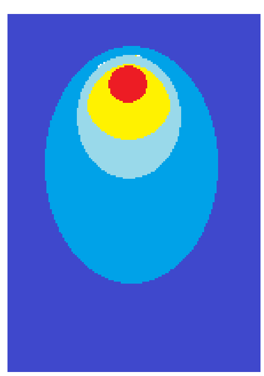

Figure 6: Point Kernel

Convolution-superposition methods calculate a 3D dose distribution from a 3D convolution. Divergence, lateral scatter, energy spectrum, and primary/secondary interactions with inhomogeneous media are all taken into account (DesRosiers 2013). Like pencil beam, convolution-superposition still encounters problems when attempting to accurately calculate the dose along material interfaces such as tissue to bone. This limitation is due to the inability to model the coupled photon-electron transport across the interface (Apipanyasopon 2012). Convolution-superposition calculates the dose distribution better than pencil beam but is not as accurate as Monte Carlo near high atomic number material interfaces. In part this is because of the type of interaction and, hence, scatter is assumed to be near tissue equivalent Z material.

2.3. Total Hip Arthroplasty and Hip Prostheses

The Center for Disease Control and Prevention (CDC) reported 332,000 total hip replacements procedures performed in the United States in 2010 ((CDC) 2010). Recent studies presented at the 2014 American Academy of Orthopaedic Surgeons (AAOS) estimated that in 2010, 4.5 million (1.5%) Americans were living with a prosthetic hip (Maradit-Kremers, Crowson et al. 2014). At this same meeting, it was presented that there is a growing incidence of adults younger than 65 undergoing total hip replacements (Lange, Briggs et al. 2014). In most industrialized countries, total hip replacement procedures have an incidence greater than 150 procedures per 100,000 habitants per year (Holzwarth and Cotogno 2012). This indicates that on the order of one million hip replacement procedures are performed worldwide every year (Holzwarth and Cotogno 2012). The rate of total hip replacements increased by approximately 25% between 2000 and 2009, and this trend is expected to continue in the coming years (Holzwarth and Cotogno 2012). One reason for the increased incidence of hip replacements is the large advancement in the longevity of the hip prosthesis implant.

Total hip replacements, or THA, are performed for patients experiencing chronic hip pain commonly caused by osteoarthritis, rheumatoid arthritis, post-traumatic arthritis, avascular necrosis, or childhood hip disease (AAOS 2014). When a THA is performed, the damaged bone and cartilage is removed first (AAOS 2014). After the damaged bone and cartilage is removed, it is replaced with prosthetic components (AAOS 2014).

A hip prosthesis used for THA includes a femoral stem, a femoral head, an acetabular cup liner, and an acetabular cup shell. The femoral stem is placed into the medullary cavity after the damaged femoral head is removed. It can either be cemented or "press fit" into the bone. The femoral stem is subjected to the highest mechanical stresses out of all of the hip prosthesis components (Holzwarth and Cotogno 2012). The femoral head is either a metal or ceramic ball that is placed on the upper part of the femoral stem replacing the damaged femoral head that was removed (AAOS 2014). The acetabular cup liner is also known as the insert and acts as the counterpart of the femoral head (Holzwarth and Cotogno 2012). The liner allows for a smooth gliding surface. The acetabular cup shell replaces the damaged cartilage surface of the acetabulum. It provides the outer face of the acetabular cup and must be fixed to the pelvis by bone cement or press-fitting (cementless) (Holzwarth and Cotogno 2012). Press-fitting is defined as "a match between the size and shape of two parts, such that force is required for assembly as one part is slightly larger than the other" (Holzwarth and Cotogno 2012). The following image illustrates the components of a hip prosthesis:

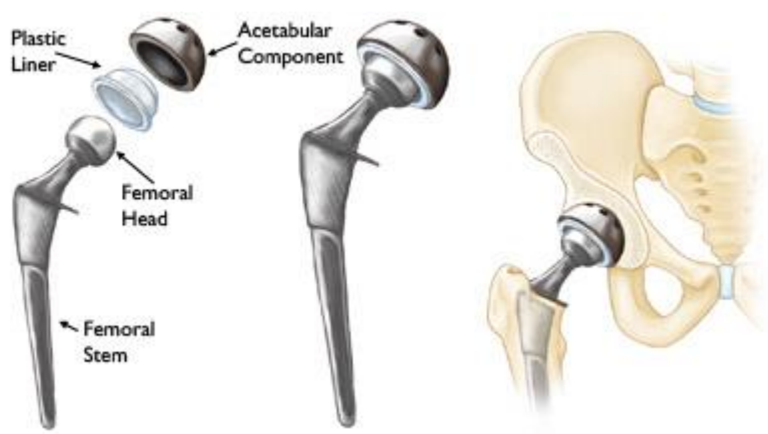

Figure 7: Hip Prosthesis Components (AAOS 2014)

Typical hip prosthesis are composed of a Titanium alloy, such as the Tri Lock® model manufactured by DePuy Synthes or a Co-Cr-Mo allow, such as the AML® model manufactured by DePuy Synthes (Orthopaedics 2002, Orthopaedics 2011). Stainless steel prostheses have also been employed in THA. Current hip prosthesis utilizing cementless technology employ fixation techniques using a porous coating such as Gription® (Warsaw, IN) fixation technology or Porocoat® (Warsaw, IN) coating (Orthopaedics 2002, Orthopaedics 2011). These porous coatings encourage new bone ingrowth into the artificial femoral stem instead of using cement. The following figures show the Gription® coating and interface of the Gription® coating to the hip prosthesis magnified:

Figure 8: Gription® Porous Coating on a Tri Lock® Hip Stem Magnified 10X

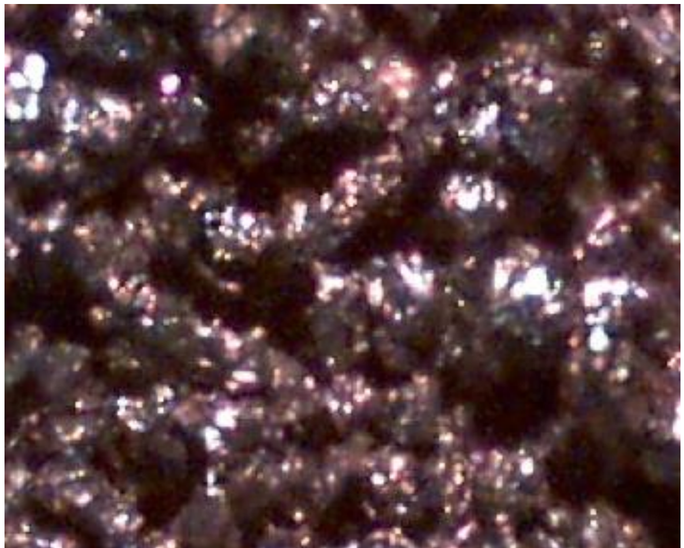

Figure 9: Gription® Porous Coating on a Tri Lock® Hip Stem Magnified 60X

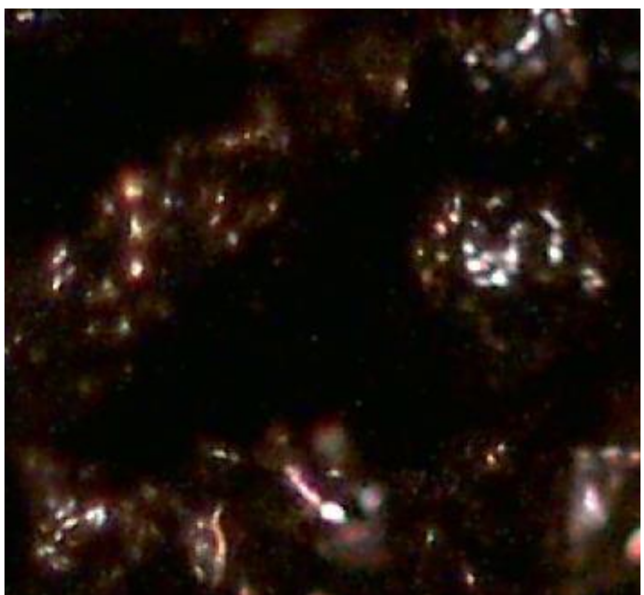

Figure 10: Gription® Porous Coating on a Tri Lock® Hip Stem Magnified 200X

Figure 11: Gription® Porous Coating interface on a Tri Lock® Hip Stem Magnified 10X

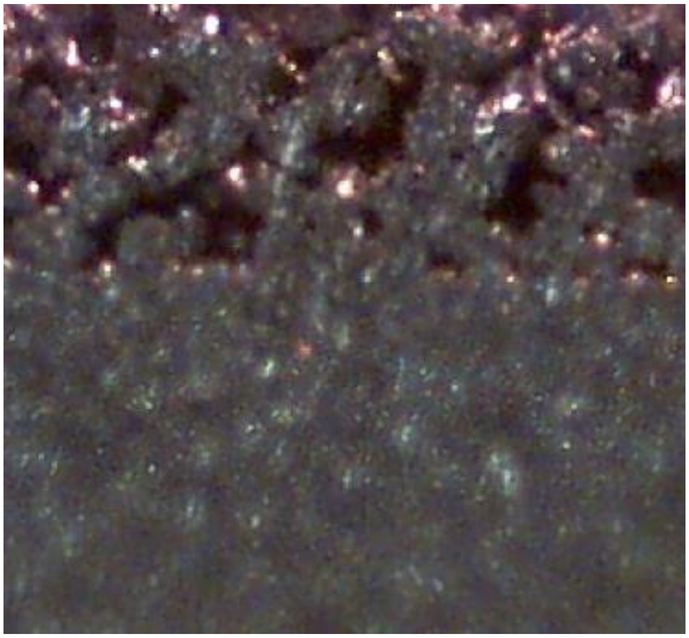

Figure 12: Gription® Porous Coating interface on a Tri Lock® Hip Stem Magnified 60X

The following figures show the Porocoat® coating and interface of the Porocoat® coating to the hip prosthesis magnified:

Figure 13: Porocoat® Porous Coating on an AML® Hip Stem Magnified 10X

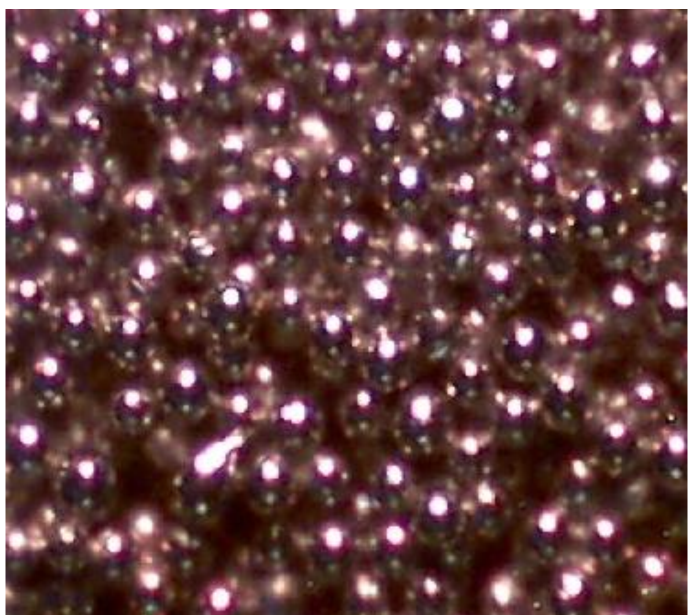

Figure 14: Porocoat® Porous Coating on an AML® Hip Stem Magnified 60X

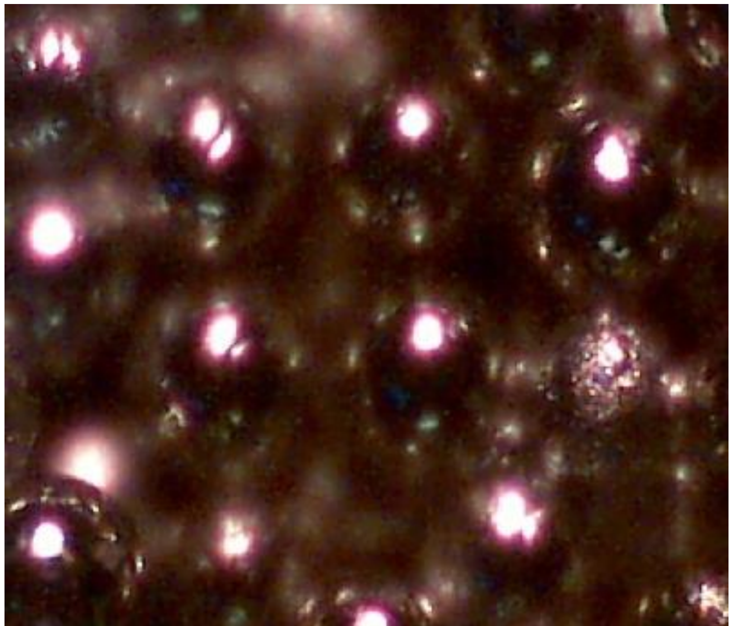

Figure 15: Porocoat® Porous Coating on an AML® Hip Stem Magnified 200X

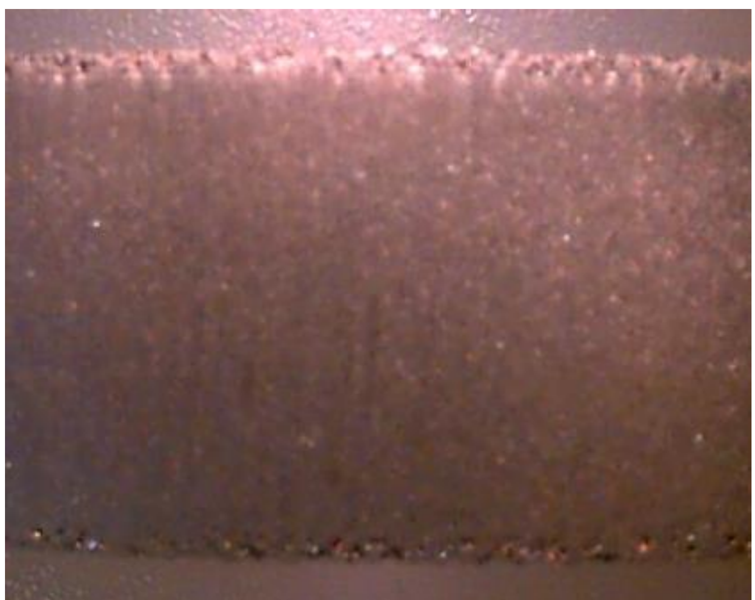

Figure 16: Porocoat® Porous Coating interface on an AML® Hip Stem Magnified 10X

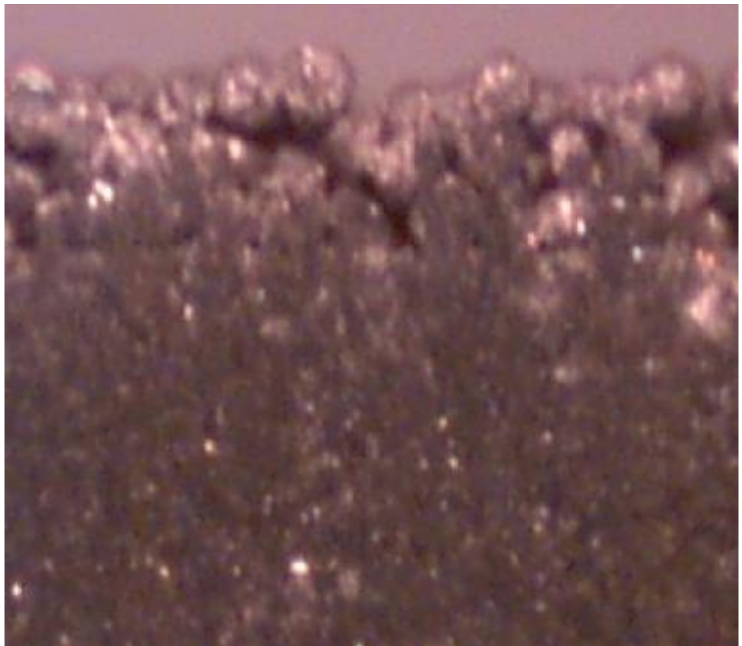

Figure 17: Porocoat® Porous Coating interface on an AML® Hip Stem Magnified 10X

2.4.Definitive Radiation Therapy with Hip Prosthesis

There are an increasing number of patients with prosthetic hips requiring definitive pelvic radiation therapy. As the number of total hip replacements continues to increase in the coming years so will the number of patients with hip prosthesis requiring definitive radiation therapy. Hip prostheses pose unique concerns and challenges in developing an accurate and deliverable treatment plan with confidence.

Interface effects are defined in AAPM's Task Group 63 as the local perturbations in the dose distribution. Interface effects occur in the body along any interfaces between tissue and materials of greater atomic number (Z) than tissue, including tissue to bone interfaces. Interface effects are typically of greater importance when involving high-Z materials. High-Z materials in the context of radiotherapy are defined as an atomic number greater than that of cortical bone (Reft, Alecu et al. 2003).

Dose perturbations along a prosthesis interface depend upon the incident photon energy, differences in the photon energy transfer coefficients, the atomic number, the mass density and thickness of the prosthesis, and the resulting differences in multiple scatter of the secondary electrons (Reft, Alecu et al. 2003). As the incident photon energy increases greater than 10 MV, there may be an increased dose distal to the prosthesis attributed to pair production interactions in the prosthesis (Reft, Alecu et al. 2003). The electron fluence increases laterally to the prosthesis since there is an increase in lateral scatter from the material resulting in an increased dose to the surrounding tissue (Reft, Alecu et al. 2003).

Hip prostheses also pose concerns in accurately simulating a patient in CT. The prosthesis itself will create streaking artifacts (beam hardening artifacts), and the scan must be post-processed in order to develop a treatment plan. These artifacts result in partial image loss, CT number error, and geometry error in the CT image.

Current treatment planning systems discussed earlier employ methods to account for beam attenuation as long as the composition of the prosthesis is known and the CT number to electron density conversion curve is suitable (Reft, Alecu et al. 2003). When treating patients with hip prosthesis, it is not always known the type or composition of prosthesis in place increasing the uncertainties involved in developing a successful treatment plan. Also, current treatment planning systems in their default setting may not be as accurate as needed in calculating the dose near the high-Z prosthesis. Treatment planning systems often have an upper limit for the electron density used for the heterogeneity correction algorithm. The only treatment planning system that will accurately calculate dose near high-Z material will utilize Monte Carlo methods which are not yet in widespread clinical use. While Monte Carlo is the most accurate method to date, it encounters challenges modeling the porous coating that most hip prostheses now utilize. The porous coating used on hip prosthesis is not uniform in shape and density as shown in the following figures:

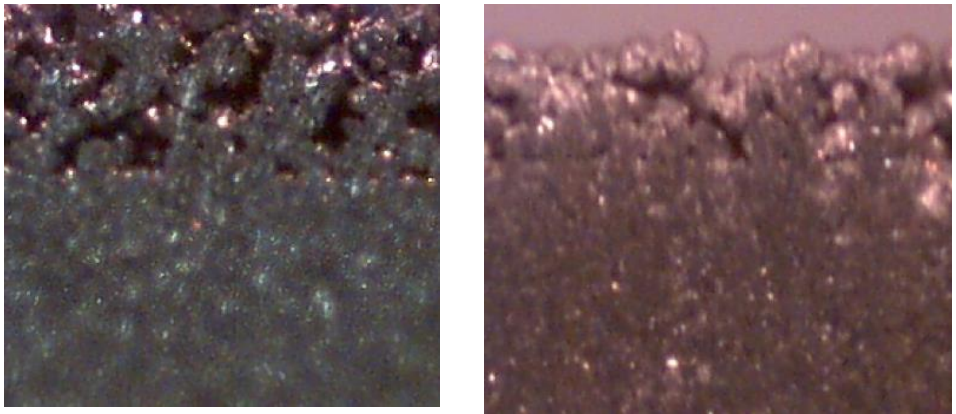

Figure 18: 60X Magnification of Hip Stem Interfaces with Gription® (left) and Porocoat® (right) Coating

The non-uniform shape and density can be challenging to model with Monte Carlo. With Monte Carlo, there is a limited mesh and voxel size based on the finite CT voxel size available. The voxels are typically not small enough to account for the very small differences in the shape and density of the porous coatings.

Several studies have been performed to quantify the dose perturbation along a hip prosthesis. These studies were performed by measuring the dose or by calculating the dose with a treatment planning system (Reft, Alecu et al. 2003). Measurements have been attempted either in phantoms containing prosthesis or in patients.

A study performed by *Ding and Yu* using parallel-opposed beams determined an approximate 15% increase in the dose to tissue within 2 mm of a stainless steel prosthesis interface facing the beam due to the scatter of electrons (Ding and Yu 2001). Also, *Ding and Yu* found the dose decreases by 5-45% in the shadow of the prosthesis depending on the material of the prosthesis in place (Ding and Yu 2001). The dose distributions in the presence of a metal hip prosthesis were performed using Monte Carlo modeling. These hot and cold spots must be accounted for properly and accurately in planning and delivery of pelvic radiation therapy. In this study, the prostheses materials were modeled as a metal bar. There is no mention of modeling the porous coating in this study.

Keall et al performed a study comparing the accuracy of dose calculations in the presence of hip prosthesis from Monte Carlo, superposition, and pencil beam algorithms. In the study, the hip prosthesis was assumed to be a solid prosthesis, and calculations were performed in phantom and patient geometries. Phantom calculations used solid blocks of iron or titanium. The iron block calculations represented Cobalt-Chrome prostheses (Keall, Siebers et al. 2003). This study did not mention representing or modeling the porous coating along the surfaces of the materials used. *Keall et al.* found Monte Carlo predicted the dose would increase while approaching the higher-Z materials with an immediate local decrease after crossing high-Z interface.

Keall et al. concluded that the "accuracy of the dose calculation algorithms in the vicinity of hip prosthesis materials is proportional to their complexity of physical process modeling" (Keall, Siebers et al. 2003). *Keall* found Monte Carlo to be the most accurate algorithm method in accounting for interface dose variations. Superposition was found to be limited at interfaces with different atomic numbers, but more than a few millimeters from the boundary, it did not significantly differ from Monte Carlo. Generally, superposition calculated a slightly higher dose than Monte Carlo. Pencil beam did not predict dose near the hip prosthesis interface well, but the difference between pencil beam and Monte Carlo decreased beyond the interface. Pencil beam calculated a higher dose than superposition (Keall, Siebers et al. 2003).

Laub and Nüsslin performed a study comparing Monte Carlo modeling to pencil beam with a hip prosthesis. Their study demonstrated that pencil beam overestimates the dose to the planning target volume up to 10% due to underestimating the absorption of photons through the hip prosthesis (Laub and Nusslin 2003). This study did not mention representing or modeling the porous coating along the surfaces of the materials used.

Eng performed a study to determine the dose attenuation through a solid titanium alloy hip prosthesis (Eng 2000). The study used a scanning film dosimeter to determine the transmission and the dose perturbation for both 6 and 15 MV photon beams (Eng 2000). *Eng* found a greater dose attenuation for the lower energy with the dose attenuation ranging from 32% to 60% for the 15 MV photon beam and 39% to 64% for the 6 MV photon beam (Eng 2000). The maximum dose attenuation occurred at the head and proximal shaft which is the thickest width of the prosthesis, and the minimum dose attenuation occurred at the tip which is the thinnest width of the prosthesis (Eng 2000). In *Eng's* study, the film dosimeter was scanned across a titanium alloy hip prosthesis at the widest (trans-axial) plane at various levels along the prosthesis (Eng 2000). The scanned film only measured transmission and does not supply dose physically close to the prosthesis.

The AAPM TG-63 recommends avoidance as the best option in treating patients with hip prosthesis, but this is not always a viable option. This task group also states that a heterogeneity correction may be employed when developing a treatment plan. When a heterogeneity correction is used, it is important to have an understanding of the limitations of the available treatment planning systems must always be taken into account.

2.5.Prophylactic Radiation Therapy

Outside of definitive pelvic radiation therapy for cancer therapy, prophylactic radiation therapy is typically utilized when a patient is undergoing a THA. Prophylactic radiation therapy is utilized for patients undergoing a THA to prevent heterotopic ossification. Heterotopic ossification is an adverse effect that may occur after a THA procedure.

Heterotopic ossification (HO) is defined as the "abnormal formation of mature, lamellar bone in soft tissues, often containing bone marrow" (Balboni, Gobezie et al. 2006). HO occurs in various locations of the body and is a major complication after THA, traumatic acetabular fracture, or central nervous injury (Seegenschmiedt, Keilholz et al. 1997). It is typically asymptomatic, detected only on a radiograph. If the HO is symptomatic, it commonly causes decreased range of motion of the hip and pain while in severe cases complete bony ankylosis[1] may occur (Balboni, Gobezie et al. 2006). Several studies have been performed to demonstrate radiation therapy as an effective tool for prevention of HO, to determine effective dose prescriptions, and to determine an effective treatment delivery time window.

Cooley and Goss demonstrated in 1958 that a single dose of 30 Gy to a fractured rat within the first week of healing would prevent bone repair. If the same dose was administered more than a week later, it would not prevent the bone repair (Cooley and Goss 1958). This study established the understanding that radiation therapy, if administered within an early window of bone healing, could prevent bone healing (Cooley and Goss 1958). *Craven and Urst* hypothesized in 1971 from their work with rats that osteoprogenitor cells present in the early phase of HO development are particularly radiosensitive (Craven and Urist 1971).

In 1981, *Coventry et al.* studied the effect of 20 Gy delivered in 10 fractions on patients considered to be high risk for HO (Coventry and Scanlon 1981). They concluded that radiation therapy may be an effective means to prevent HO (Coventry and Scanlon 1981). Work performed in the study by *Sylvester et al.* concluded that 10 Gy delivered in 5 fractions was comparable to 20 Gy in 10 fractions in prevention of HO (Sylvester, Greenberg et al. 1988). Their work also concluded that radiation therapy should be delivered post-operatively within 4 days of surgery (Sylvester, Greenberg et al. 1988).

From a retrospective study, *Lo et al.* concluded a single fraction of 7 Gy was effective in HO prevention (Lo, Healy et al. 1988). *Pellegrini et al.* concluded that a single fraction of 7-8 Gy was similar in efficacy to fractionated radiation therapy for HO prevention from a prospective study comparing single fraction therapy to fractionated therapy

---

[1] Bony ankylosis is defined as the union of the bones of a joint by proliferation of bone cells, resulting in complete immobility.

(Pellegrini, Konski et al. 1992). In a retrospective study comparing a single fraction of 7 Gy to a single fraction of 5.5 Gy performed by *Healy et al.* it was found that a single fraction of 5.5 Gy was insufficient in prevention of HO (Healy, Lo et al. 1995).

Kantorowitz et al. found from their work with rats that radiation therapy may be delivered pre-operatively to effectively prevent HO (Kantorowitz, Miller et al. 1990). *Gregoritch et al.* reported no significant difference between prophylactic RT delivered pre-operatively within 4 hours of surgery and post-operatively delivered within 72 of surgery in their randomized, controlled trial (Gregoritch, Chadha et al. 1994). The two randomized trials performed by *Seegenschmiedt et al.* in 1997 presented data supporting both pre-operative and post-operative radiation therapy as an effective means of HO prevention (Seegenschmiedt, Keilholz et al. 1997). *Seegenschmiedt et al.* performed a multicenter study in 2001 that concluded that both prophylactic radiation therapy delivered pre-operatively within 4 hours of surgery or post-operatively within 72 hours of surgery are effective methods of preventing HO (Seegenschmiedt, Makoski et al. 2001).

The randomized trial completed by *Kölbl et al.* showed that a single fraction of 7 Gy delivered post-operatively is more effective at HO prevention than a single fraction of 5.5 Gy or use of indomethacin (Kolbl, Knelles et al. 1997). Work completed by *Balboni et al.* discussed radiation therapy as an alternative to indomethacin for HO prevention (Balboni, Gobezie et al. 2006). The available data supported the standard of a single fraction of 7-8 Gy radiation therapy delivered either less than 4 hours pre-operatively or less than 72 hours post-operatively (Balboni, Gobezie et al. 2006).

Balboni et al. performed a retrospective study to determine whether there is an increased risk of HO when prophylactic radiation therapy is performed with shielding of the prosthesis components (Balboni, Gaccione et al. 2007). They found that shielding was associated with an increased risk of HO development even with adjusting for other predictors of HO development, and shielding was not associated with a reduced risk of prosthesis failure (Balboni, Gaccione et al. 2007). *Balboni et al.* concluded that prophylactic radiation therapy should be performed without shielding of the prosthesis components.

Recently, a retrospective study comparing patients receiving prophylactic radiation therapy to patients who did not performed by *Childs et al.* enforced the effectiveness of radiation therapy in preventing HO (Childs, Cole et al. 2000). *Chao et al.* demonstrated that prophylactic radiation therapy is capable of preventing HO in patients with a high-risk of HO development (Chao, Lee et al. 2006).

2.6.Radiochromic Film

Radiochromic film is film that changes color when exposed to ionizing radiation without any chemical or physical processing required (Lewis, Micke et al. 2012). Radiochromic film utilizes the optical density to determine the dose to the film. Optical density is the measure of the amount of light passing through the film. The relationship between optical density and dose can be expressed as:

Equation 5

$$optical\ density\ (OD) = log_{10}\left(\frac{I_o}{I}\right)$$

where I_o is the light intensity with no film present and I is the light intensity after passing through the film. Optical density has a limited linear range to dose since I_o/I has an exponential relationship to dose (Butson, Yu et al. 2003).

Radiochromic film is advantageous to use in radiation therapy applications due to its weak energy dependence, near tissue equivalence, high spatial resolution, small thickness, and wide dynamic range. It also can be exposed from any angle, handled in light, cut to size, bent to shape, and immersed in water (Lewis 2012). Radiochromic films were pioneered by William McLaughlin and David Lewis (Soares). Radiochromic film consists of a single or double self-developing active layer and several protection layers (Soares). When the radiochromic film is exposed to radiation, the film will darken in a shade of blue proportional to the absorbed dose (Soares). The color change occurs from chemical changes due to the polymerization process. A polymerization process occurs when the energy is transferred from an energetic photon or particle to the receptive part of the colorless photomonomer molecule (Niroomand-Rad, Blackwell et al. 1998). Twenty-four hours after exposure, there is relatively little change in color density (Niroomand-Rad, Blackwell et al. 1998).

Gafchromic™ EBT (External Beam Therapy) film was developed to replace silver halide radiographic film for IMRT QA. EBT film utilizes the red color channel in determining dose measurements extracted from a RGB (red-green-blue) flatbed scanner (Devic 2011). The red color channel has been shown to be the most sensitive color channel to lower doses (<10 Gy) (Borca, Pasquino et al. 2013). The EBT sensitive layer was modified to increase the sensitivity tenfold. Only using the red color channel, the dose range of EBT film is up to 8 Gy, while utilizing all three color channels (RGB) it has been shown that the dose range can be extended above 100 Gy (Devic 2011). The defined range for EBT film was defined as 0.2 Gy to 100 Gy with an uncertainty of about 2% attributed to the sensitive layer non-uniformities. The 2% uncertainty was a great improvement over the 10-15% and 6-8% uncertainty of predecessors (Devic 2011). EBT film consists of a clear polyester (97 µm), active layer (17 µm), surface layer (6 µm), active layer (17 µm), and clear polyester (97 µm) as shown in the following figure (Devic 2011):

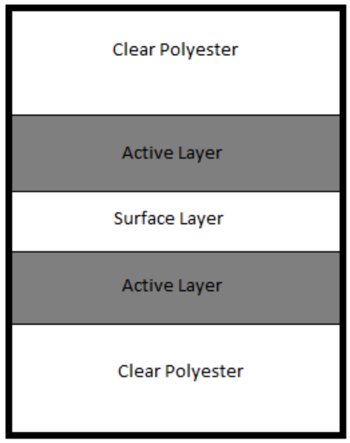

Figure 19: EBT Film Dimensions

The next generation of Gafchromic™ Film, EBT2, improved upon the film response uniformity by adding a yellow dye, known as the marker dye, to the sensitive layer to allow for corrections to be made in the thickness of the active layer (Devic 2011). A sensitive layer thickness correction matrix can be constructed from mapping the absorption of the blue channel in two dimensions since the marker dye has the strongest absorption in the blue channel (Devic 2011). EBT2 consists of a polyester overlaminate (50 µm), adhesive layer (25 µm), top coat (6 µm), active layer (30 µm), and polyester substrate (175 µm) as shown in the following figure (Devic 2011):

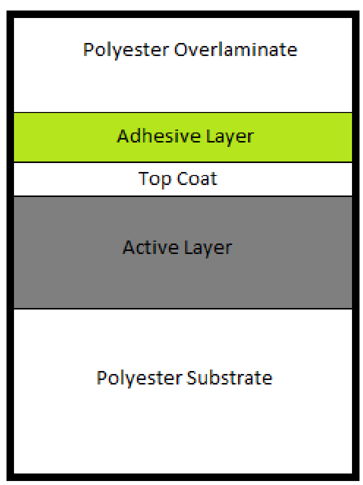

Figure 20: EBT2 Film Dimensions

EBT2 film is not symmetric, so care must be taken to ensure that the correct orientation of the film is used for exposure and scanning analysis (Devic 2011).

Gafchromic™ EBT3 film was the next generation of Gafchromic™ film with improved characteristics. EBT3 is symmetric in composition so the issue of face-up or face-down orientation is no longer of concern as it was with EBT2. EBT3 film consists of two transparent, polyester substrates (120 μm) sandwiching the active layer (27 μm) as shown in the following figure (Borca, Pasquino et al. 2013):

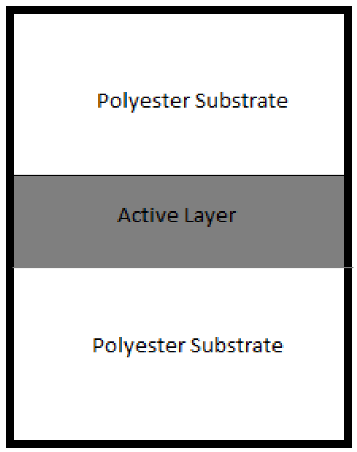

Figure 21: EBT3 Film Dimensions

The yellow marker dye added in EBT2 is also added in EBT3. Each polyester substrate receives a special surface treatment containing microscopic silica particles. These silica particles maintain a gap between the film surface and the glass window of the scanner, eliminating the formation of Newton's Rings (Borca, Pasquino et al. 2013).

Using multi-channel methods, the red color channel is the most sensitive at lower doses up to 10 Gy. The green color channel is most sensitive for doses greater than 10 Gy. The blue channel is useful in determining the active layer thickness non-uniformities and developing a correction matrix since the yellow marker dye is absorbed the most in the blue channel.

A description of the handling protocols for Gafchromic™ film can be found in AAPM's Task Group 55 (Niroomand-Rad, Blackwell et al. 1998). Inspection of film should be performed upon receipt of film. Any damage will appear as a milky white color at the damaged site instead of clear. Since the films can attract and gather dust due to the static charges on the outer layers, the films should be carefully wiped clean with a lintless paper prior to use. If the film is cut, the edges near the cuts may be stressed and should be avoided for dosimetric analysis. The recommendation is to keep the light analyzing beam about 1.5 mm away from the cut edges (Niroomand-Rad, Blackwell et al. 1998).

It has been shown that radiochromic films can be used for interface dosimetry such as tissue-metal dental interfaces (Reft, Alecu et al. 2003). Following this example, it could be assumed that radiochromic film can be placed to measure the entire dose distribution through a high-Z material prosthesis.

3. Materials and Methods

This study required completion of different procedures to ensure the validity of the data collected. The following sections are broken down into each procedure performed. In order to validate the calibration of the Gafchromic™ EBT3 film, ion chamber point measurements were taken at eight points on a treatment plan developed for measurement evaluation. Pinnacle^3 (Andover, MA) also calculated the same eight point dose values to act as a second check.

In order to compare the EBT3 film measurements gathered from the delivery of the same eight point treatment plan, a film calibration needed to be performed. After the film calibration, the eight points gathered from the EBT3 film were compared to the dose values from the ion chamber and Pinnacle^3. This comparison was performed to validate the calibration and evaluate the confidence of the film measurements.

The next procedures developed and used for this study were related to the stainless steel and titanium rods. Following a defined procedure developed from guidelines the film dosimetry supplier (Ashland) for film measurements with the rods, film sets were taken and analyzed. Ion chamber measurements were taken for a comparison to the film findings to determine the validity and confidence in the film measurements. To evaluate the ability of the Pinnacle[3] dose calculation algorithm, point dose measurements were calculated in Pinnacle[3] at the interfaces of stainless steel and titanium density volumes. These values were compared to the film interface values.

Similar film processing procedures were utilized for the hip stem film measurements. Ion chamber measurements were also taken for a comparison to the film findings to determine the validity and confidence in the film measurements. The titanium rod film findings were then compared to the Tri Lock® hip stem findings since the densities of the two materials vary only slightly. Finally, an evaluation of the perturbation of dose within a specified distance of the interfaces was performed.

3.1.Materials

The following resources and tools were used to complete this study:

- Elekta Infinity™[2] (Atlanta, GA) linear accelerator with 6 and 18 MV
- A12 Ion Chamber
- A14 Ion Chamber
- Crank operated probe positioning water tank

[2] Infinity™ Linear Accelerator located at Tuality/OHSU Cancer Center in Hillsboro

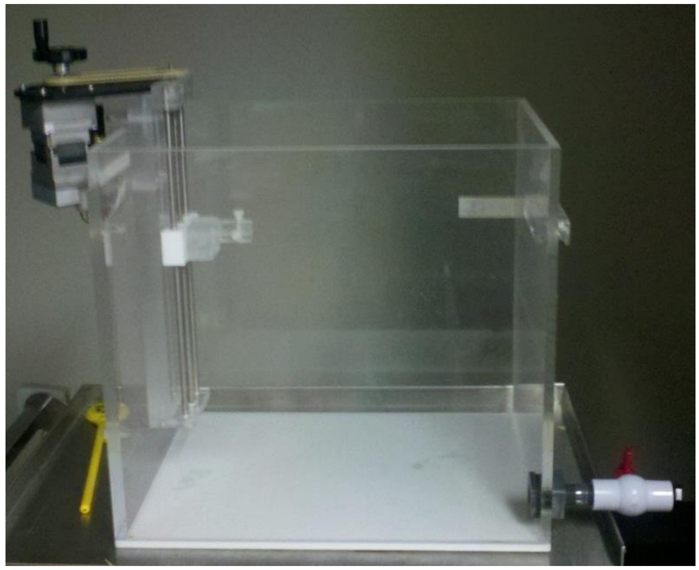

Figure 22: Crank Water Tank

- Pinnacle[3] Radiotherapy Planning System
- Thermometer and Pressure gauge
- Electrometer (PTW Unidos® E (Brooklyn, NY))
- 48-bit RGB Epson Expression 10000XL flatbed scanner
- Epson Scan software and Twain driver
- Laptop (specific laptop used for FilmQA™ Pro (Covington, KY) film analysis and evaluation)
- FilmQA™ Pro software application (Ashland)
- Solid water blocks (standard)
- Solid Water block (special/modified for rod measurements)
- Gafchromic™ EBT3 film (include manufacturer info and batch number)
- Solid Stainless Steel rods (1" and ½")
- Solid Titanium rods (1" and ½")
- Tape
- Philips Big Bore CT scanner[3]
- Ruler
- Tri Lock® model sample hip stem from DePuy Synthes
- AML® model sample hip stem from DePuy Synthes

[3] Philips Big Bore CT located at Tuality/OHSU Cancer Center in Hillsboro

3.2.Film Analysis

In order to evaluate the films, each film needed to be scanned by a flatbed scanner. The Epson 10000XL RGB flatbed scanner was used to scan all of the films for this study. The scanner was set to transparency mode with positive film using 48 bit color, 75 dpi, and no color correction in the landscape mode/orientation.

After scanning the film, film analysis was performed using FilmQA™ Pro software as suggested by the film manufacturer (Ashland) following the User's Manual (Ashland 2014). FilmQA™ Pro provides a variety of methods for evaluation. The two evaluation tools utilized the most in this study were the dose square statistics tool and the dose profile tool.

With the dose square statistics tool, a dose region square can be created using the frame tool. The statistics tab provides information for each color channel within the dose region frame including average value, standard deviation, maximum value, and minimum value. An example of a dose region square is shown in the following figure:

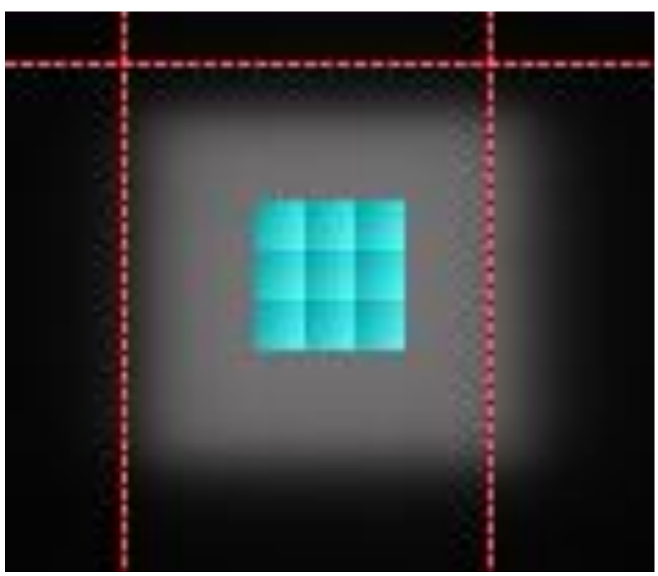

Figure 23: Example Dose Square Screen Shot

With the profile tool, a profile can be drawn over the region of interest. Selecting to see all the statistics and selecting the red color channel provides the average value, standard deviation, maximum value, and minimum values. An example of a dose profile is shown in the following figure:

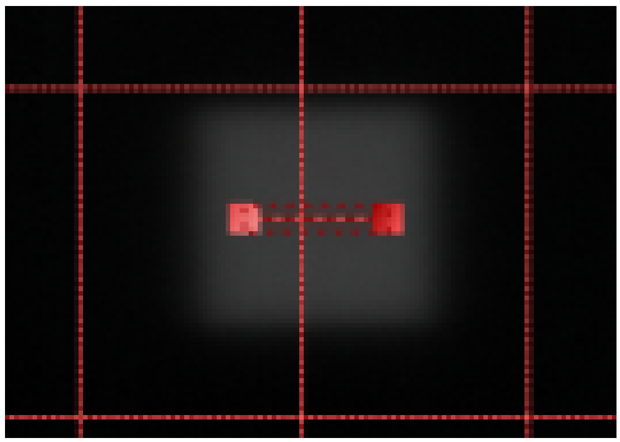

Figure 24: Example Dose Profile Screen Shot

When analyzing the EBT3 film, only the red was considered because the blue channel is only helpful for film thickness/uniformity. The green channel was not used because it is more helpful for doses greater than 10 Gy. The red channel was the most sensitive color channel for the dose range used in this study.

The standard deviations for each pixel point are determined from the pixel path range (the red dotted line in Figure 29). As per the recommendations of Ashland, the default pixel range width of 10 pixels was used for this study. To check the 10 pixel range width selection, profiles were taken for comparison with 70 pixel range width. This check was to evaluate whether the amount of noise in the profiles decreased with an increased pixel range width.

The standard error shown in the raw profiles was determined by the following equation:

Equation 6

$$standard\ error = \frac{standard\ deviation}{\sqrt{pixel\ range\ width}}$$

The 95% confidence was determined based on Gaussian statistics using the standard error.

Equation 7

$$95\%\ Confidence = 2 * standard\ error$$

Each set of film measurements were compared to evaluate the level of confidence in reproducibility and in the film measurements.

3.3.Pinnacle^3 Calculated Dose for Film Calibration Verification

In order to ensure that calibration of the Gafchromic™ EBT3 film was performed correctly, an 8 square plan was developed in the Pinnacle^3 planning system. The 8 square plan was delivered to a sheet of EBT3 film for analysis. The film analysis included both dose region squares and dose profiles for comparison to ion chamber measurements. The plan created in Pinnacle^3 consists of 8 squares of 2.9 x 2.9 cm^2 as shown in the following figure:

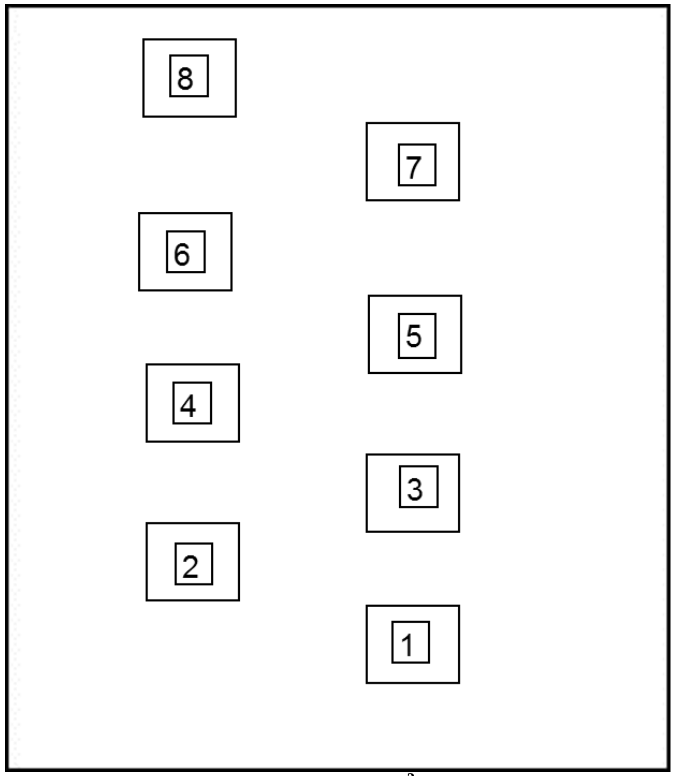

Figure 25: Pinnacle[3] Plan

A step-by-step procedure for delivery and analysis of the Pinnacle[3] plan to EBT3 film can be found in the Appendix.

3.4. Ion Chamber Water Tank Measurements for Film Calibration Verification

Using the same Pinnacle[3] 8 square plan, ion chamber water tank measurements were taken for the primary comparison to the delivered plan to a sheet of EBT3 film. Measurements were taken with an A14 ion chamber and then cross calibrated with an A12 ion chamber to find the dose per MU and the dose to each of the 8 squares depending on the MU used in delivering the plan. Two measurements were taken with the A14 chamber at the center of each of the 8 squares. Two measurements were taken to obtain an average response at the center of each square. The average measurement for each square was then cross calibrated with the A12 to determine the response of the linear accelerator (MU/cGy).

The following tables provide calibration data for the A12 and A14 ion chambers:

Table 1: A12 Ion Chamber Cross Calibration Data

A12 Chamber	
Reading 1 (nC)	28.22
Reading 2 (nC)	28.22
Reading 3 (nC)	28.23
Average Reading (nC)	28.22
Dose (cGy)	133.15
nC/MU	0.1411
cGy/MU	0.6658

Table 2: A14 Ion Chamber Cross Calibration Data

A14 Chamber	
Reading 1 (pC)	506
Reading 2 (pC)	505
Reading 3 (pC)	506
Average Reading (pC)	505.67
Dose (pGy)	2385.61
pC/MU	2.5283
nC/MU	0.00253
cGy/pC	0.26332
cGy/nC	263.317

The following table presents the dose per MU found from the ion chamber calibration and cross calibration.

Table 3: Dose per MU for each Square Position

Position	cGy/MU
Square 1	0.1016
Square 2	0.1999
Square 3	0.2947
Square 4	0.3905
Square 5	0.4877
Square 6	0.5846
Square 7	0.6862
Square 8	0.7942

A step-by-step procedure for gathering ion chamber water tank cross calibration and dose measurements can be found in the Appendix.

3.5. Gafchromic™ EBT3 Film Calibration

Calibration of the Gafchromic™ EBT3 film was performed as per the recommendations from the manufacturer's (Ashland) user guide and the one scan protocol (Lewis 2012). Calibration of Gafchromic™ EBT3 film determines the average response of the system consisting of the radiation source, the Gafchromic™ film, the RGB scanner, and the mode of operation. The radiation source may include non-homogeneities in the flat field. The Gafchromic™ film may have non-uniformities. The RGB scanner may add lateral effect and noise. Lateral effect, also known as the parabola effect, is defined as “the non-uniform response of the scanner in the direction at right angles to the movement direction of the light source” (Poppinga, Doerner, et al., 2014). The mode of operation encompasses film orientation and ambient conditions.

For this study, the maximum dose used for calibration was 305.2 cGy. Any EBT3 films based on this calibration must fall within the calibrated dose range (0 – 305.2 cGy).

The calibration film strip exposures used can be found in the following table:

Table 4: EBT3 Calibration Film Strip Exposures

Strip #	MU	Dose (cGy)	Percent of Max. Dose in Pinnacle[3] Patient Plan
1	0	0	0.0%
2	23	20.056	6.4%
3	56	48.832	16.0%
4	140	122.08	40.0%
5	350	305.2	100.0%

A step-by-step procedure to perform a calibration of Gafchromic™ EBT3 can be found in the Appendix.

3.6. Verification of Gafchromic™ EBT3 Film Calibration

The ion chamber water tank dose measurements for each square were compared to the EBT3 film dose values found for each square. The ion chamber measurements were compared to both the dose region squares and the dose profiles for each square. This comparison was also performed to evaluate the level of confidence in the EBT3 film measurements.

3.7. Stainless Steel and Titanium Rod Measurements with Gafchromic™ EBT3 Film

Half inch and one inch diameter medical grade stainless steel and titanium rods were used to take measurements with EBT3 film. Each rod was machined in half lengthwise to allow the best film placement. The machined rods are shown in the following figure:

Figure 26: Stainless Steel and Titanium Rods

The following table presents the mass density of the stainless steel and titanium rods used in this study (Fort Wayne Metals, 2011):

Table 5: Stainless Steel and Titanium Rod Alloy Data

Rod Type	Rod Material	Mass Density (lbs/on3)	Mass Density (g/cm3)
Stainless Steel	SS 316 LVM	0.287	7.944
Titanium	Unalloyed Commercially Pure Titanium	0.163	4.512

A modified solid water block was used to position the rods without movement. It also allowed the film to remain as flat across the top of the solid water as possible. The modified solid water block is shown in the following figures:

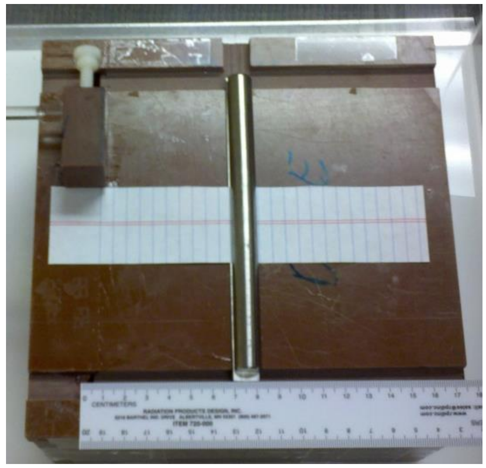

Figure 27: Top Down View of Solid Water Block

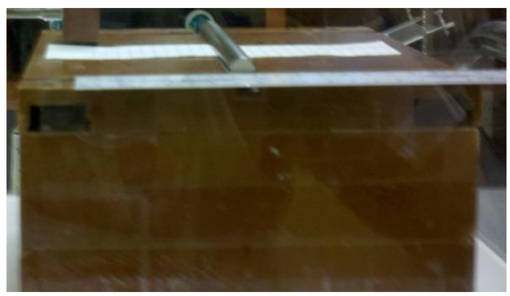

Figure 28: Side View of Solid Water Block

When analyzing the film, a dose profile was taken for each film. An example of a dose profile is shown in the following figure:

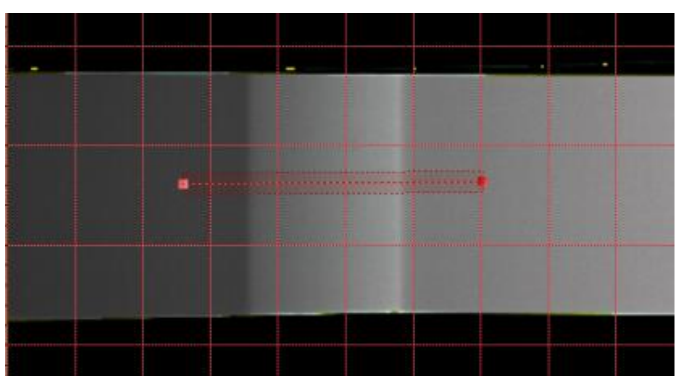

Figure 29: Example of a Dose Profile

The raw profile data and standard deviations were extracted for analysis of the each film measurement. For each set of film measurements, the normalized dose profiles were compared to evaluate the reproducibility of the film measurements. The interface dose was determined by evaluating the profiles. An example of a profile across one of the rods is shown in the following figure:

Figure 30: Example Profile Across a Rod

The interface location was determined to be the peak of the buildup of dose approaching the high-Z material immediately before the dip in dose on both sides. In the example profile, the peak points are located at positions 9 mm and 36 mm (as shown by the arrows). The peak points just before the local decrease are the points right at the surface interface.

The standard error and the 95% confidence intervals were previously discussed and calculated by Equations 6 and 7. The error bars were only included with the raw profile data. A step-by-step procedure to perform rod measurements can be found in the Appendix.

3.8. CT scan and Pinnacle^3 Calculated Dose of Stainless Steel and Titanium Rods

A CT scan of each rod was performed and sent to the Pinnacle^3 planning system to develop a treatment plan representative of the rod measurement beam delivery setup (with gantry at 0º only). The calculated doses from the Pinnacle^3 plans were then compared to the film measurements with the rods. Comparisons were made further away from the rod interface using the distant ambient field profiles from the film. Further away for the rod interface, the film measurements and the Pinnacle^3 calculated values are assumed be very similar with negligible perturbation of the dose due to the high-Z rods. The following image is a screen shot of an example of a profile from the distant ambient field of the films taken with rods in place (to the side of the rod):

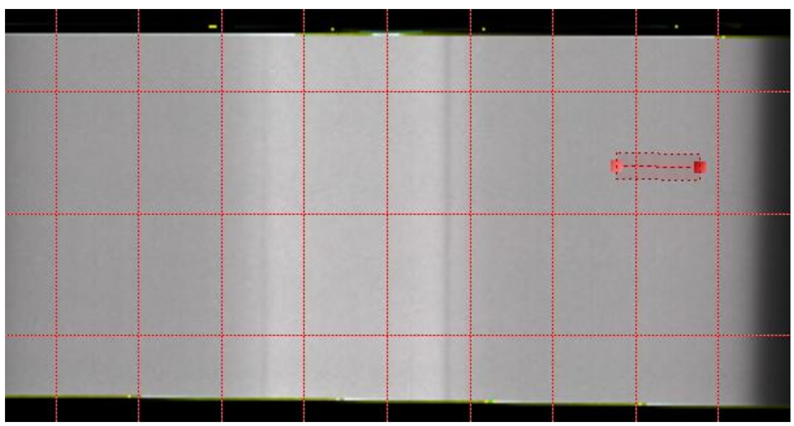

Figure 31: Example of a Distant Ambient Field Profile on Film for Rods

Comparisons of dose were also made close to the rod interface. These comparisons were made to evaluate the discrepancies between the film measurements and the Pinnacle^3 calculated values close to the rod interface. A step-by-step procedure for the CT scans and Pinnacle^3 plan development can be found in the appendix.

3.9. Hip Stem Measurements

Two hip stems were provided by DePuy Synthes for this study. One hip stem was the Tri Lock® model, the other was the AML® model. The Tri Lock® model featured a cementless Titanium alloy stem with Gription® porous coating. The AML® model featured a Co-Cr-Mo alloy stem with Porocoat® porous coating. The following figure shows the sample hip stems before any preparation for film measurements:

Figure 32: Tri Lock® and AML® Hip Stems from DePuy Synthes

The following table presents the mass density of the hip stems used in this study:

Table 6: Hip Stem Data

Hip Stem	Hip Stem Material	Mass Density (lbs/on3)	Mass Density (g/cm3)
Tri Lock®	Ti 6Al-4V ELI	0.160	4.429
AML®	Co-Cr-Mo	0.285	7.900

In order to create the best film placement for interface measurements, the two sample hip stems were cut with a precision water jet cutter[4] as shown in the following figures:

Figure 33: Cut Tri Lock® Hip Stem with Gription® Coating

[4] Precision water jet cutting performed by Rickard Engineering and Design

Figure 34: Cut AML® Hip Stem with Porocoat® Coating

Film measurements were performed at both 6 MV and 18 MV with the gantry at 0° only. The modified solid water block was not applicable in the hip stem setup; therefore, new stands were needed for each hip stem. PVC piping was used to position the stems properly as shown in the following figures:

Figure 35: Tri Lock® Hip Stem PVC Stand

Figure 36: AML® Hip Stem PVC Stand

The film was cut 5 cm wide and 10 cm long. The length was shortened compared to the stainless steel and titanium rod measurements to ensure the film remain flat instead of bowing up while remaining long enough for quality measurements. The film remains flat with the shorter length as shown in the following figure:

Figure 37: Film Placement reducing bowing for level and flat films

The bowing was not a concern with the stainless steel and titanium rods because the solid water block allowed the film to lay flat. With the unique geometry of the hip stems, it was not feasible to build a comparable water block cutouts to position the hip stems.

Each film was labeled with the type of stem (Tri Lock® or AML®), orientation, SSD, field size (10 x 10 cm^2), MU, energy (6X or 18X), and date. The normalized dose profiles for each set were compared to ensure reproducibility and determine the relative dose. The interface dose was determined by evaluating the profiles. An example of a profile across one of the hip stems is shown in the following figure:

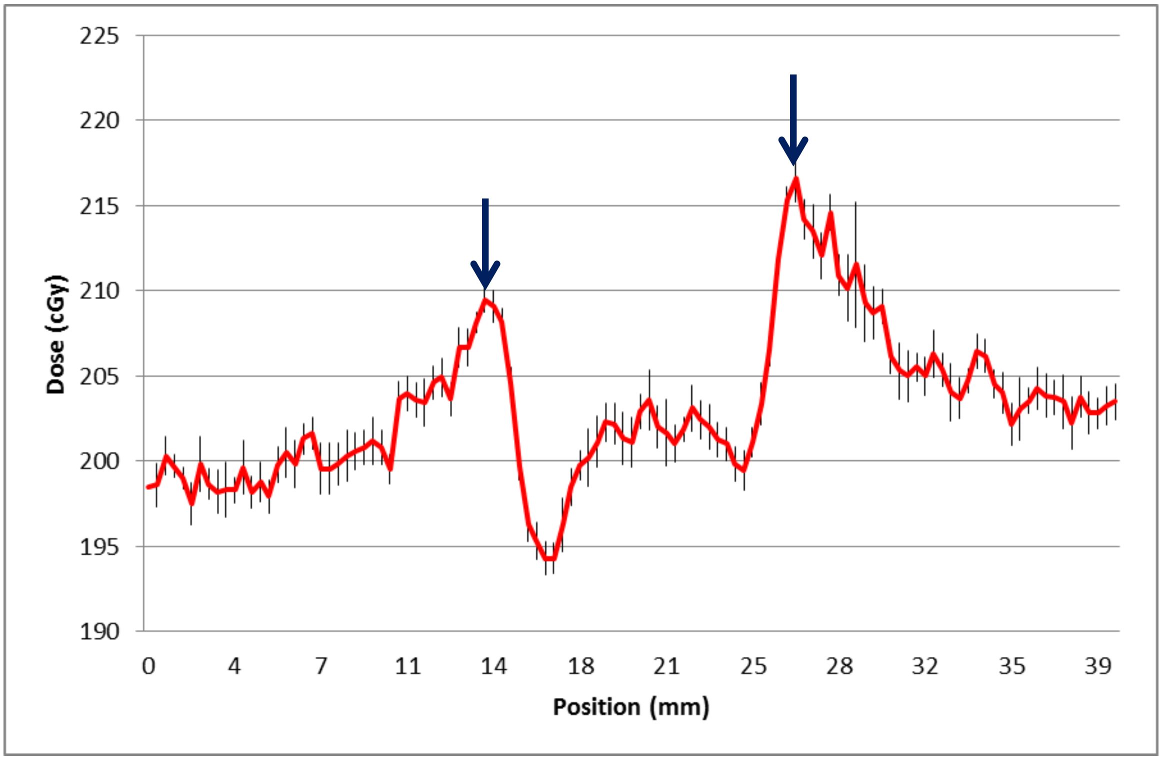

Figure 38: Example Profile across a Hip Stem

The interface location was determined to be the peak of the buildup of dose approaching the high-Z material immediately before the dip in dose on both sides. In the example profile, the peak points are located at pixel positions 14mm and 26 mm (as shown by the arrows). The peak points just before the local decrease are the points right at the surface interface.

The standard error and the 95% confidence intervals were previously discussed and calculated by Equations 6 and 7. The error bars were only included with the raw profiles. A step-by-step procedure for the sample hip stem film measurements can be found in the appendix.

3.10. Comparison of Titanium Rods to Tri Lock® Hip Stem

The titanium profiles were compared to the profiles gathered from the Tri Lock® hip stem. These profiles were compared because they are of comparable material. The density of the solid titanium rods is 4.512 g/cm^3. The Tri Lock® hip stem is composed of a titanium alloy (Ti 6Al-4V ELI) with a density of 4.429 g/cm^3. The densities differ by less than 2% thus justifying a comparison of dose perturbation profiles.

In order to compare the rod normalized profiles to the Tri Lock® normalized profiles, the average of the three sets of film were found for the 1" and ½" titanium rod and the Tri Lock® hip stem. The average normalized profiles were found for both 6 MV and 18 MV, and only the 0° gantry position was used for the titanium rods. Since the size of the rods and hip stem varied, only the left interface of the profile was evaluated. The profiles are aligned at the surface interface for comparison. While the shape of the solid titanium rods and the Tri Lock® hip stem are different, the magnitude and shape of the interface doses were compared to determine the effect of the porous coating on interface dose.

3.11. Decrease in Dose 2 mm from the Interface

The greatest increase in dose laterally occurs near the surface interface within millimeters, and therefore, it is most important to evaluate the dose perturbation close to the surfaces of the high-Z materials. In order to do this, the dose decrease within 2 mm of the surface interfaces was calculated. The relative decrease in dose 2 mm from the interface surface was calculated by comparing the average relative interface dose to the relative dose 2 mm from the interface. These values were found by evaluating the normalized profiles.

4. Results and Discussion

4.1. Verification of EBT3 Film Calibration

4.1.1. Ion Chamber vs. Gafchromic™ EBT3 Film

When analyzing the EBT3 film exposed to the 8 square plan, the film was scanned twice. The first time the film was scanned with squares 1, 3, 5, and 7 aligned to the center of the scanner. Squares 2, 4, 6, and 8 were aligned at the center of the scanner for the second scan. Dose region squares and dose profiles were taken for squares 1, 3, 5, and 7 from the first scan and for squares 2, 4, 6, and 8 from the second scan. The following tables present the difference for each square between the ion chamber measurements and the profiles and dose region squares. The plots present the dose values found from each method and how they align with each other.

Table 7: Tabular comparison of the ion chamber point measurements taken in a water tank and the EBT3 film measurements found using dose profiles.

Square #	Percent Difference (%) Red
1	5.83
2	2.93
3	2.84
4	1.66
5	1.75
6	1.56
7	1.26
8	5.05

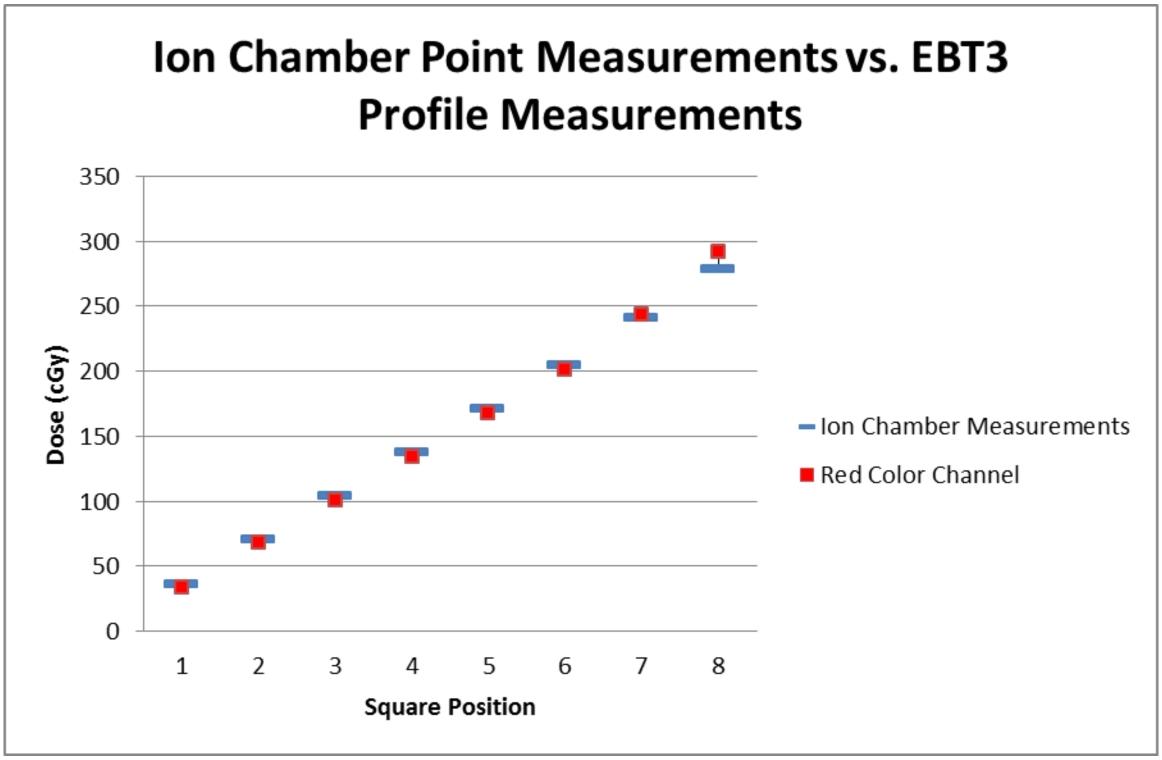

Figure 39: Graphical representation of the differences found between the ion chamber water tank point measurements and the EBT3 film dose profile measurements

Table 8: Tabular comparison of the ion chamber point measurements taken in a water tank and the EBT3 film measurements found using dose region squares.

Square #	Percent Difference (%) Red
1	5.27
2	2.79
3	2.94
4	1.52
5	1.63
6	0.88
7	0.89
8	5.52

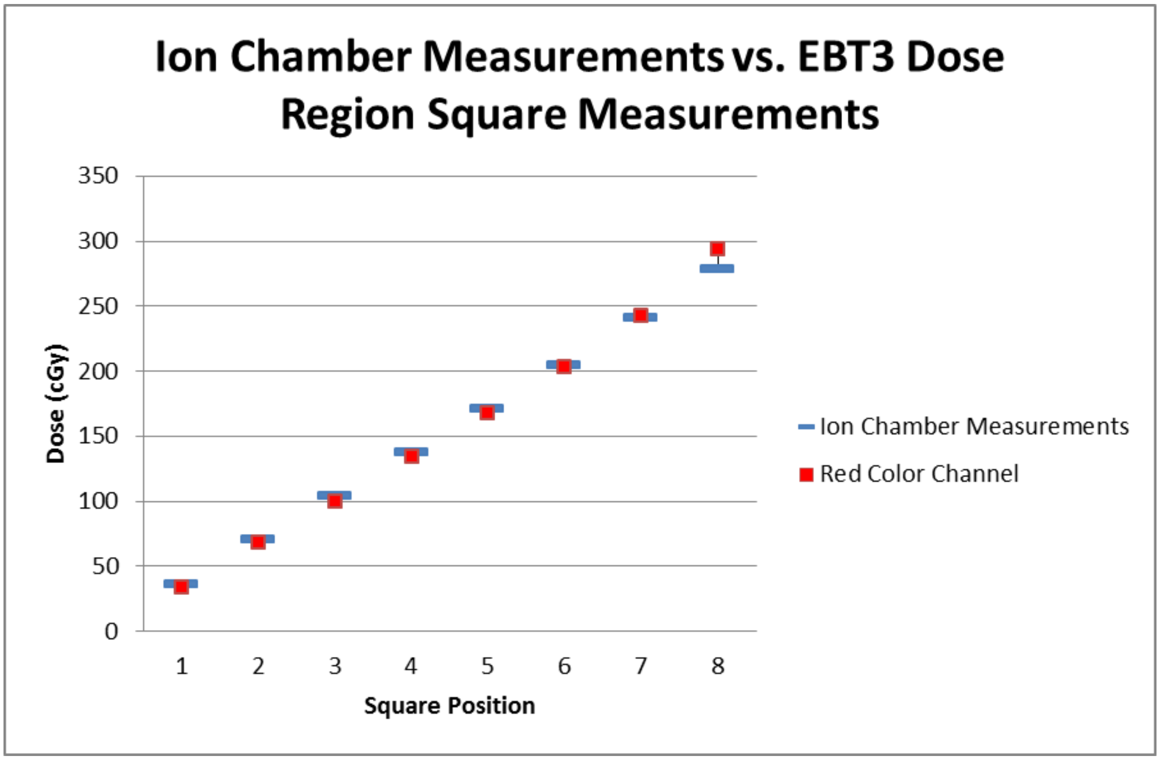

Figure 40: Graphical representation of the differences found between the ion chamber water tank point measurements and the EBT3 film dose region square measurements

The measurements aligned well with the greatest variation observed in the square 1 and 8 positions. This can be attributed to the physical location of the squares being close to the edge of the film. This larger variation is acceptable since the dose for these two squares were not close to the dose used for film measurements. The dose used for film measurements was 218 cGy (250 MU) which falls between the square 6 and square 7 doses. Since the differences at the square 6 and 7 positions were small, the film calibration was trusted for use with the film measurements. The film under-estimated the dose for all squares except 7 and 8 compared to the ion chamber measurements. Since these were the squares closest to the edges of the film and they were the furthest from the scanner center, measurements should only be taken away from the edges of the film and at the scanner center to minimize the effect of the edge of the film.

4.2.Stainless Steel and Titanium Rod Measurements

4.2.1. Dose Profiles for Stainless Steel and Titanium Rods

The following figure presents the raw data collected from FilmQA™ Pro. The error bars represent the 95% confidence based on the standard error and Gaussian statistics. The vertical black lines represent the position of the rod interface in relation to the profile. The re-buildup region is the region of increasing dose deposition following the local decrease observed just past the surface interfaces as indicated by the arrows in the following figure.

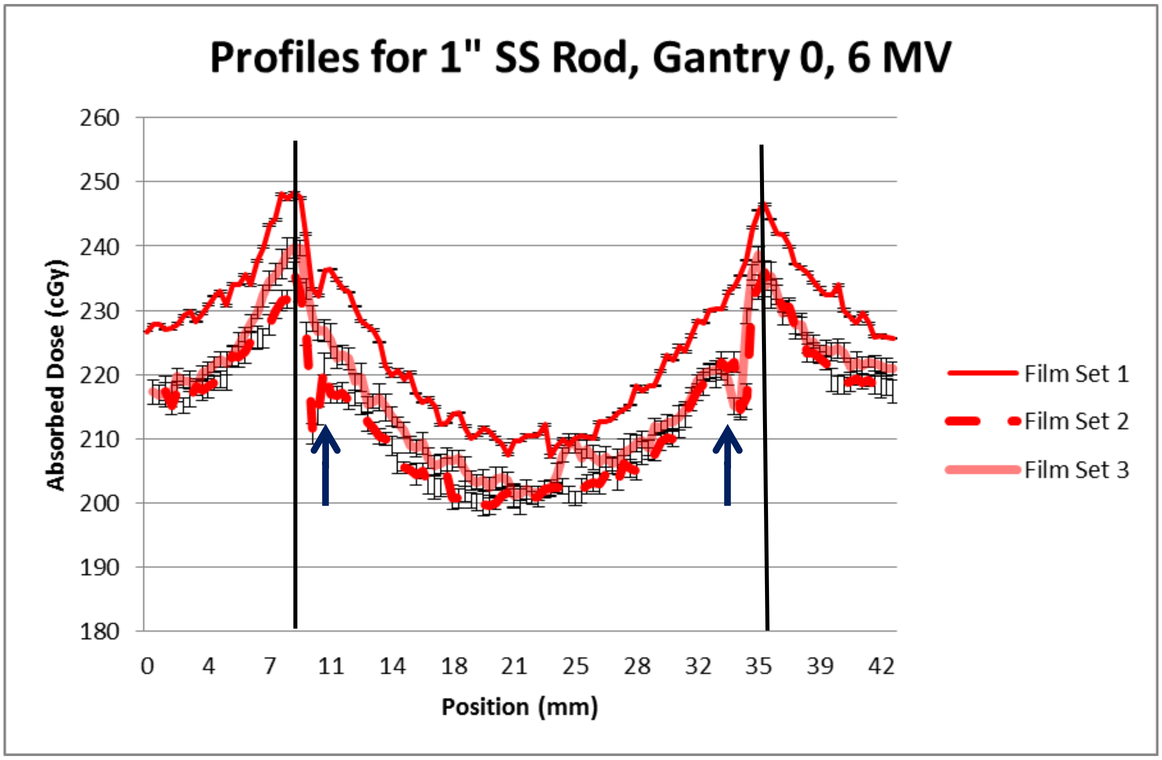

Figure 41: Raw profiles for the 1" SS Rod with gantry at 0° using 6 MV

The overall trends in the profile shapes were consistent with predictions described in TG-63 (Reft, Alecu et al. 2003). The shape of the dose profiles for the stainless steel and titanium rods also followed Monte Carlo predictions performed in previous studies (Keall, Siebers et al. 2003, Laub and Nusslin 2003). As presented in the raw profile plot for the 1” stainless steel rod above, there was some variation in the absolute dose observed between film sets. This can be attributed to a variation in film setup. The largest variation between film sets occurred with the first film set. The first film set resulted in a shift upward in the profile. The shape and trends between all three film sets matched. Given that the point of the experiment is to look at the relative perturbation in dose and not absolute values, the profiles were normalized to the maximum dose value.

The pixel range width of 10 was compared to the pixel range width of 70. This was performed to evaluate if widening the range would decrease the noise present in the profiles. The following two plots compare the normalized profiles using a pixel range width of 10 and 70.

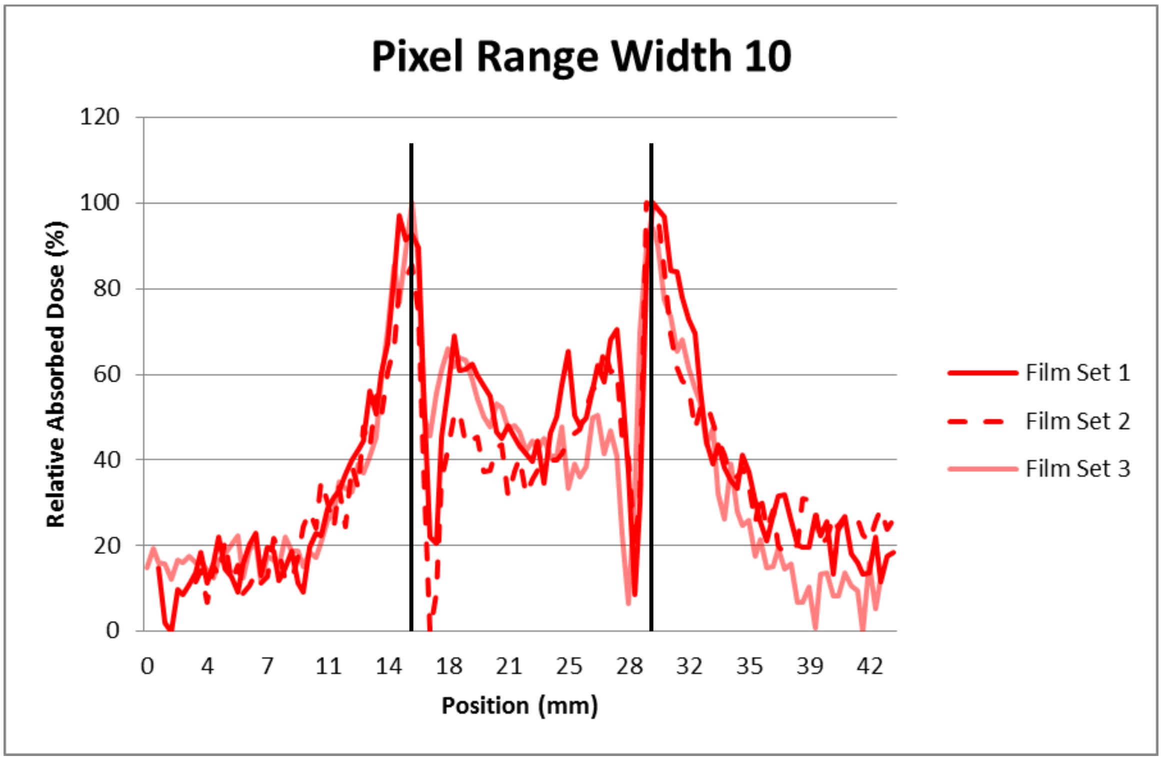

Figure 42: Normalized profiles for the 1/2" SS rod using 6 MV with the gantry at 0° using a pixel range width of 10

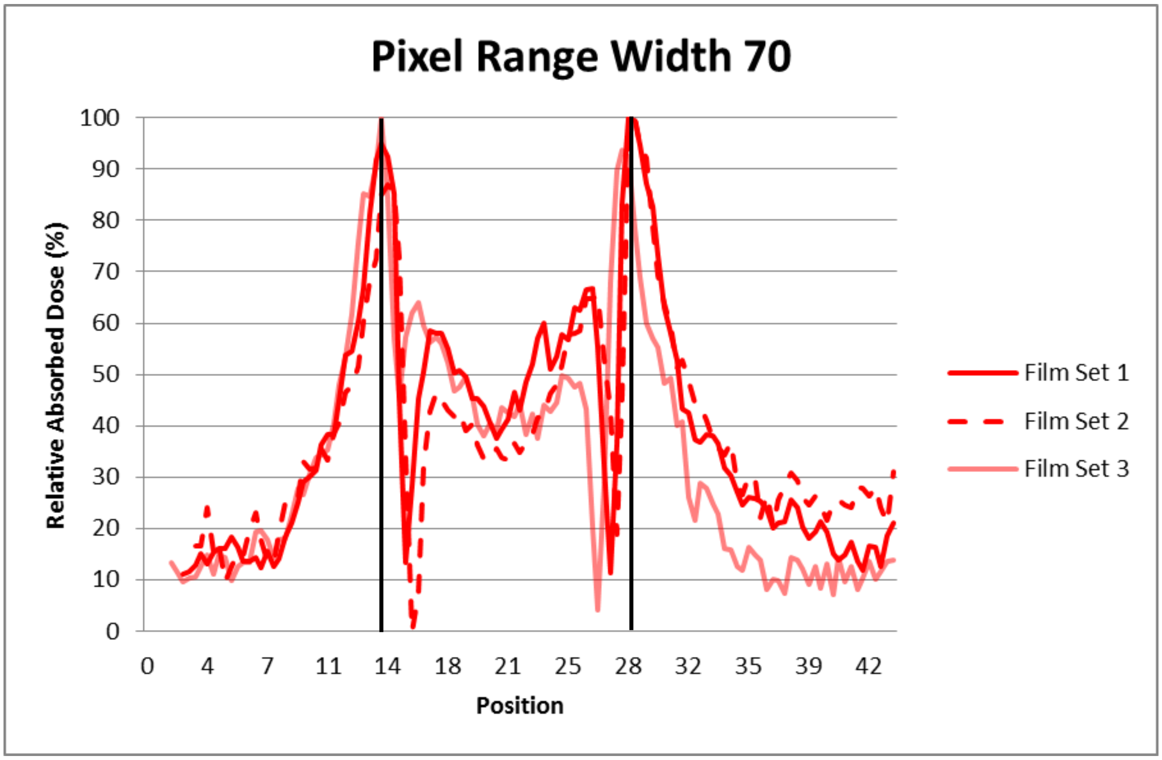

Figure 43: Normalized profiles for the 1/2" SS rod using 6 MV with the gantry at 0° using a pixel range width of 70

The following figure presents the average of the three film sets with the pixel range width of 10 and the average of the three film sets with the pixel range width of 70.

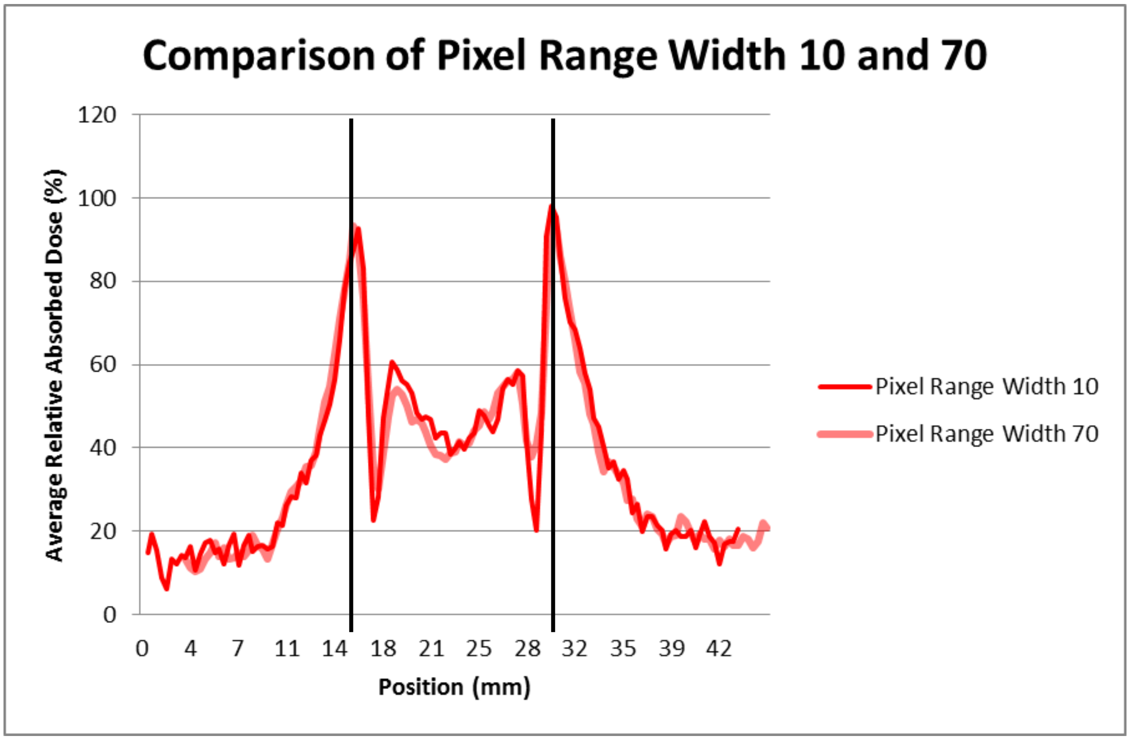

Figure 44: Comparison of the Pixel Range Width 10 and Pixel Range Width 70

The two different pixel range widths were compared by finding the average difference in the relative doses for the normalized profiles (the difference between pixel range width 10 and 70). The average difference was found to be 16.0. This indicates that there was very little reduction in the variation when increasing the pixel range width. With little reduction in the noise by increasing the pixel range width, the complete evaluation of the normalized profiles was completed using the pixel range width of 10 as advised by Ashland. Increasing the pixel range width without a considerable decrease in the noise dose bring up the possibility that the variance in the profiles may be due to the structure, chaotic or otherwise, and not noise alone. Further investigation fell outside the scope of this study.

4.2.2. Normalized Profiles

To remove the variations in the absolute data caused by variations in setup the profiles were normalized to the maximum dose value gathered from the three film sets. The resulting relative doses are relative to the maximum raw dose as a percent. The following figures represent the normalized profiles from each of the three set of film for each rod size, energy, and gantry position. These figures help to determine the reproducibility of the film measurements and the location of the interface point for each film set. The vertical black lines represent the position of the rod interface in relation to the profile.

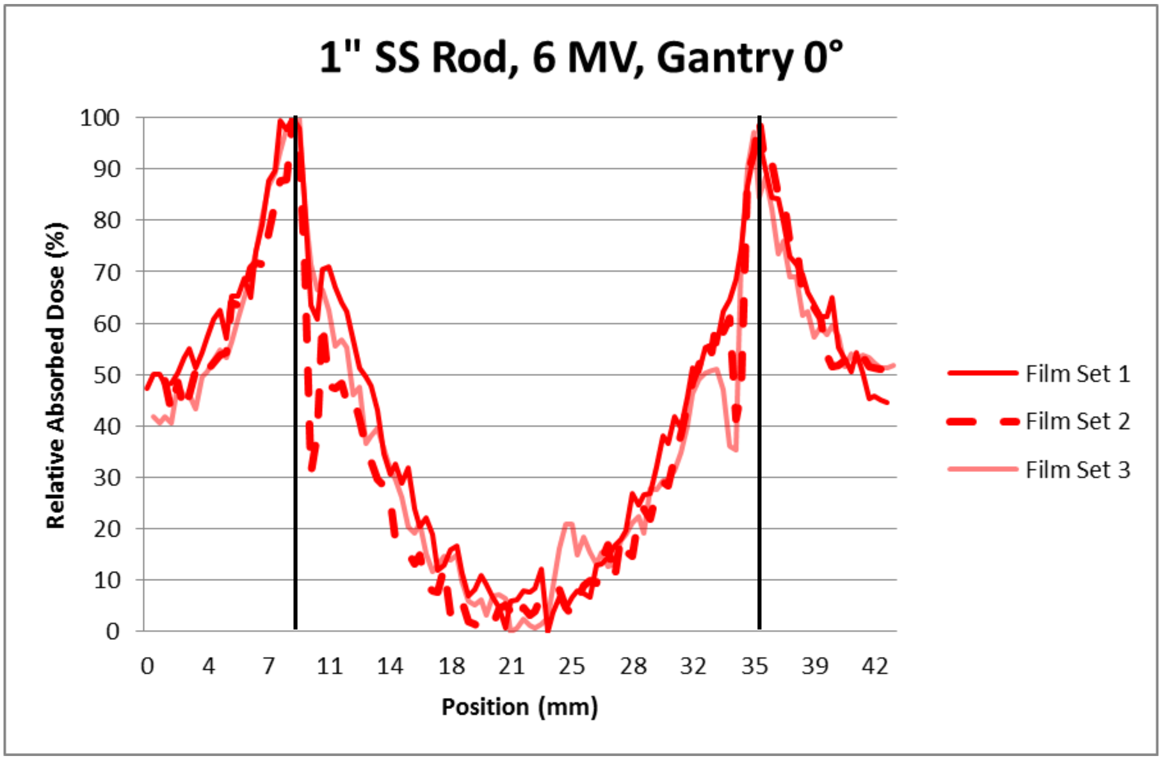

Figure 45: Normalized Profiles for the 1" SS Rod with Gantry at 0° using 6 MV

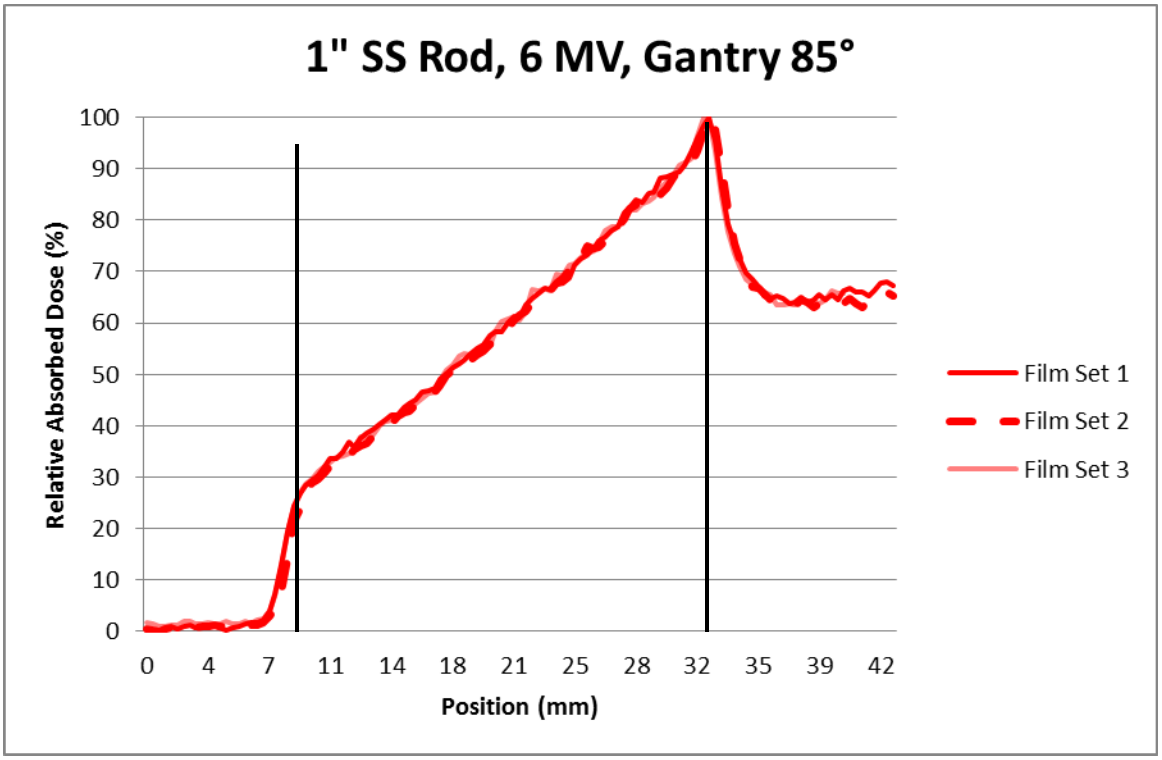

Figure 46: Normalized profiles for 1" SS rod with gantry at 85° using 6 MV

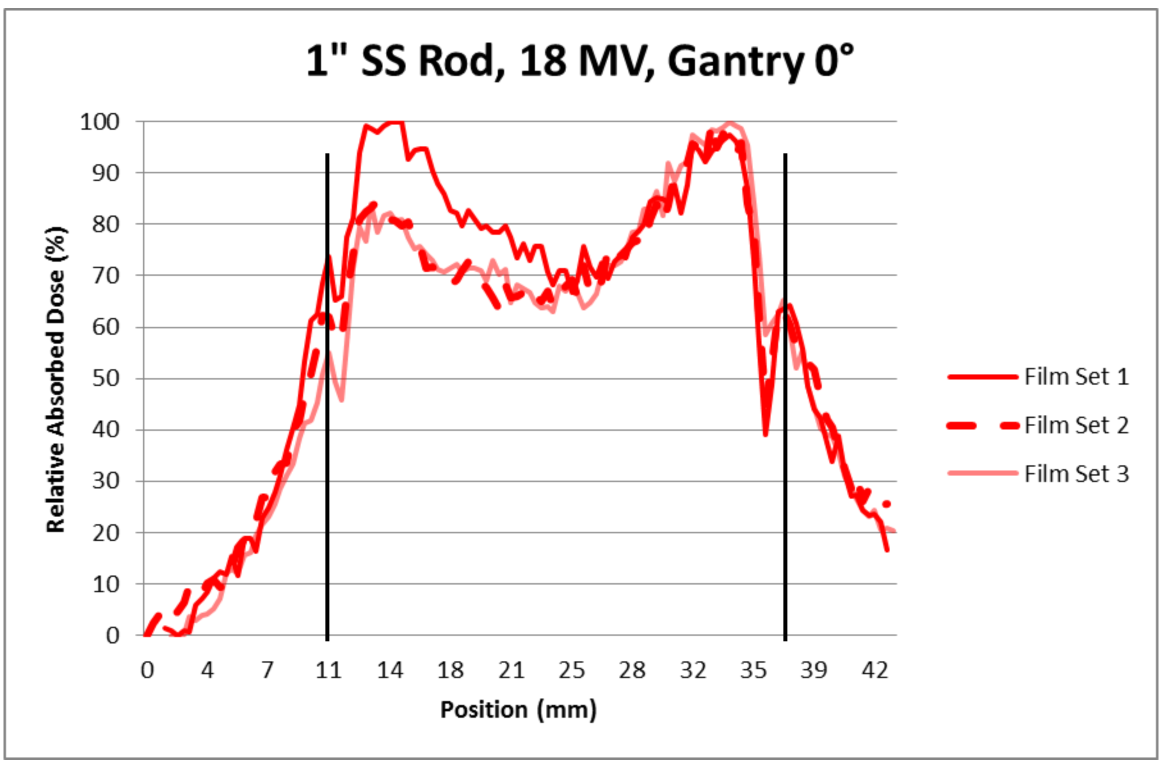

Figure 47: Normalized profiles for 1" SS rod with gantry at 0° using 18 MV

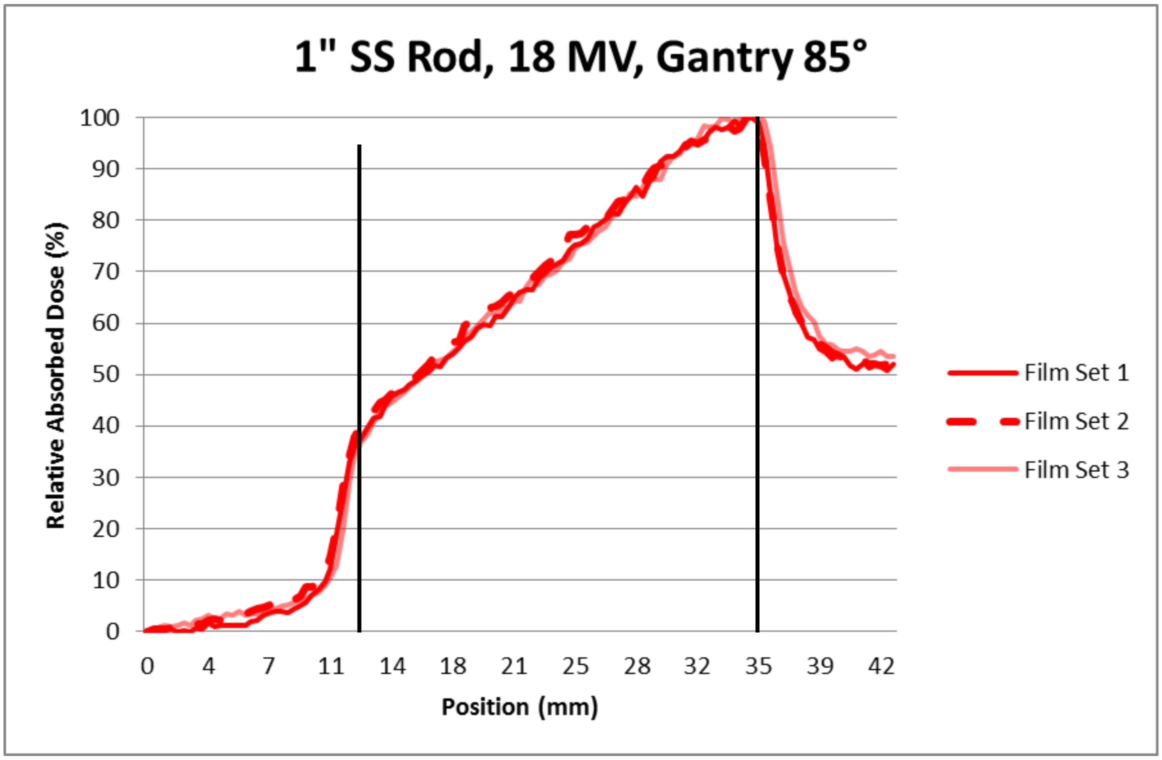

Figure 48: Normalized profiles for 1" SS rod with gantry at 85° using 18 MV

With the gantry at 0° for the 1" stainless steel rod, the relative dose increased approaching the left and right surface interfaces. This increase is due to the increased scattering of electrons in the stainless steel. After crossing the surface interface boundaries, there was a local decrease in relative dose before a re-build up region. The electrons that are laterally scattered also caused the local decrease since they were scattered out of the metal but not replenished by equal scatter in from the tissue. The slope of the local decrease in relative dose was very steep for both the 6 and 18 MV photon beams. With the high density stainless steel, the electrons laterally scattered very close to the surface interface causing the very steep local decrease before the re-buildup region. The magnitude of the local decrease after crossing the surface interface appeared to be greater with the 6 MV beam compared to the 18 MV photon beam. This can be attributed to the larger dose deposition at the surface interface with the 6 MV photon beam compared to the 18 MV photon beam. Also, the Compton scatter interactions have a forward bias of the scattered photons at higher energies (Attix, 2004). For lower energies, as seen with 6 MV, the photoelectrons from photoelectric interactions are predominantly ejected sideways resulting in the greater local decrease after crossing the interface (Attix, 2004). With an increased energy, as seen with 18 MV, the photoelectrons are ejected more toward smaller angles resulting in a smaller local decrease (Attix, 2004). The larger dose deposition at the interface results in greater lateral electron scatter.

The 1” stainless steel rod with 6 MV continued to increase in relative dose after the re-buildup region only shortly before decreasing approaching the center of the rod. The 1” stainless steel rod with 18 MV followed a similar trend but continued to increase following the re-buildup region longer before decreasing approaching the center of the rod due to the greater penetrative ability of the 18 MV photon beam than the 6 MV photon beam. Moving towards the center of the rod, the thickness increases. The 6 MV photon beam deposited more dose at the thinner edges of the rod instead of at the thicker center of the rod due to the weaker penetrability of the 6 MV beam. The increased center thickness of the 1” stainless steel rod somewhat suppressed the ability of the 18 MV photon beam to penetrate and deposit a large percentage of dose at the film at the center of the rod. Instead, the 18 MV photon beam deposited more dose closer to the edges of the rods. The 18 MV beam did deposit more dose further in from the surface edges of the rod compared to the 6 MV beam due to the increased penetrability of the 18 MV beam. These trends were observed in the 1” stainless steel rod due to the larger density of the material and the larger diameter of the rod.

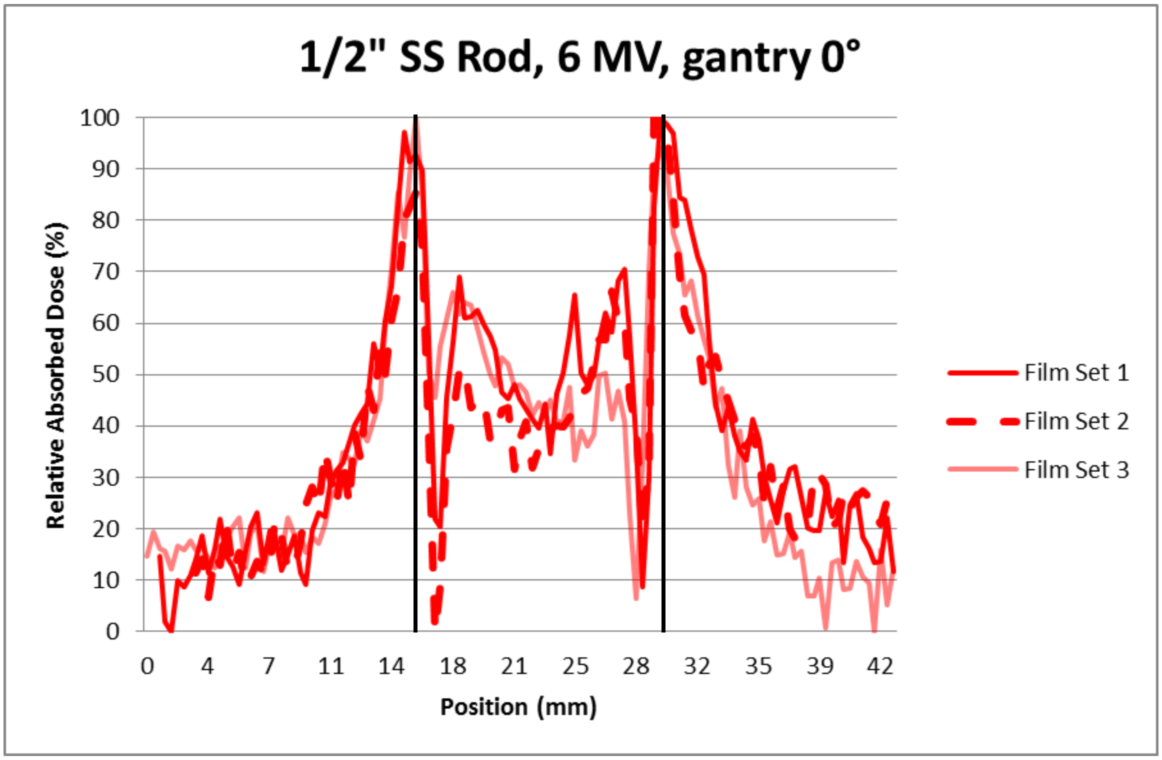

Figure 49: Normalized profiles for 1/2" SS rod with gantry at 0° using 6 MV

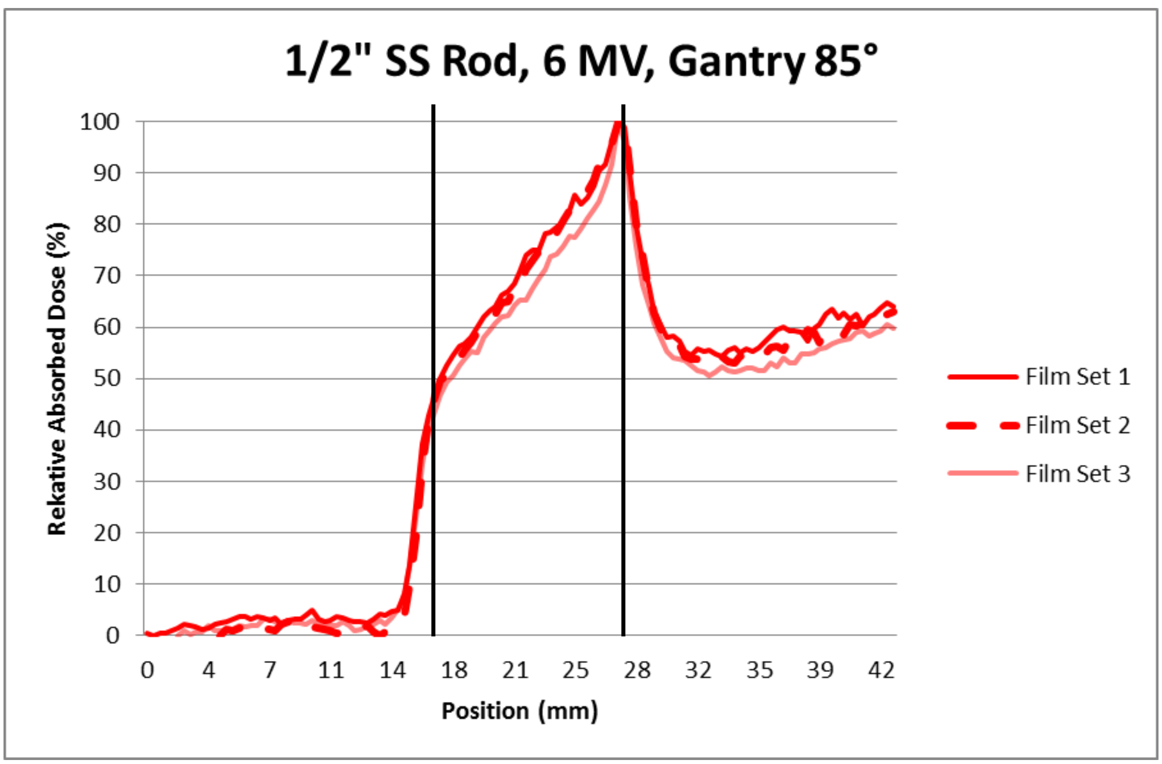

Figure 50: Normalized profiles for 1/2" SS rod with gantry at 85° using 6 MV

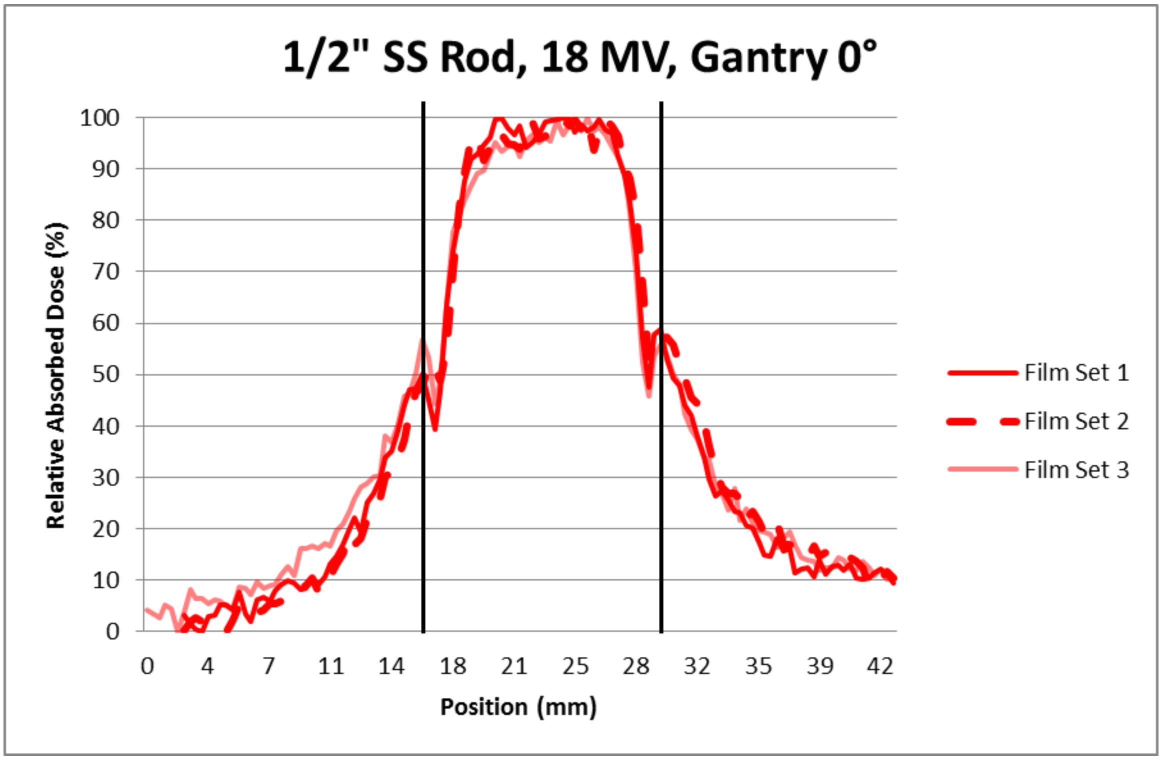

Figure 51: Normalized profiles for 1/2" SS rod with gantry at 0° using 18 MV

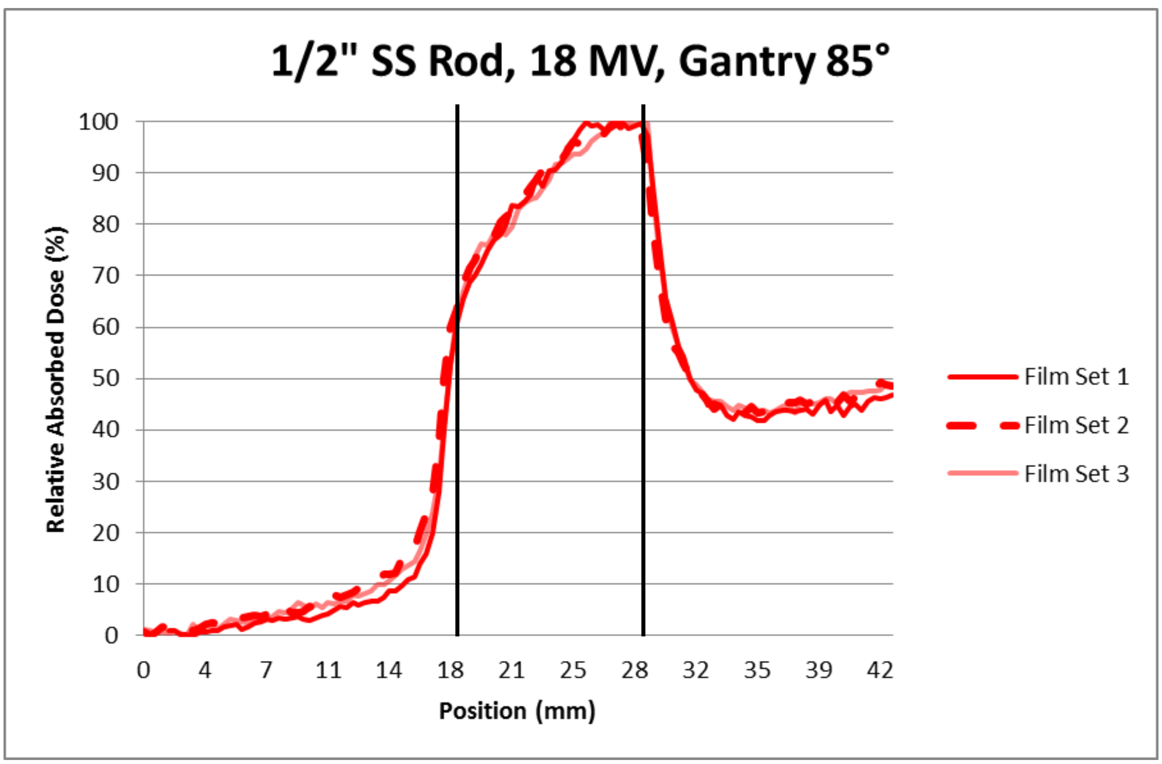

Figure 52: Normalized profiles for 1/2" SS rod with gantry at 85° using 18 MV

With the gantry at 0°, the ½" stainless steel rod with 6 MV only increased after the re-buildup region very shortly followed by a decrease in relative dose approaching the center of the rod. The ½" stainless steel rod with 18 MV resulted in a plateau at the center of the rod after the re-buildup region. This is attributed to the smaller diameter and thickness of the ½" stainless steel rod. The 18 MV beam was able to penetrate and deposit more dose at the center of the ½" rod due to the smaller diameter and thickness of the rod at the center compared to the 1" rod. The smaller rod had less high density material to impede the 18 MV photon beam.

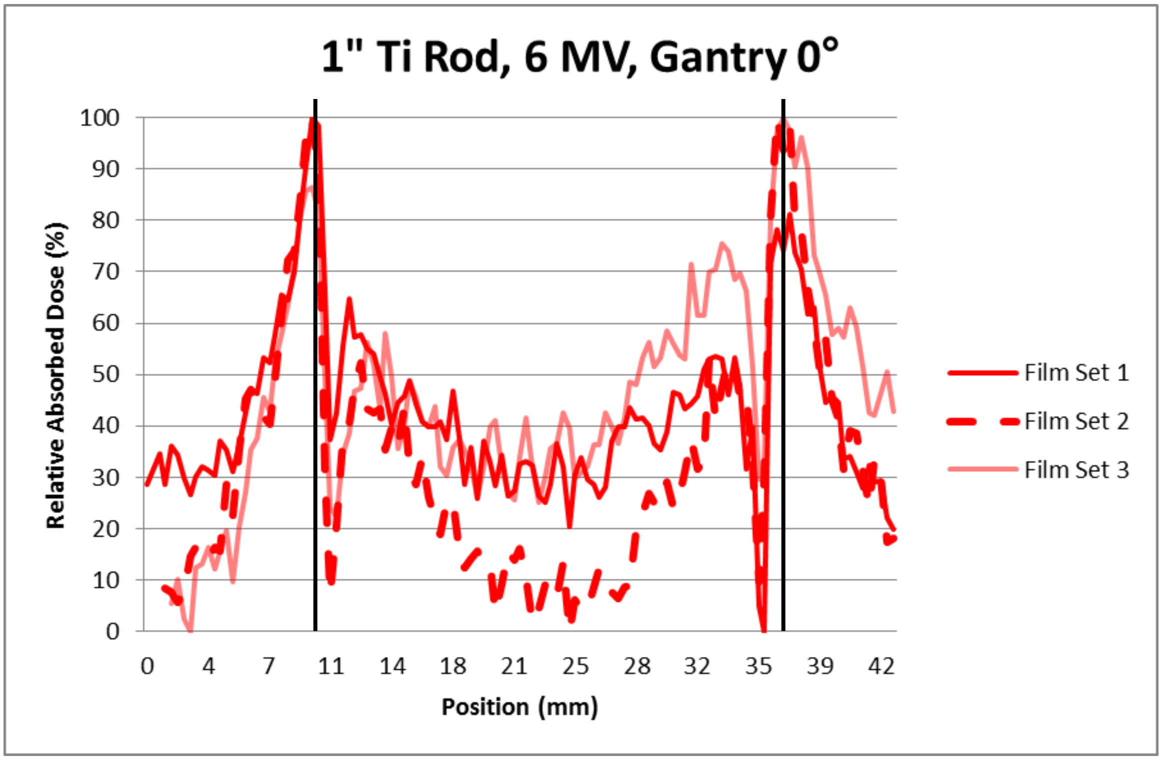

Figure 53: Normalized profiles for 1" Ti rod with gantry at 0° using 6 MV

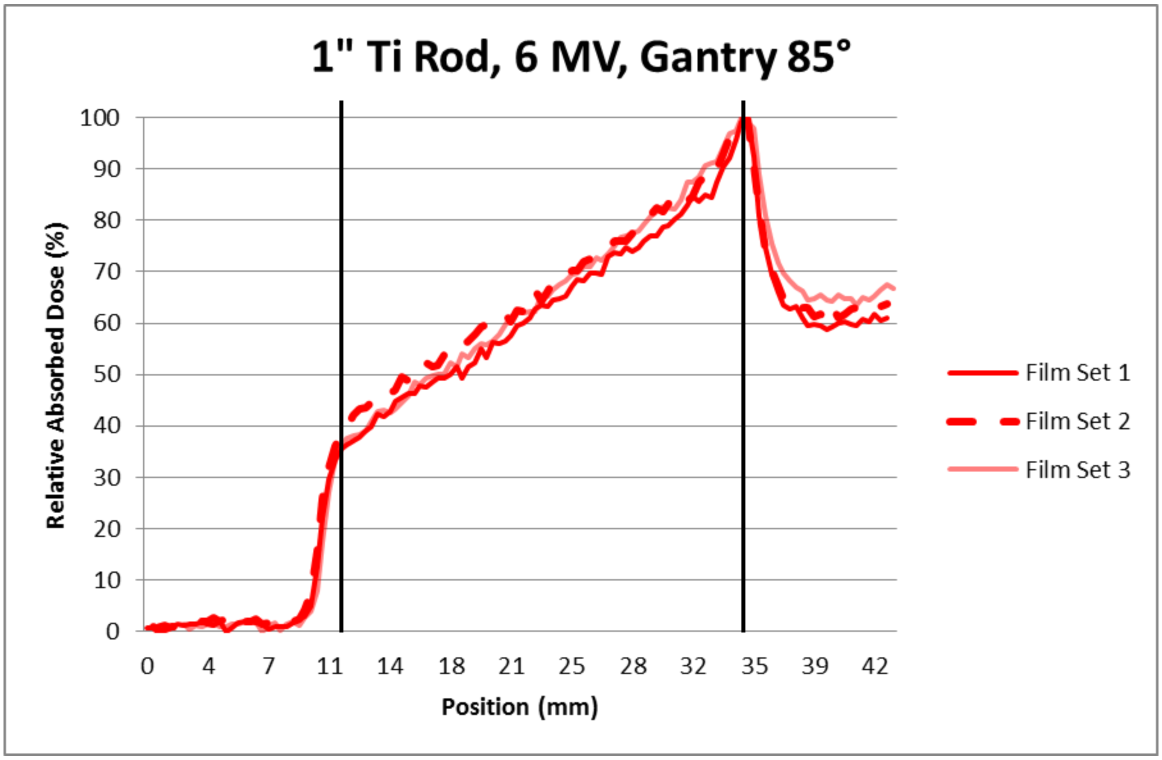

Figure 54: Normalized profiles for 1" Ti rod with gantry at 85° using 6 MV

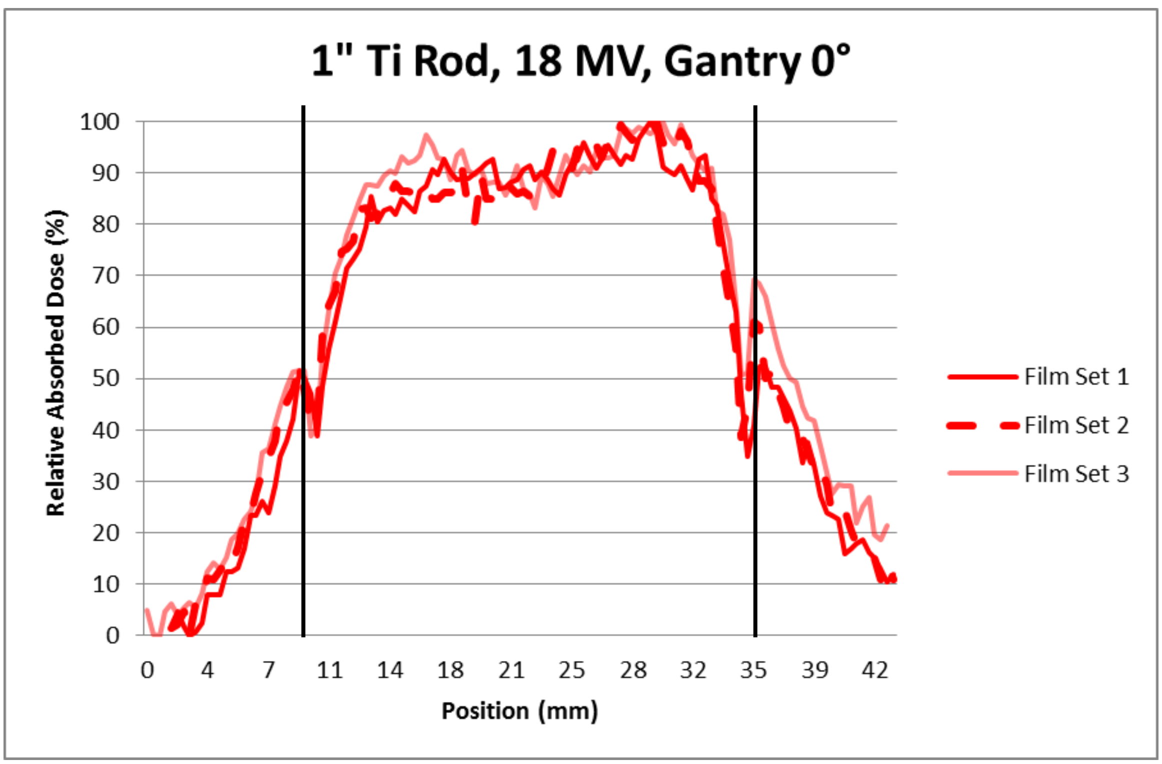

Figure 55: Normalized profiles for 1" Ti rod with gantry at 0° using 18 MV

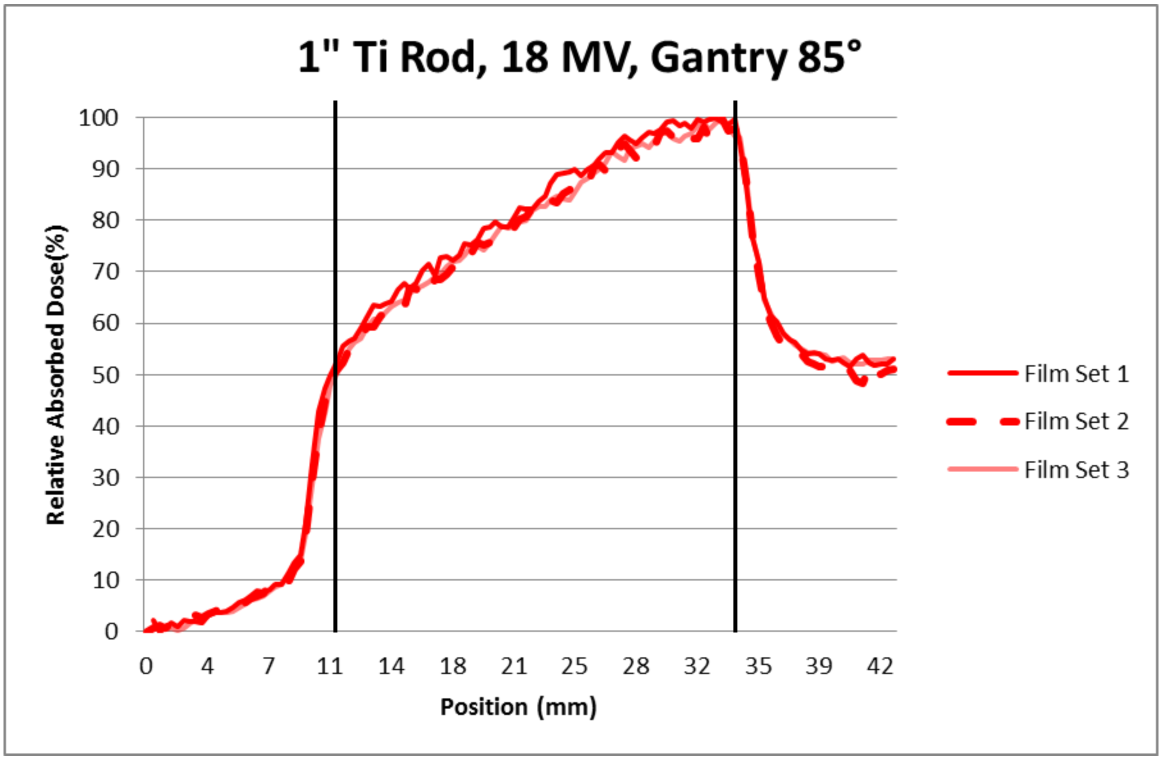

Figure 56: Normalized profiles for 1" Ti rod with gantry at 85° using 18 MV

With the gantry at 0°, the 1" titanium rod profile trends were similar to the stainless steel profile trends with small differences. The central rod dose decrease of the 1" titanium rod with 6 MV was not as pronounced as the central rod dose decrease of the 1" stainless steel rod. This can be attributed to the smaller density of titanium in comparison to stainless steel. The plateau seen with 18 MV has a slight dip at the very center of the 1" titanium rod whereas the ½" stainless steel rod did not due to the lower density and larger diameter of the 1" titanium rod. The lower density of the 1" titanium rod allowed for a greater dose deposition at the center of the rod compared to the higher density stainless steel rods. The larger diameter of the 1" titanium rod slightly impedes the 18 MV from depositing dose. The 1" titanium rod profiles resemble the ½" stainless steel profiles more than the 1" stainless steel rod profiles due to the combined effects of the lower density and larger diameter. According to the Fano and O'Connor theorems, the density and size scale in the same proportion (Papanikolaou et al. 2004). This means that a slab of density D and thickness X will scatter and attenuate the same as half the density (D/2) and twice the thickness (2X) (Papanikolaou et al. 2004). The density of titanium is slightly less than half the density of stainless steel, and the 1” diameter of the titanium rod is twice the thickness of the ½” stainless steel rod; therefore, the 1” titanium rod will scatter and attenuate approximately the same or very similar to the ½” stainless steel rod.

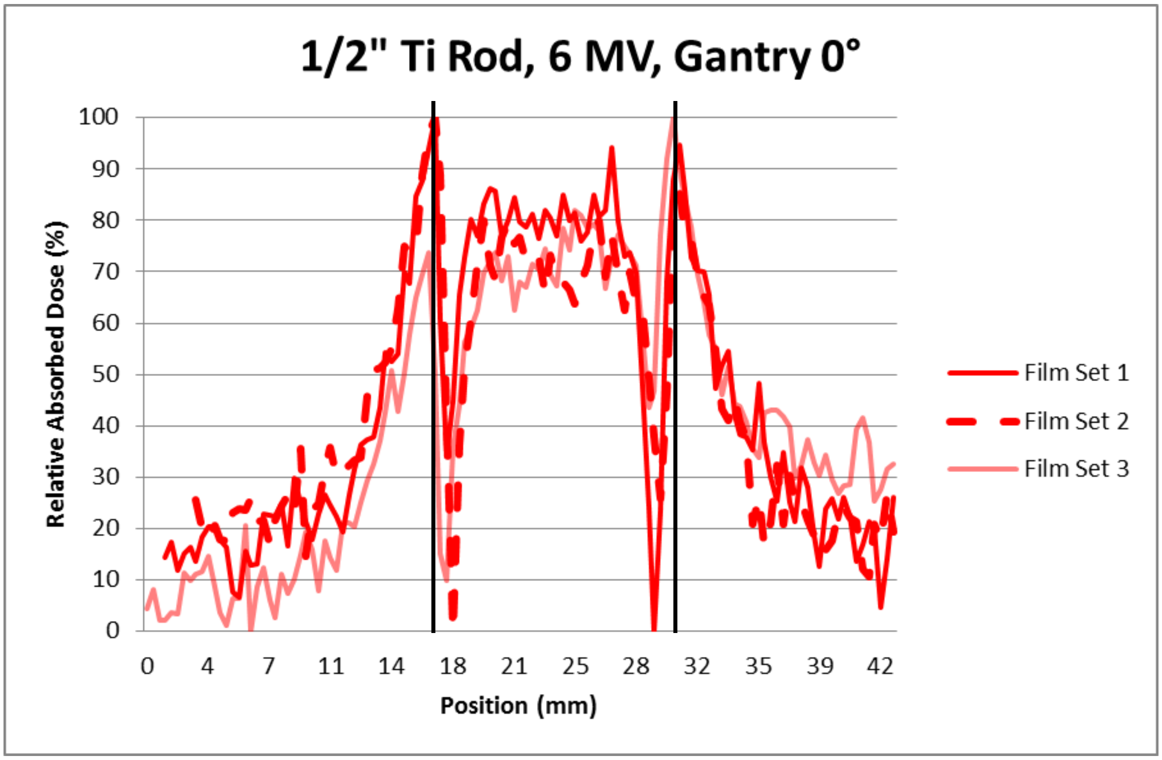

Figure 57: Normalized profiles for 1/2" Ti rod with gantry at 0° using 6 MV

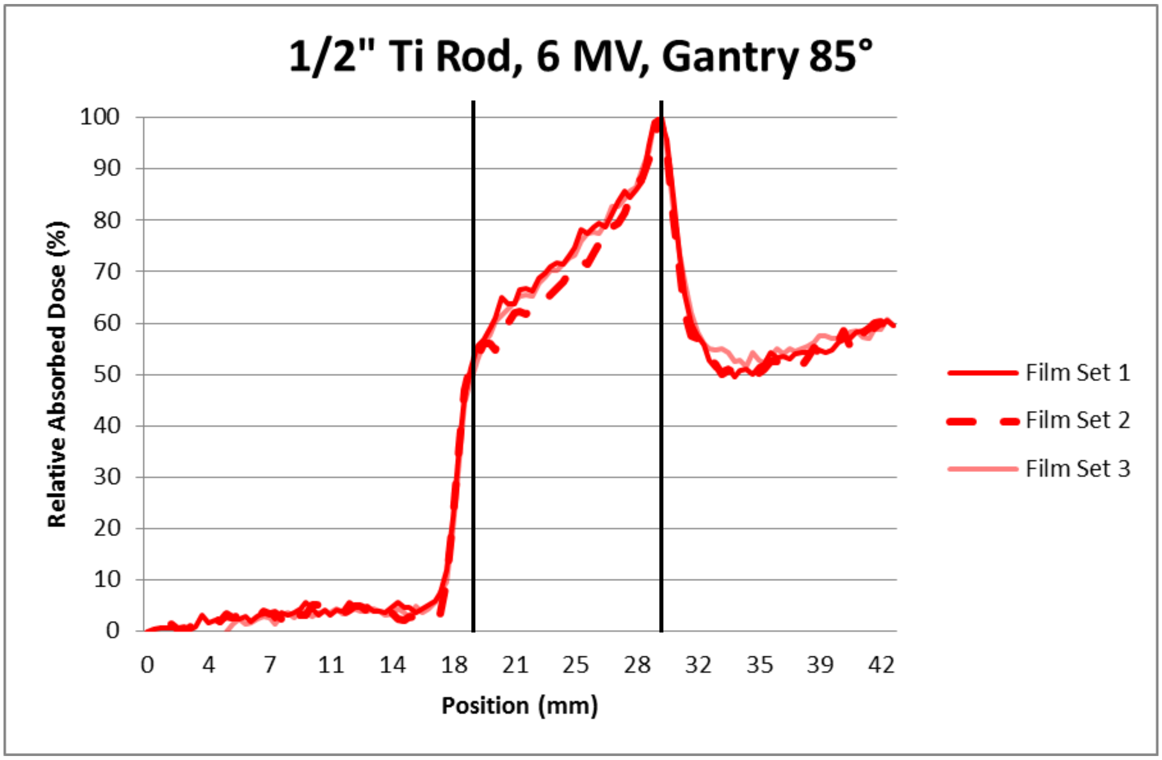

Figure 58: Normalized profiles for 1/2" Ti rod with gantry at 85° using 6 MV

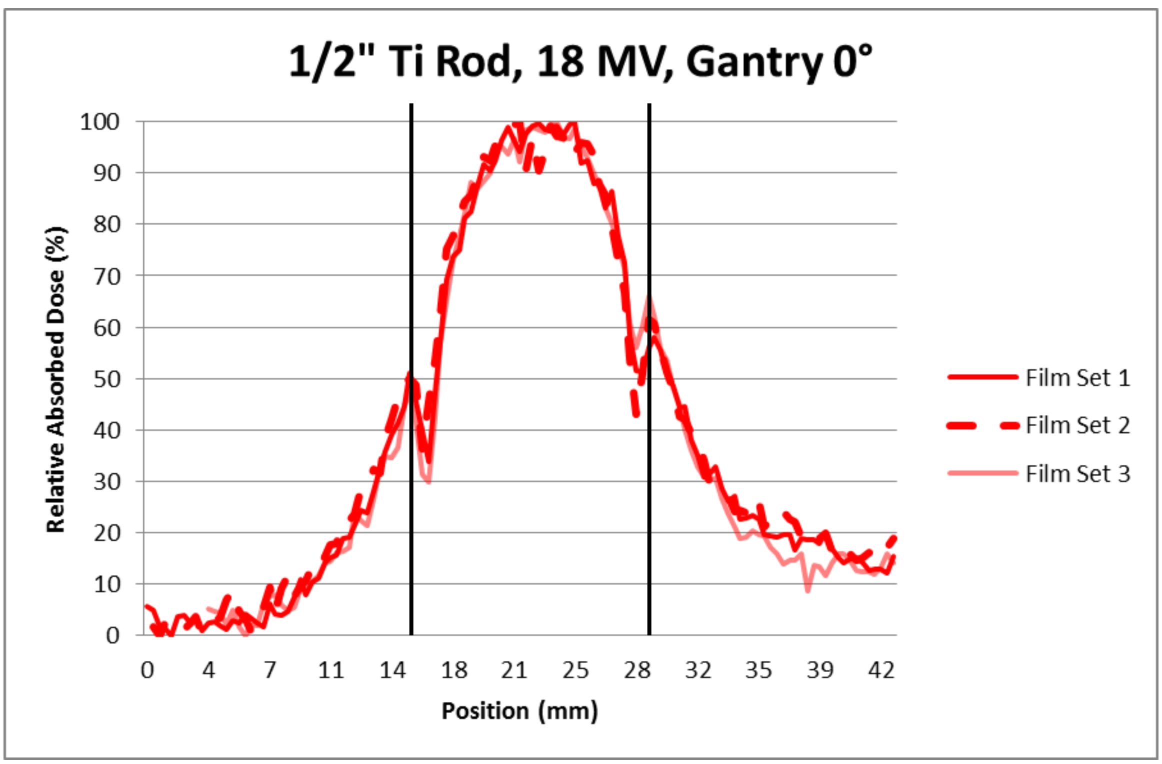

Figure 59: Normalized profiles for 1/2" Ti rod with gantry at 0° using 18 MV

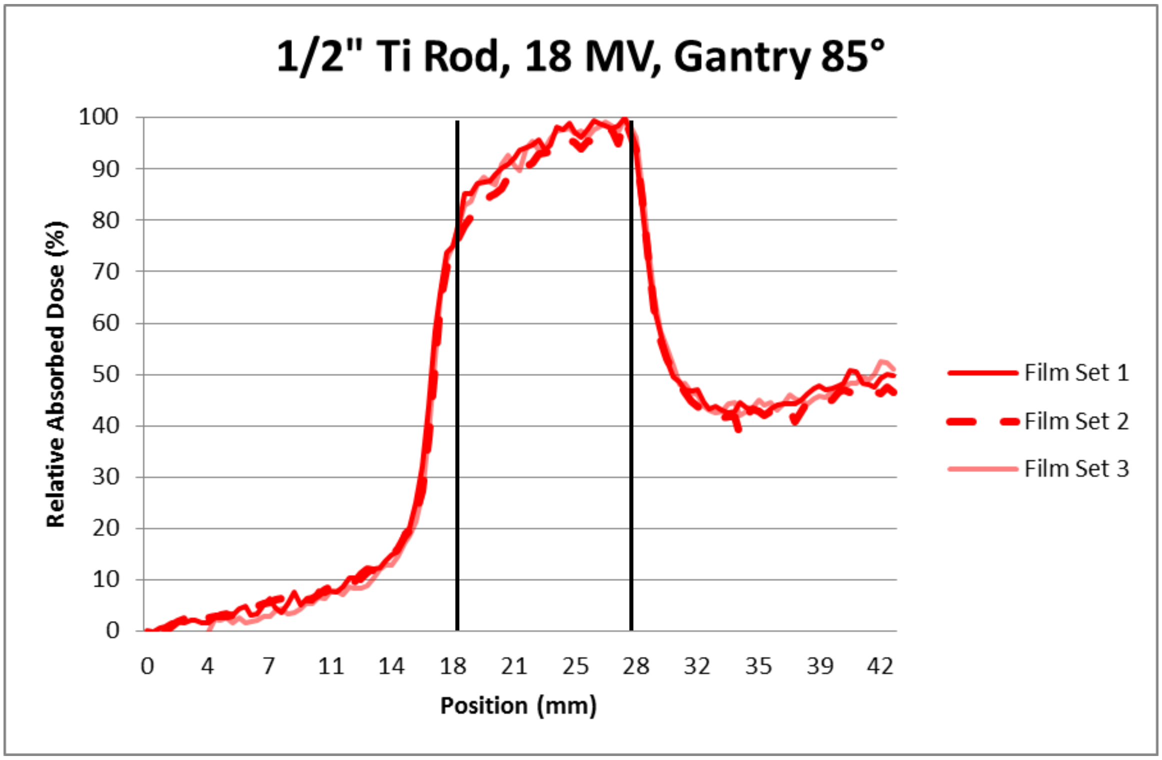

Figure 60: Normalized profiles for 1/2" Ti rod with gantry at 85° using 18 MV

As expected, the ½" titanium rod profiles trends at gantry 0° varied from the 1" titanium rod profile trends in a similar fashion as the stainless steel rods. With the smaller diameter and thickness of the ½" titanium rod, a central rod dose deposition plateau was observed with the 6 MV and the 18 MV. The 18 MV plateau was not as flat and almost appears as peak dose deposition at the center of the rod due to the greater penetrative ability of the 18 MV photon beam in the smaller diameter and less dense ½" titanium rod compared to the 1" titanium rod and the stainless steel rods.

With the gantry at 85°, the dose peaked at the entrance surface interface of the rods with a gradual decline in dose moving through the rod and a marked decrease in dose as the photon beam exited the rods. The peak at the entrance surface interfaces can be attributed to backscatter caused by the high-Z materials of the rods. Much more pronounced peaks were observed with the 6 MV photon beam, and slightly more rounded peaks were observed with the 18 MV photon beam. These findings were due to the greater forward penetration of the 18 MV beam compared to the 6 MV beam. The high-

Z of the stainless steel and titanium rods caused the photon spectrum to be attenuated more by photoelectric and pair production interactions and less by Compton scatter than an equivalent mass of water (Keall, Siebers et al. 2003). The shape and reproducibility of the 85° profiles were evaluated in this study. The 85° profiles could be used to evaluate the attenuation through the rods but this task fell outside the scope of this study.

The slope of the local decrease in dose was very steep for both the 6 and 18 MV photon beams for both stainless steel and titanium rods meaning the maximum local decrease in dose occurred near the surface interface. With the high density stainless steel and titanium, the electrons laterally scattered very close to the surface interface resulting in the very steep local decrease before the re-buildup region. The following table presents the depth of the maximum point of the local decrease into the rods:

Table 9: Depth of local decrease into the rods before re-buildup region

Rod	Energy	Average Depth of Local Decrease (mm)
1" SS	6	0.90
1" SS	18	0.71
1/2" SS	6	0.90
1/2" SS	18	0.68
1" Ti	6	1.38
1" Ti	18	0.55
1/2" Ti	6	1.38
1/2" Ti	18	0.86

Overall, the 6 MV beam results in a greater depth of the local decrease into the rods before the re-buildup regions begin. The greater dose deposition at the surface interfaces with the 6 MV beam resulted in a greater amount of laterally scattered electrons. With the increase in the amount of laterally scattered electrons, there will be a greater depth of the local decrease into the rods. The size of the rod had very little to no impact on the depth of the local decrease for both the stainless steel and titanium rods. The less dense titanium rod resulted in a larger depth of the local decrease when compared to the stainless steel rods.

4.2.3. Interface Dose Measurements for Stainless Steel and Titanium Rods

The following table presents the average relative interface dose measurements for the stainless steel and titanium rods found using the EBT3 film. The dose measurements are relative to the maximum raw dose. The measurements were found by evaluating the normalized profile data for each film set for each rod, size, and energy to determine the interface locations (left and right). After determining the location of the interface along the profile, the average relative interface dose was calculated from the three film sets. This provided the average relative interface dose for each rod. The smaller interface position value represents the left surface interface of the rods, and the larger interface position value represents the right surface interface of the rods.

Table 10: Average relative interface dose for the stainless steel and titanium rods

Rod Type	Energy	Position along Profile (mm)	Average Relative Interface Dose (%)
1" SS	6	8.8	96.38
1" SS	6	35.3	94.52
1" SS	18	10.6	63.48
1" SS	18	36.7	61.70
1/2" SS	6	15.5	92.71
1/2" SS	6	29.3	90.77
1/2" SS	18	15.9	51.51
1/2" SS	18	29.6	57.25
1" Ti	6	9.2	90.66
1" Ti	6	37.0	92.45
1" Ti	18	8.8	51.67
1" Ti	18	35.3	56.96
1/2" Ti	6	15.9	82.08
1/2" Ti	6	30.3	89.44
1/2" Ti	18	15.2	49.40
1/2" Ti	18	28.9	61.16

There were larger relative doses at the surface interfaces for the 6 MV photon beam than the 18 MV photon beam for both stainless steel and titanium. This is attributed to the greater penetrability of the 18 MV beam than the 6 MV beam. The stainless steel and titanium surface interfaces impeded the 6 MV beam more than the 18 MV beam resulting in a greater dose deposition from the 6 MV beam.

The larger rod diameters resulted in larger relative dose at the surfaces interfaces for both stainless steel and titanium. With a larger diameter, the surface interfaces will be larger. The larger surface interfaces increase the surface area of the high-Z materials the beam interacts with at the interface.

The relative interface doses were larger for the stainless steel rods than the titanium rods. This trend can be attributed to the larger density of stainless steel than titanium. Greater mass density is associated with a greater electron density relative to water. A larger dose deposition will occur in materials with the larger relative electron density and a greater amount of scattered secondary radiation, particularly electrons.

4.2.4. Verification of Gafchromic™ EBT3 Measurements to Pinnacle^3 Calculated Dose

The following table presents the calculated Pinnacle^3 dose values calculated away from the stainless steel and titanium rods compared to the distant ambient field EBT3 film measurements. These comparisons provide a verification of Pinnacle^3's ability to accurately calculate dose away from high density materials. The doses from the film were gathered from the raw profile data for comparison to Pinnacle^3 measurements. The plot presents the average dose values in the distant ambient field from Pinnacle^3 to the EBT3 film for a better understanding of the comparison. The lines represent the difference between the two measurements types.

Table 11: Comparison of Pinnacle[3] Calculated Distant Ambient Field Dose and EBT3 Film Distant Ambient Field Measurements

Rod Type	Energy	Percent Difference (%)
1" SS	6	1.21
1" SS	18	1.63
1/2" SS	6	0.63
1/2" SS	18	0.76
1" Ti	6	1.19
1" Ti	18	2.66
1/2" Ti	6	0.85
1/2" Ti	18	0.99

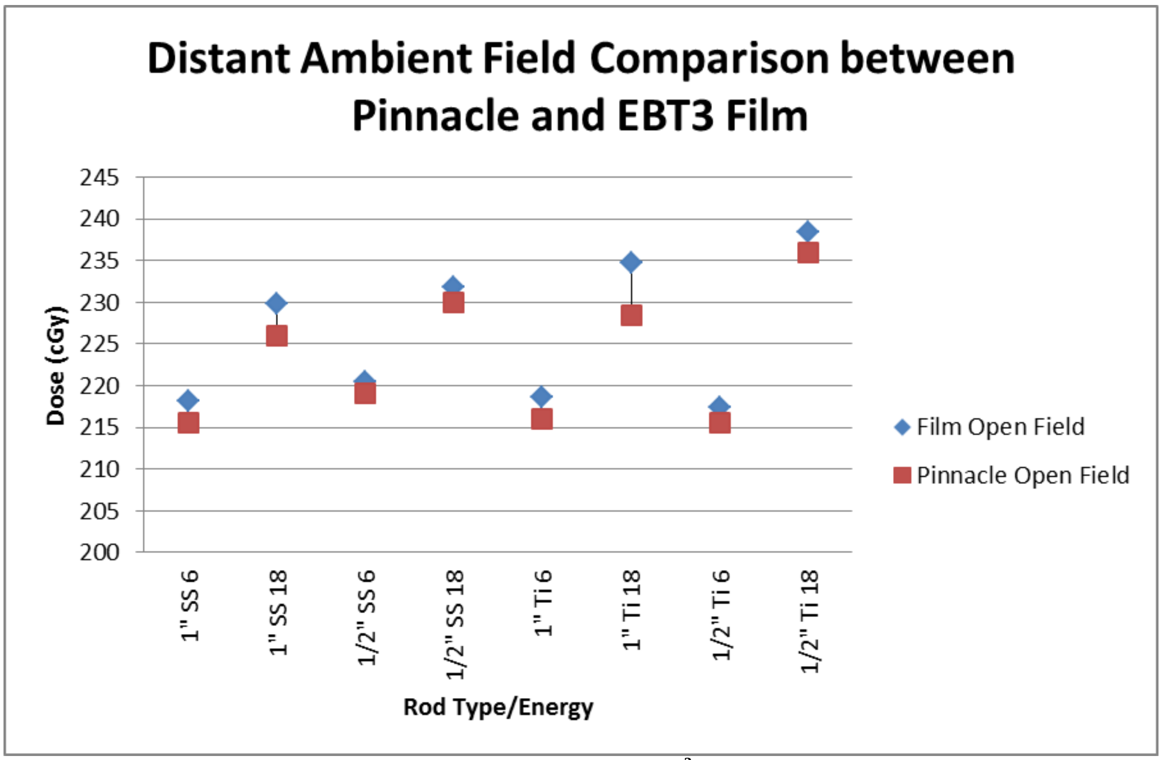

Figure 61: Distant Ambient Field comparison between Pinnacle[3] point calculations and film measurements

The table and plot show that Pinnacle[3] and the film distant ambient field measurements match quite well. All of the comparisons provided evidence of very good agreement between Pinnacle[3] and the film for distant ambient field measurements. This supported that Pinnacle[3] is accurate in calculating dose away from a high-Z material.

The following table presents the calculated Pinnacle^3 dose values at the interface of the high density stainless steel and titanium rods compared to the interface measurements gathered from the EBT3 film. These comparisons provide evidence of the inaccuracy of the algorithm used in Pinnacle^3 to calculate dose near high density interfaces. The plot presents the average dose values at the interface from Pinnacle^3 to the EBT3 film for a better understanding of the comparison. The lines represent the difference between the two measurements types.

Table 12: Comparison of Pinnacle^3 Average Calculated Interface Dose and EBT3 Average Film Interface Measurements

Rod Type	Energy	Percent Difference (%)
1" SS	6	3.07
1" SS	18	9.77
1/2" SS	6	3.49
1/2" SS	18	2.68
1" Ti	6	16.30
1" Ti	18	10.20
1/2" Ti	6	5.11
1/2" Ti	18	5.07

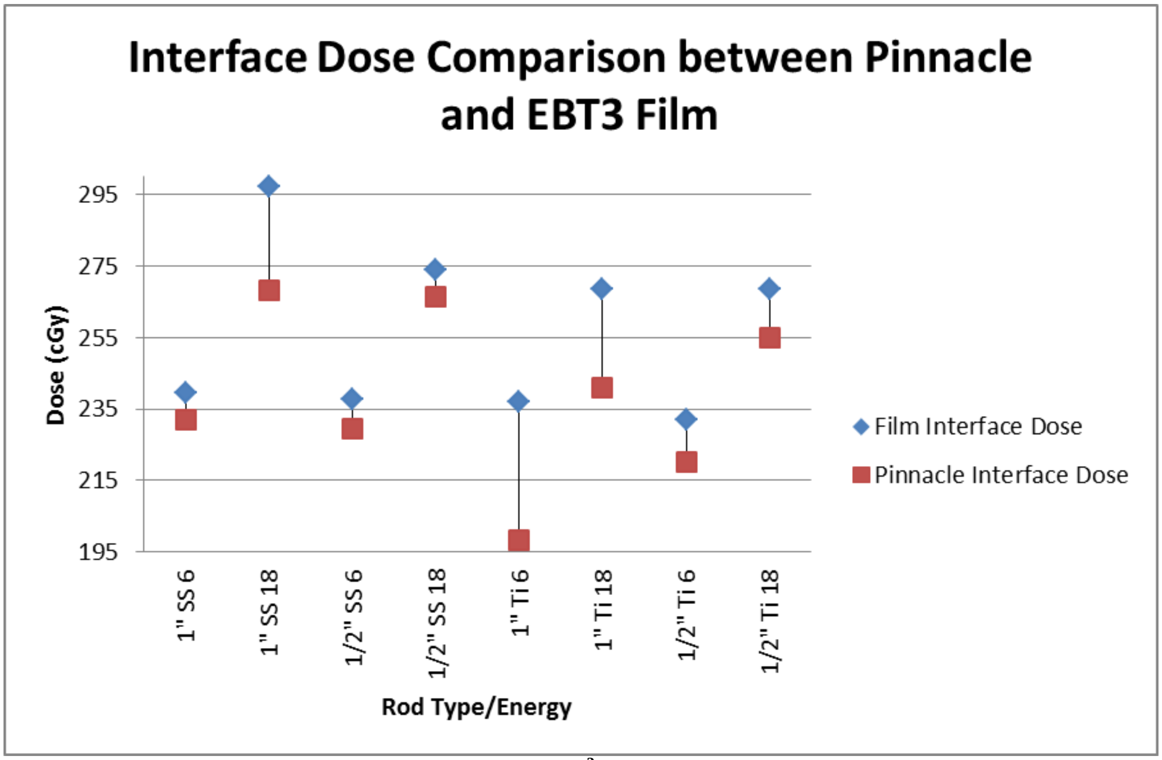

Figure 62: Comparison of interface Pinnacle[3] calculation points and film measurements

There were larger discrepancies between the film and Pinnacle[3] in the interface dose values. This provided evidence that Pinnacle[3] did not consistently and accurately calculate the dose near high-Z materials. Pinnacle[3] used a convolution-superposition dose calculation algorithm. As discussed earlier, convolution-superposition dose calculation algorithms are limited in the ability to accurately calculate the dose at high-Z interfaces. These limitations are due to the inability to accurately model the coupled photon-electron transport across the interface (Apipanyasopon 2012).

4.3. Hip Stem Measurements

4.3.1. Dose Profiles with Tri Lock® and AML® Hip Stems

The following figure presents the raw data collected from FilmQA™ Pro. The error bars represent the 95% confidence based on the standard error and Gaussian statistics. The vertical black lines represent the position of the rod interface in relation to the profile. The re-buildup region is the region of increasing dose deposition following the local decrease observed just past the surface interfaces as indicated by the arrows in the following figure.

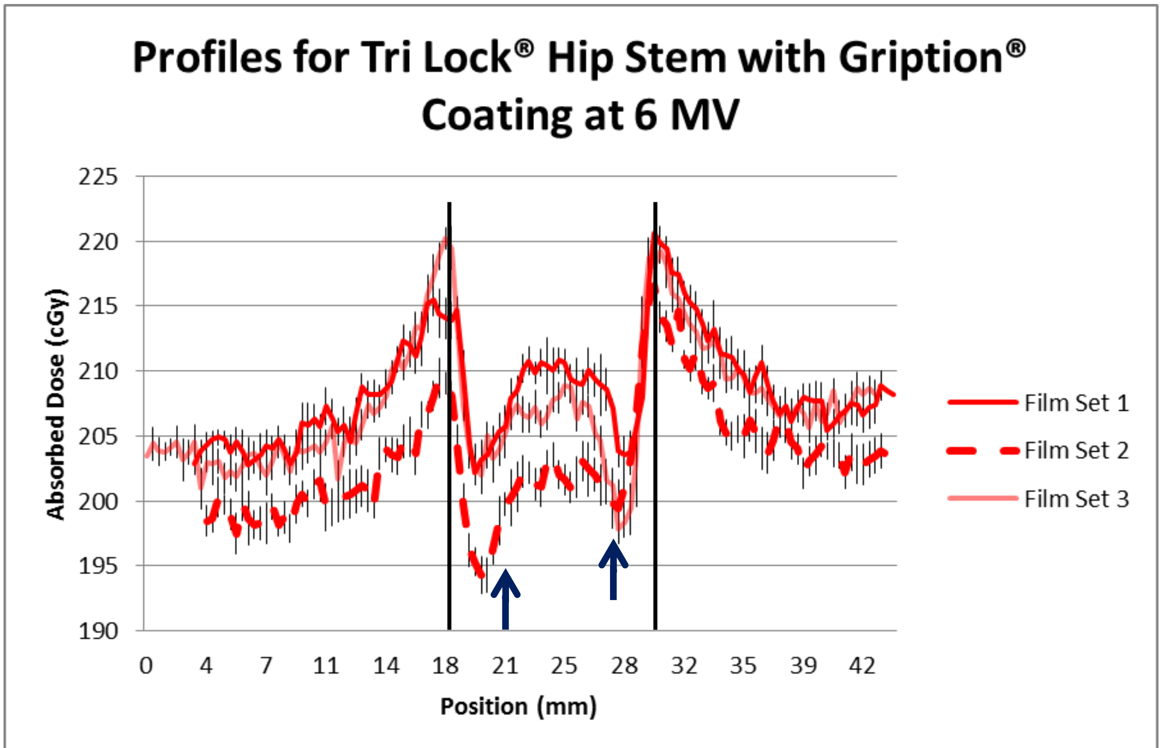

Figure 63: Profiles for the Tri Lock® hip stem with Gription® coating with 6 MV

The overall trends in the profile shape were consistent with predictions. The absorbed dose increased as it approached the left and right surface interface of hip stems, peaking at the interfaces. After crossing the surface interface boundaries, the absorbed dose immediately dropped. The absorbed dose increased after the immediate drop moving towards the center of the hip stems. The magnitude of the increase varied depending on the energy used and the type of hip stem in place. The magnitude of the absorbed dose at the right surface interface of the AML® hip stem was greater than the magnitude of the absorbed dose at the left surface interface.

It was also observed that there was some variation in the absolute dose from each film set. This was most likely due to a slight human setup error. Since the shape of the profiles matched well for the three film sets, the absolute dose values were normalized for further evaluation.

The pixel range width of 10 was compared to the pixel range width of 70. This was performed to evaluate if widening the range would decrease the noise present in the profiles. The following two plots compare the normalized profiles using a pixel range width of 10 and 70.

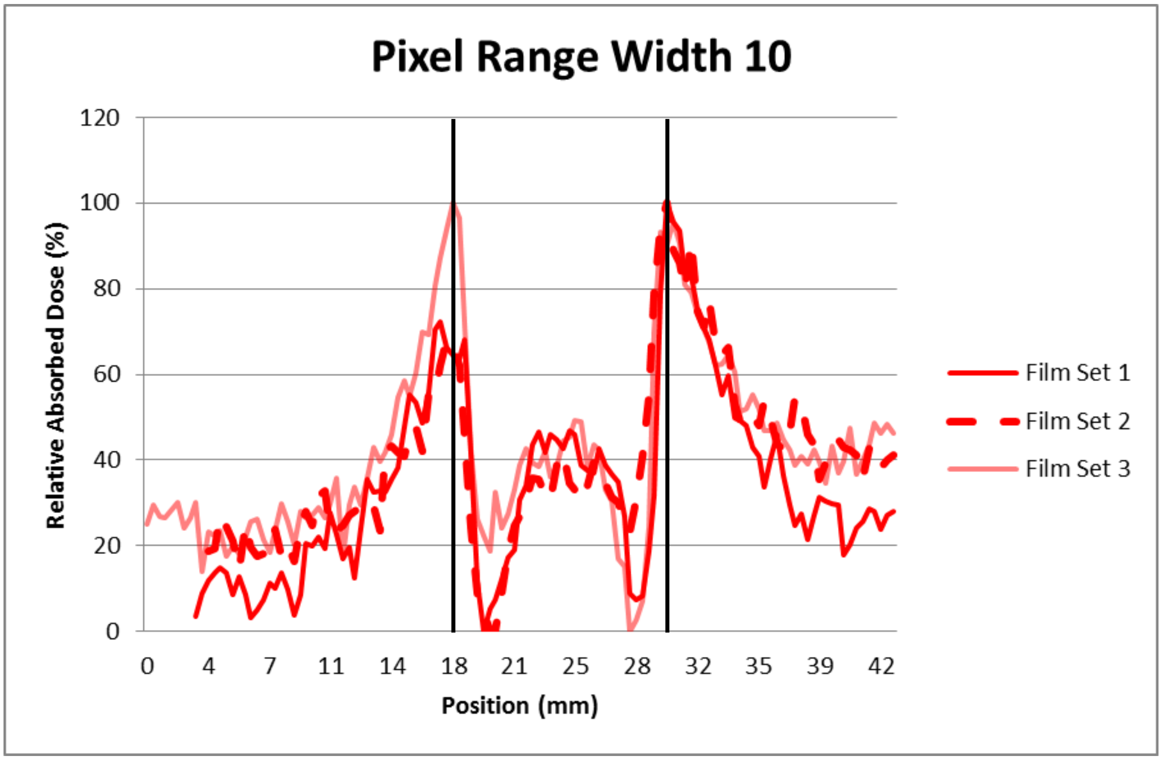

Figure 64: Normalized profiles for the Tri Lock® hip stem using 6 MV using a pixel range width of 10

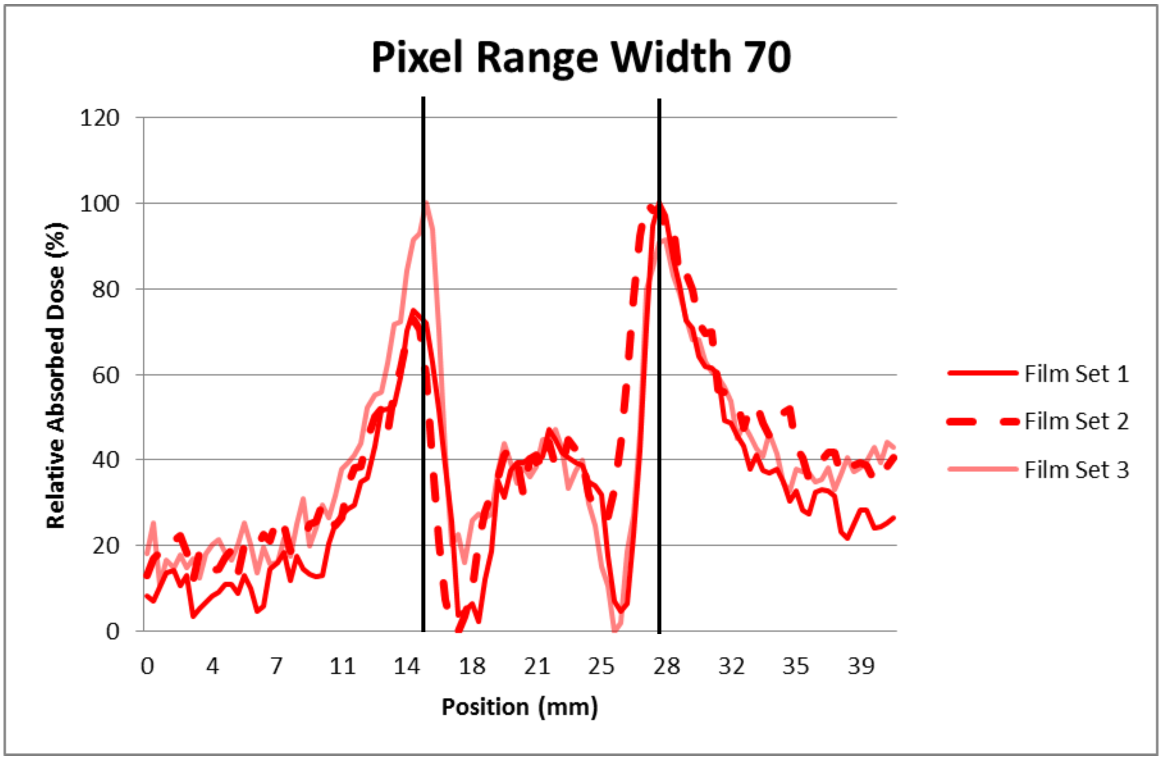

Figure 65: Normalized profiles for the Tri Lock® hip stem using 6 MV using a pixel range width of 70

The following figure presents the average of the three film sets with the pixel range width of 10 and the average of the three film sets with the pixel range width of 70.

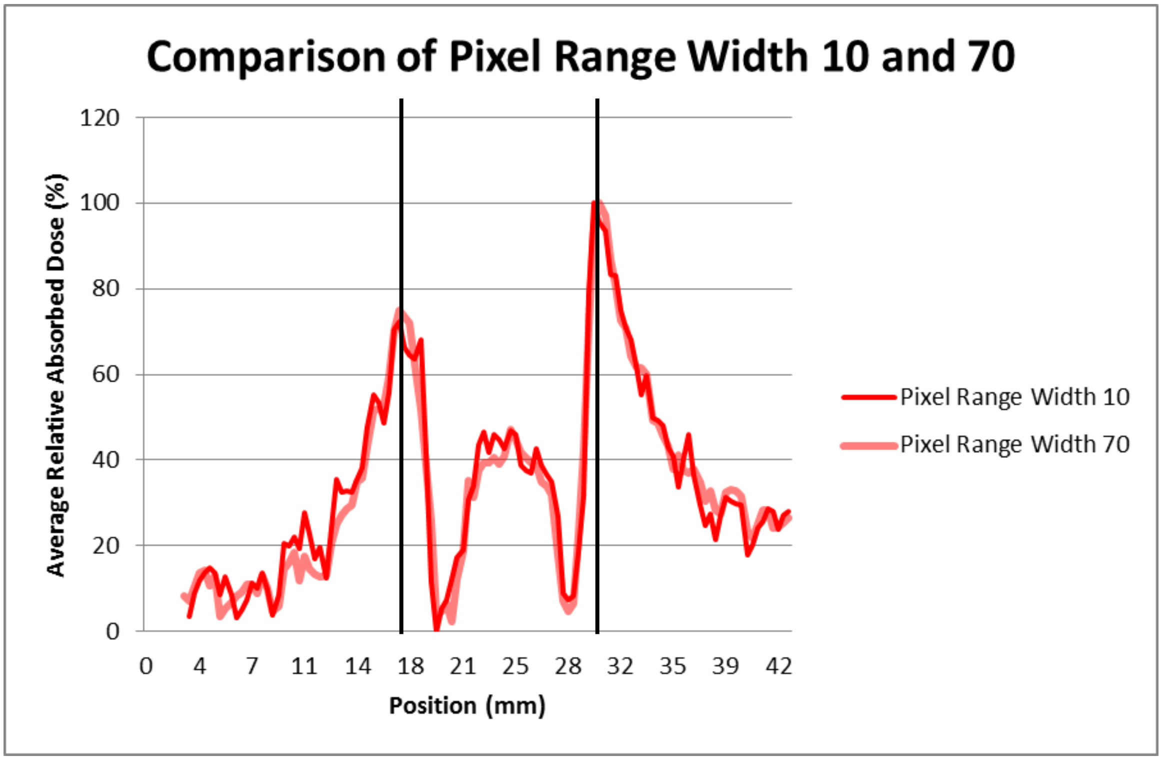

Figure 66: Comparison of the Pixel Range Width 10 and Pixel Range Width 70

The two different pixel range widths were compared by finding the average difference in the relative doses for the normalized profiles (the difference between pixel range width 10 and 70). The average difference was found to be 2.97. This indicates that there was very little reduction in the variation when increasing the pixel range width. With little reduction in the noise by increasing the pixel range width, the complete evaluation of the normalized profiles was completed using the pixel range width of 10 as advised by Ashland. Increasing the pixel range width without a considerable decrease in the noise dose bring up the possibility that the variance in the profiles may be due to the structure, chaotic or otherwise, and not noise alone. Further investigation fell outside the scope of this study.

4.3.2. Normalized Profiles

Since the raw profile data showed that some variation in the absolute dose between film sets were present, the raw profile data was normalized for further evaluation of the profiles. The profiles were normalized to the maximum dose value gathered from the three film sets. The resulting relative doses are relative to the maximum raw dose as a percent. The following figures represent the normalized profiles from each of the three set of film for each rod size, energy, and gantry position. These figures help to determine the reproducibility of the film measurements and the location of the interface point for each film set. The vertical black lines represent the position of the rod interface in relation to the profile.

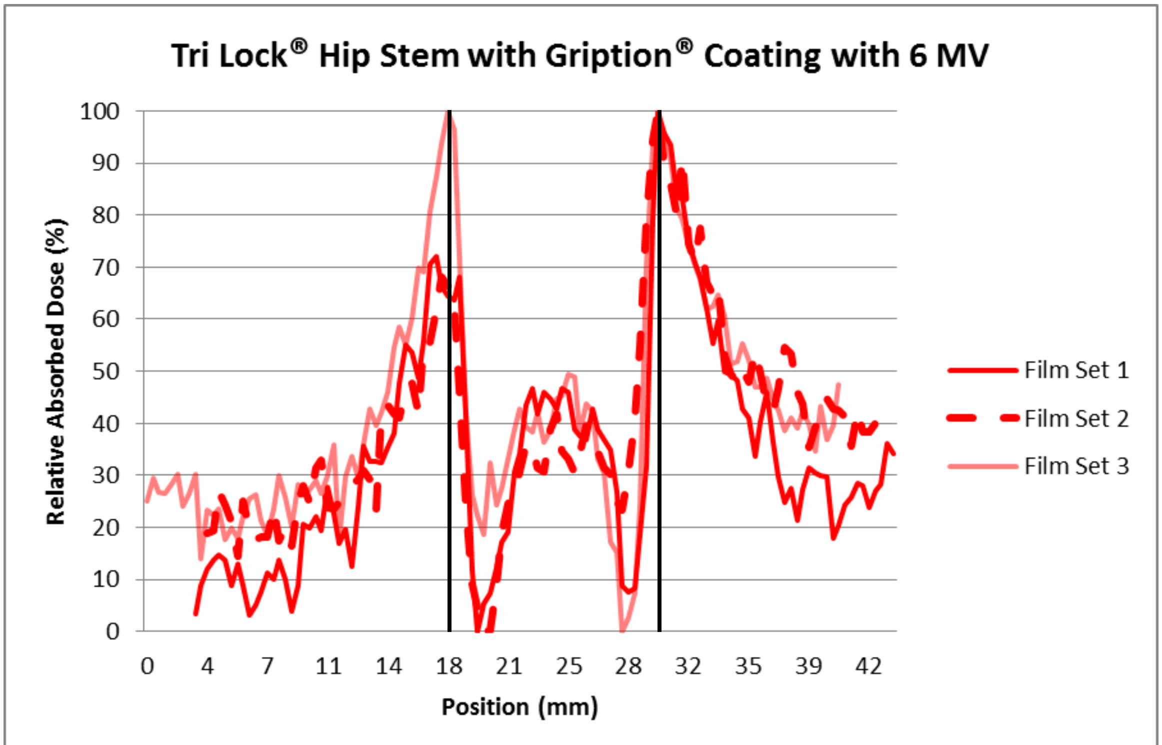

Figure 67: Normalized profiles for the Tri Lock® hip stem with Gription® coating using 6 MV

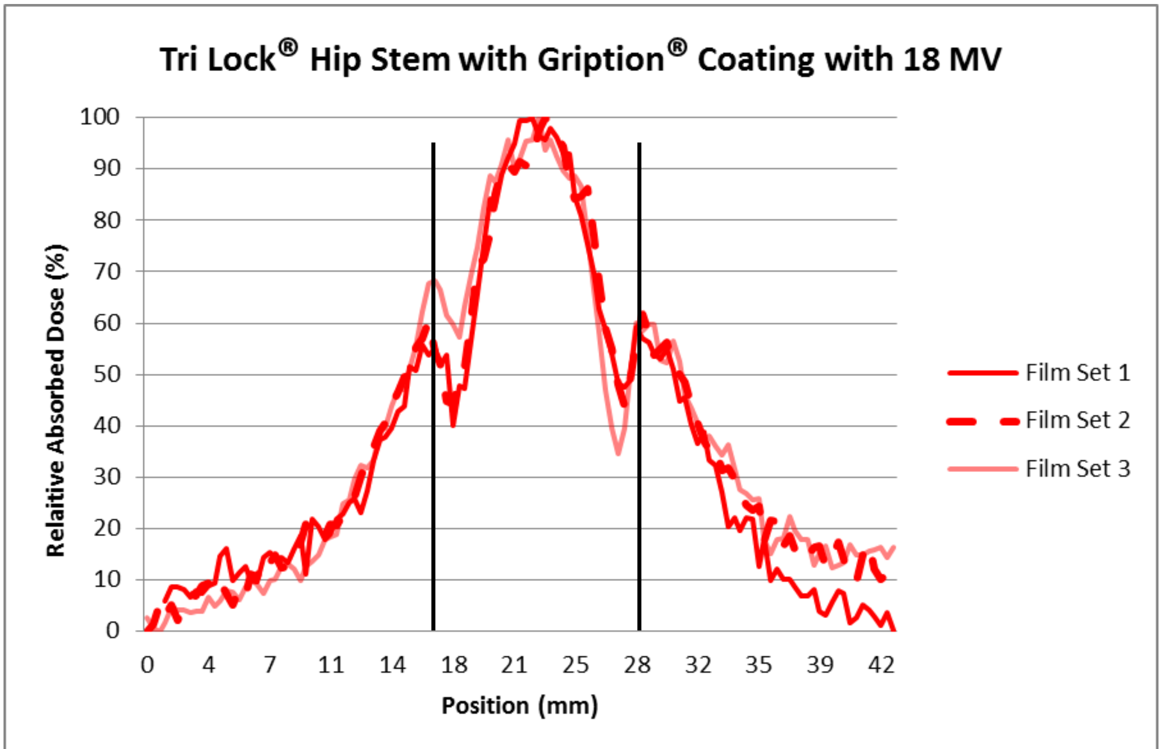

Figure 68: Normalized profiles for the Tri Lock® hip stem with Gription® coating using 18 MV

Similar profile trends as the stainless steel and titanium profiles trends were gathered with slight variations. The absorbed dose increased approaching the left and right surface interfaces. This increase is due to the increased scattering of electrons in the metal. After crossing the surface interface boundaries, there was a local decrease in dose before a re-build up region. The electrons that are laterally scattered also caused the local decrease since they were scattered instead of being deposited after crossing the surface interface. The slope of the local decrease in dose was less steep than the stainless steel and titanium rods for both the 6 and 18 MV photon beams. The Gription® coating was of a non-uniform shape and density resulting in tiny air pockets to be filled with water during the film measurements (see Figures 12 and 13). The non-uniformity of the shape and density of the coating resulted in electrons to be laterally scattered at positions further into the coating of the hip stem past the surface interface than with the stainless steel and titanium rods. With electrons being laterally scattered at positions further into the coating of the hip stem, the local decrease occurred over a wider length into the hip stem before reaching the re-buildup region.

A dose plateau was observed similar to the ½" titanium rod profiles in the Tri Lock® hip stem. The greater penetrative ability of the 18 MV photon beam resulted in a greater dose deposition at the center of the Tri Lock® hip stem at 18 MV compared to 6 MV.

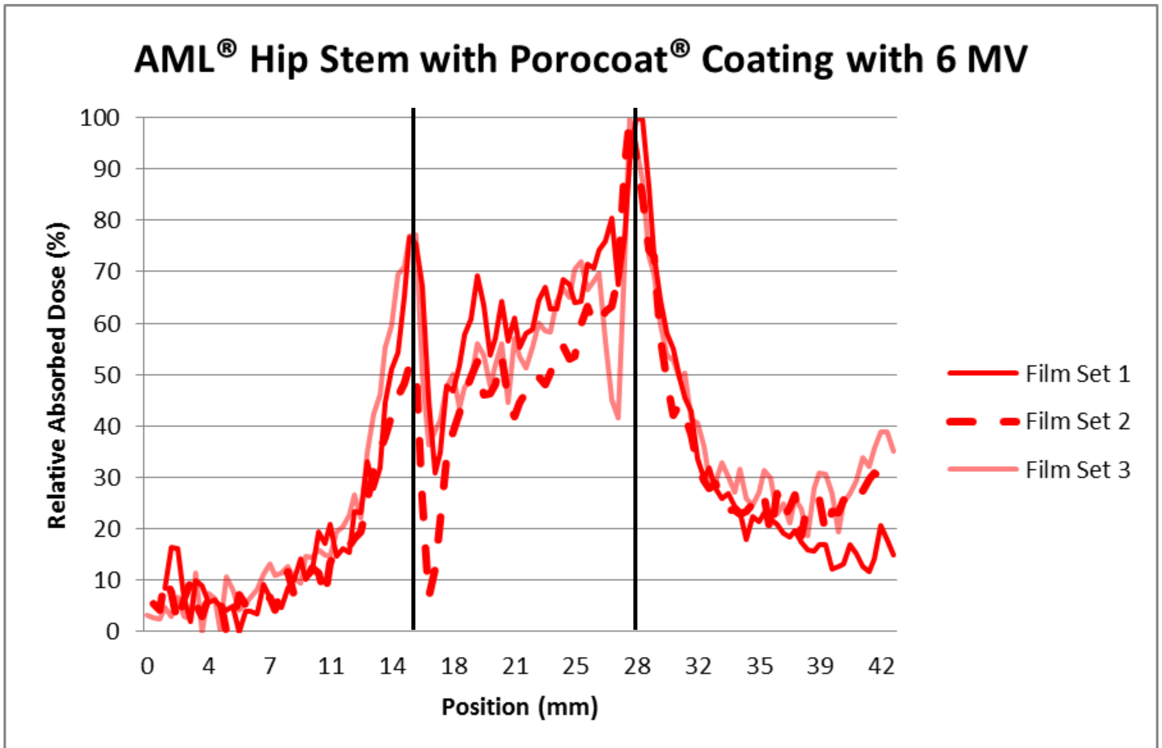

Figure 69: Normalized profiles for the AML® hip stem with Porocoat® coating using 6 MV

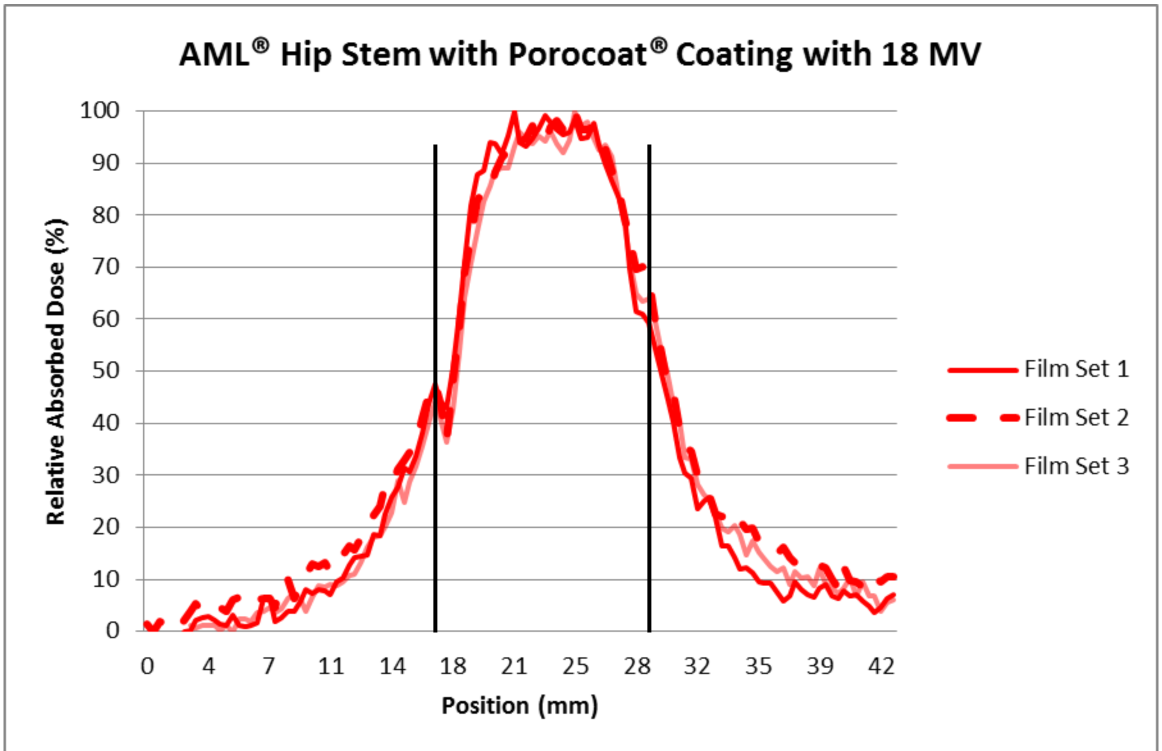

Figure 70: Normalized profiles for the AML® hip stem with Porocoat® coating using 18 MV

The AML® hip stem profiles responded in a manner that was expected with one exception. The dose at the left surface interface was less than the dose at the right surface interface for both 6 and 18 MV photon beams. This trend was found with all three film sets suggesting this trend was not human setup error. This was potentially caused by a non-uniform thickness of the Porocoat® coating performed by the manufacturer. The thickness of the Porocoat® coating was different at the left interface compared to the right interface. The right interface of the AML® hip stem resembled the profiles of the stainless steel and titanium rods without any porous coating. This indicates that the thickness of the coating on the right surface interface of the AML® hip stem is thinner than the left surface interface. Since it is thinner, the right surface interface responds in a similar manner as the rods without any coatings.

Comparing the AML® to the Tri lock®, the slope of the local decrease was slightly steeper for the AML®. This is attributed to the higher density of the material used in the AML®. This also may be slightly due to the Porocoat® coating thickness being smaller than the thickness of the Gription® coating. The non-uniformity of the shape and density of the Porocoat® coating resulted in electrons to be laterally scattered at positions further into the coating of the hip stem past the surface interface than the stainless steel and titanium rods. The electrons laterally scattered in the AML® hip stem were not scattered at positions as far into the coating of the hip stem as with the Tri Lock® hip stem due to the increased density of the AML® hip stem resulting in the less steep slope.

Overall, the magnitude of the increased dose at the center of the hip stems were larger for the 18 MV photon beam compared to the 6 MV photon beam. These findings were due to the greater forward penetration of the 18 MV beam compared to the 6 MV beam. More dose was absorbed at the center of the hip stems using an 18 MV photon beam, and more dose was absorbed at or near the surfaces of the hip stems using a 6 MV photon beam.

The following tables present the depth of the maximum point of the local decrease into the Tri Lock® and AML® hip stems:

Table 13: Depth of local decrease before re-buildup region in the Tri Lock® hip stem

Hip Stem	Energy	Average Depth of Local Decrease (mm)
Tri Lock®	6	1.42
Tri Lock®	18	1.42

Table 14: Depth of local decrease before re-buildup region in the AML® hip stem

Hip Stem	Energy	Depth of Local Decrease Left (mm)	Depth of Local Decrease Right (mm)
AML®	6	1.06	0.71
AML®	18	1.06	0.71

The depth of the local decrease remained the same for both energies. This means that the coating has the same lateral effect into the rods for both energies. The Tri Lock® hip stem resulted in greater local decrease depth due to its smaller density compared to the AML® hip stem. Comparing the left and right interfaces of the AML® hip stem, it can be seen that the right side had a less depth of local decrease than the left. This is again attributed to the coating being thinner on the right side than the left as discussed earlier. The right side acts more like the rods in the depth of the local decrease because there may be much less coating on the right side. The porous coating on the left side of the AML® and the Tri Lock® hip stem resulted in a greater depth of the local decrease into the hip stems compared to the stainless steel and titanium rods.

The dose profiles from the hip stems were slightly different shape than the stainless steel and titanium dose profiles because of the porous coatings and the difference in the densities of the two prostheses. The porous coating altered the interface effects slightly. This means it is necessary to include the porous coating in Monte Carlo modeling if accurate dose distributions are to be calculated.

4.3.3. Interface Dose Measurements for Tri Lock® and AML® Hip Stems

The following table presents the average relative interface dose measurements for the Tri Lock® and AML® hip stems found using the EBT3 film. The measurements were found by evaluating the normalized profile data for each film set for each hip stem to determine the interface locations (left and right). After determining the location of the interface along the profile, the average relative interface dose was calculated from the three film sets. This provided the average relative interface dose for each hip stem. The smaller interface position value represents the left surface interface of the rods and the larger interface position value represents the right surface interface of the rods.

Table 15: Average relative interface dose for the Tri Lock® and AML® hip stems

Hip Stem Type	Energy	Position along Profile (mm)	Average Relative Interface Dose (%)
Tri Lock®	6	17.99	96.19
Tri Lock®	6	28.93	96.79
Tri Lock®	18	15.87	58.39
Tri Lock®	18	28.22	58.57
AML®	6	15.52	68.01
AML®	6	27.87	97.15
AML®	18	16.58	46.43
AML®	18	28.93	63.69

There were larger relative doses at the surface interfaces for the 6 MV photon beam than the 18 MV photon beam for both the Tri Lock® and AML® hip stems. This is attributed to the greater penetrability of the 18 MV beam than the 6 MV beam. The Tri Lock® and AML® surface interfaces impeded the 6 MV beam more than the 18 MV beam resulting in a greater dose deposition from the 6 MV beam. The differences between the relative interface doses at 6 MV and 18 MV were not as large of differences observed with the stainless steel and titanium rods. This can be attributed to the added effects of the coating used on the hip stems.

The relative surface interface doses were comparable between the Tri Lock® hip stem and the AML® hip stem instead of seeing a larger relative surface interface doses with the larger density hip stem, the AML®. The only exception is at the right interface of the AML® hip stem. As discussed in the normalized profile section, the increased relative surface interface dose at the right interface can be attributed to a non-uniform coating thickness. The coating on the right interface was most likely less thick than the left side. With a thinner coating on the right side, the increased relative surface interface dose follows the same trend as the rods. Looking at all the other hip stem surface interfaces, their trend is different than observed with the stainless steel and titanium rods. Since the only main difference between the rod and hip stem is the added coating, this trend difference can be attributed to the addition of the coating. The non-uniform shape and density of the coatings resulted in non-uniform electron densities of the coating. The relative surface interface doses provided evidence that the relative electron densities of the coatings were less than the relative electron densities of the solid hip stem materials.

4.4. Comparison of Titanium Rods to Tri Lock® Hip Stem

The titanium rods were compared to the Tri Lock® hip stem due to their similar densities. The following figures present the comparison of the average relative dose profiles of the titanium rods and the Tri Lock® hip stem composed of a titanium alloy. The relative dose for this comparison is relative to the maximum dose value in the comparison (the maximum dose value from either the titanium rods or the Tri Lock® hip stem). The left surface interface profiles were aligned for evaluations.

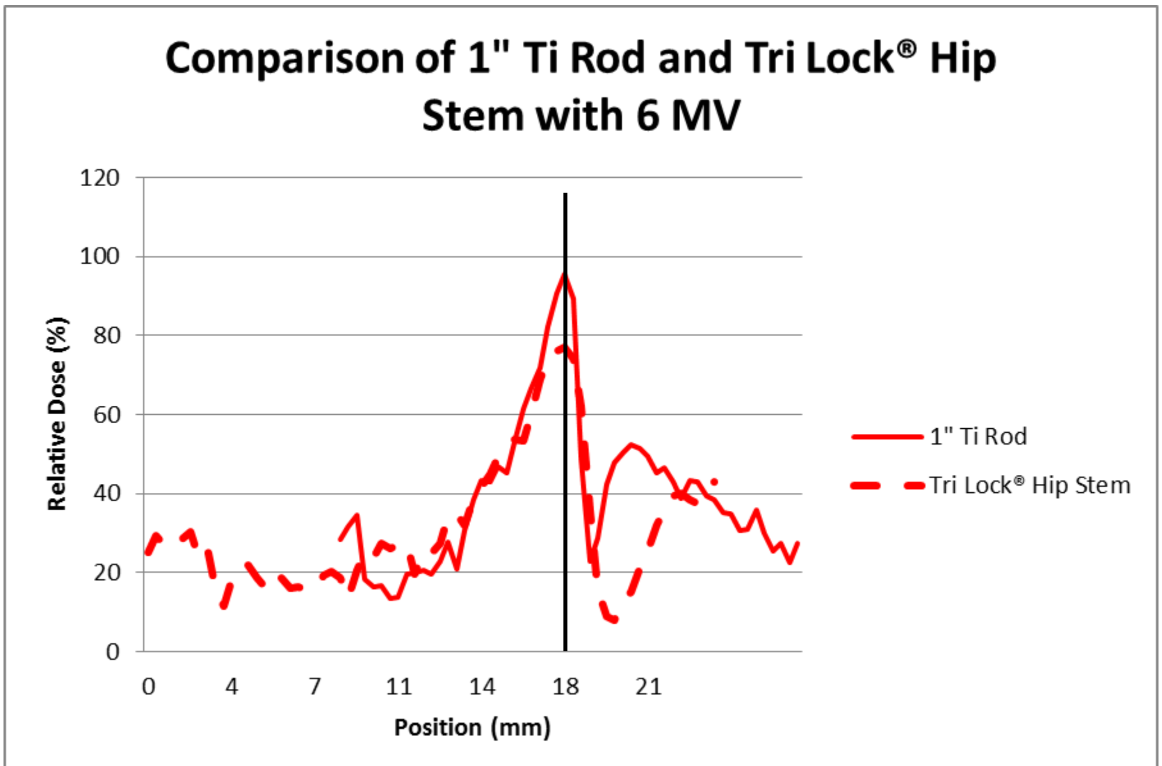

Figure 71: Comparison of the average normalized profiles from the 1" Ti rod and the Tri Lock® hip stem using 6 MV

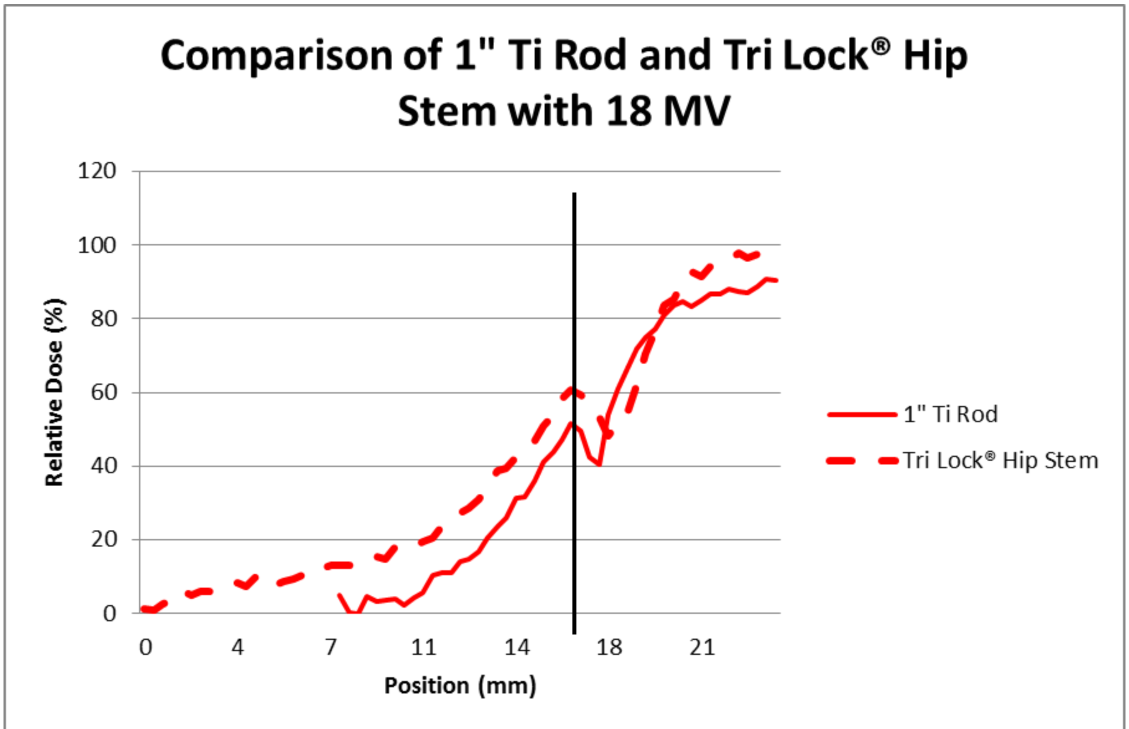

Figure 72: Comparison of the average normalized profiles from the 1" Ti rod and the Tri Lock® hip stem using 18 MV

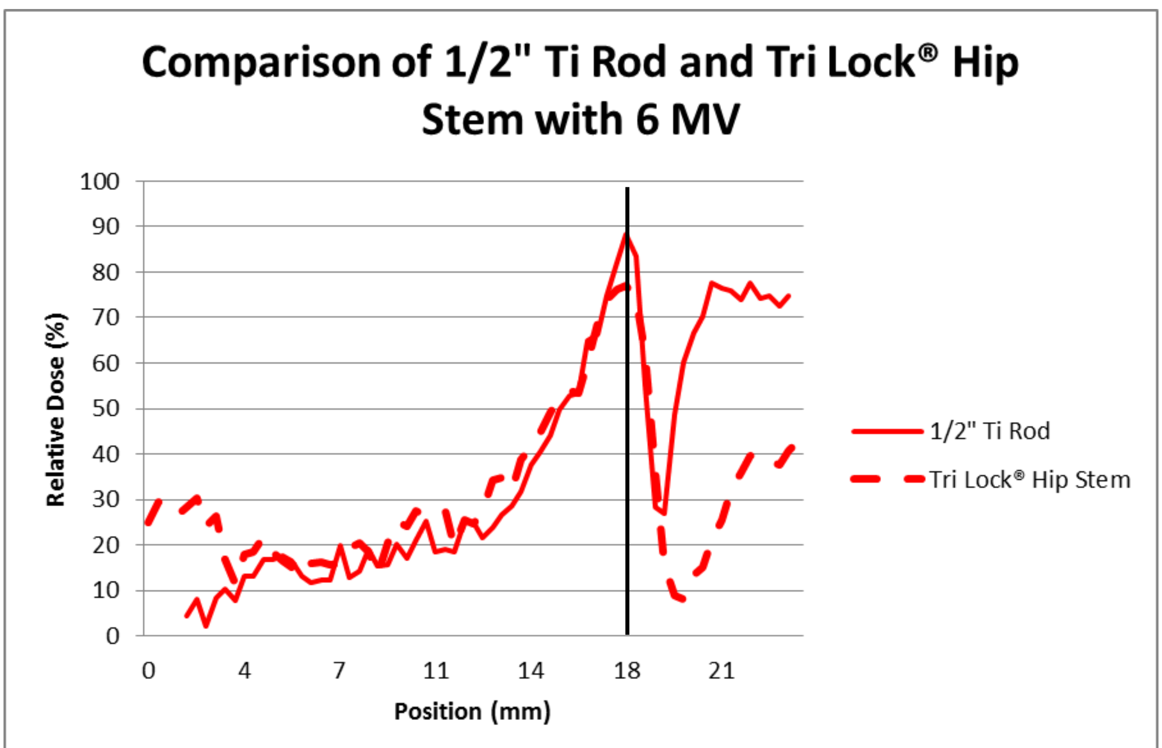

Figure 73: Comparison of the average normalized profiles from the 1/2" Ti rod and the Tri Lock® hip stem using 6 MV

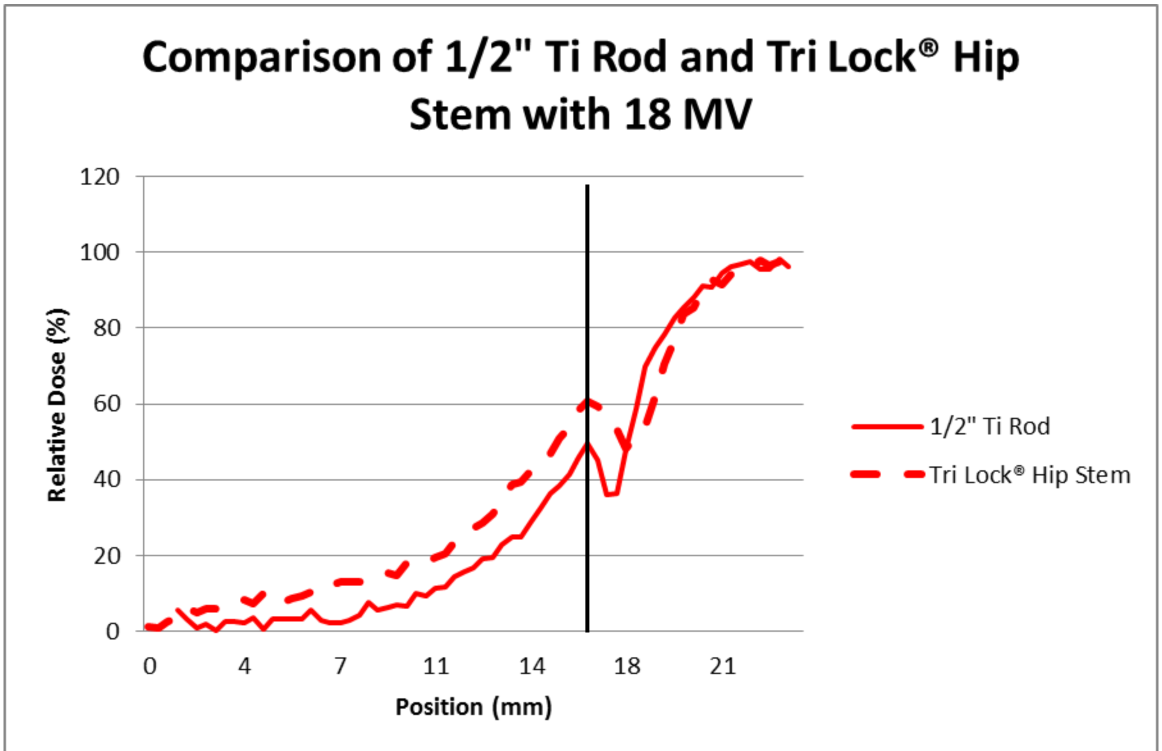

Figure 74: Comparison of the average normalized profiles from the 1/2" Ti rod and the Tri Lock® hip stem using 18 MV

The following table presents the average left surface interface absorbed dose for the 1" and ½" titanium rods and the Tri Lock® hip stem for 6 and 18 MV.

Table 16: Average left surface interface relative dose for the titanium rods and Tri Lock® hip stem

Rod/Hip Stem Type	Energy	Average Relative Dose (%)
Tri Lock®	6	76.98
1" Ti	6	95.50
1/2" Ti	6	88.22
Tri Lock®	18	60.59
1" Ti	18	51.67
1/2" Ti	18	49.40

The following figure presents the relative left interface dose values for 6 and 18 MV.

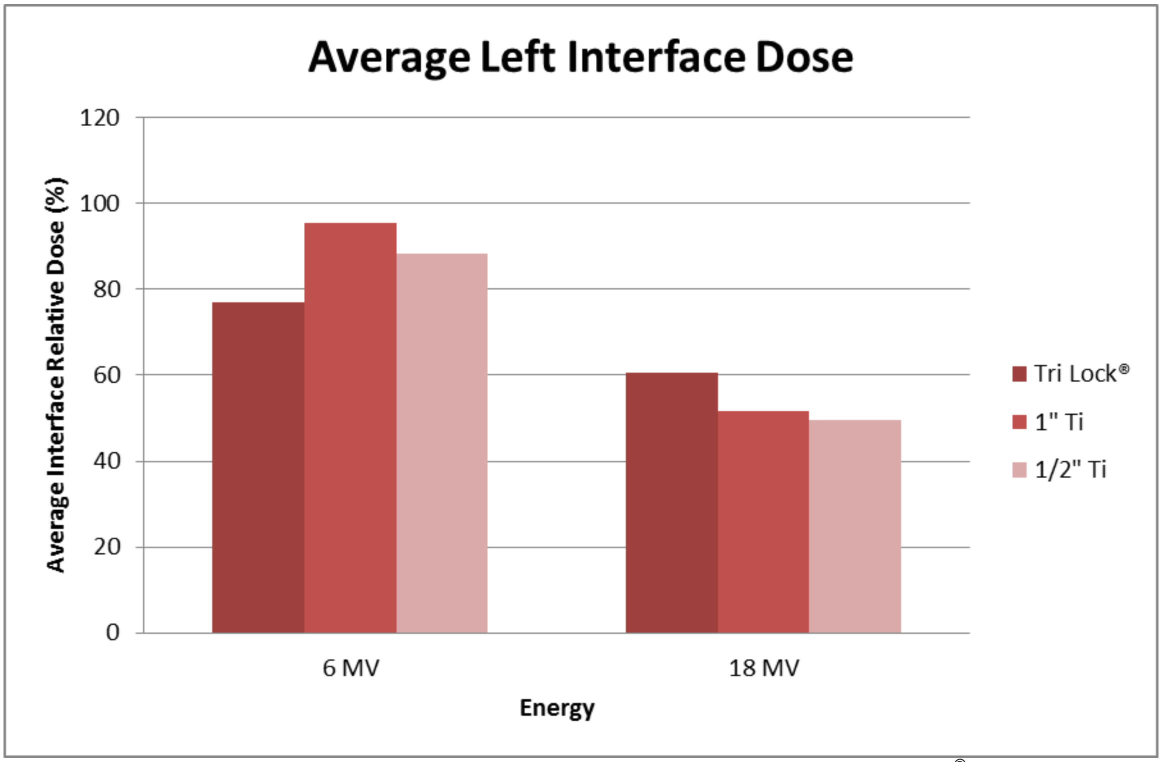

Figure 75: The average relative left surface interface doses for the Ti rods and the Tri Lock® hip stem using 6 and 18 MV

The Tri Lock® hip stem resulted in a smaller relative left interface dose compared to the 1" and ½" titanium rods using the 6 MV photon beam while all three had fairly similar relative left interface doses using the 18 MV beam. The smaller relative dose at surface interface of the Tri Lock® hip stem can be attributed to the effects of the coating. The added coating on the Tri Lock® hip stem reduced the relative surface interface dose compared to the titanium rods without the coating using the 6 MV beam. All three had fairly similar relative surface interface doses with the 18 MV beam due to the greater penetrability of the 18 MV beam. The coating had little to no effect on the 18 MV photon beam dose deposition at the surface interface.

Comparing the shape of the profiles show that the Tri Lock® hip stem results in a wider buildup region leading up to the surface interface and a wider local decrease in dose after crossing the interface. This is better observed in the comparison of the profiles using the 18 MV beam than the 6 MV beam. The wider buildup of dose leading up to the surface interface can be attributed to the laterally scattered electrons having a longer range with the 18 MV photon beam than the 6 MV photon beam.

4.5.Decrease in Dose 2 mm from the Interface

The following tables present the decrease in relative dose 2 mm from the surface interface of the rods and hip stems.

Table 17: Decrease in Absorbed Dose 2 mm from Surface Interface of Rods

Rod Type	Alloy Type	Energy	Dose Decrease 2 mm from Left Interface (%)	Dose Decrease 2 mm from Right Interface (%)
1" SS	SS 316 LVM	6	20.00	23.28
1" SS	SS 316 LVM	18	40.35	23.70
1/2" SS	SS 316 LVM	6	45.68	24.73
1/2" SS	SS 316 LVM	18	33.86	28.17
1" Ti	Unalloyed Commercially Pure Titanium	6	50.20	45.07
1" Ti	Unalloyed Commercially Pure Titanium	18	39.69	26.30
1/2" Ti	Unalloyed Commercially Pure Titanium	6	39.48	27.85
1/2" Ti	Unalloyed Commercially Pure Titanium	18	34.70	29.08

Table 18: Decrease in Absorbed Dose 2 mm from Surface Interface of Hip Stems

Stem Type	Coating Type	Alloy Type	Energy	Dose Decrease 2 mm from Left Interface (%)	Dose Decrease 2 mm from Right Interface (%)
Tri Lock®	Gription®	Ti-6Al-4V ELI	6	27.85	15.68
Tri Lock®	Gription®	Ti-6Al-4V ELI	18	32.64	12.63
AML®	Porocoat®	CoCrMo	6	44.42	44.96
AML®	Porocoat®	CoCrMo	18	37.03	48.28

Consistent with the finding presented in *Ding et al.*, a larger percentage of the relative dose occurred within 2 mm of the surface interfaces. This can be attributed to the range of the laterally scattered electrons. The buildup of dose approaching the surface interface begins with the greatest range of the laterally scattered electrons. This means that outside the range of the laterally scattered electrons, the dose distribution should remain consistent with the dose distribution without the high-Z materials. The relative dose decreased 20.00% - 50.20% within 2 mm of the stainless steel and titanium surface interfaces. The relative dose decreased 12.63% - 44.96% within 2 mm of the Tri Lock® and AML® hip stems. The slightly smaller decreased relative dose percentage within 2 mm of the interface for the hip stems can be attributed to the coatings used on these hip stems.

5. Conclusion

The dose buildup approaching to the surface interface of the rods and hip stems is attributed to the laterally scattered electrons from the high-Z of the rods and hip stems. The immediate local decrease in dose after crossing the surface interface is also attributed to the laterally scattered electrons. The local decrease in dose is then followed by a re-buildup region with varying central rod or hip stem dose depositions based on the density and size of the material and the energy of the incident photon beam. The width of the local decrease was wider for the hip stems compared to the rods due to the added coating. The non-uniformity of the shape and density of the coatings resulted in electrons to be laterally scattered at positions further into the coatings of the hip stems past the surface interface than with the stainless steel and titanium rods.

The smaller relative doses at the surface interfaces of the rods and hip stems with the 18 MV photon beam was attributed to the greater penetrability of the beam compared to the 6 MV beam. With larger mass densities, and therefore larger relative electron densities, the stainless steel rods resulted in larger relative dose at the surface interfaces. The coating of the hip stems resulted in comparable relative surface interface doses with the exception of the right surface interface of the AML® hip stem. The larger diameter rods with greater surface area at the interfaces resulted in larger relative doses compared to the smaller diameter rods. When comparing the titanium rods and the Tri Lock® hip stem, the coating reduces the relative surface interface dose when using a 6 MV photon beam but has little effect on the magnitude of the relative surface interface dose when using a 18 MV photon beam.

Comparison of the film measurements to Pinnacle^3 verified the capabilities and limitations of the Pinnacle^3 dose calculation algorithm. Pinnacle^3 was able to accurately calculate the dose far from the high-Z stainless steel and titanium rods, but it was inaccurate in its calculation of the dose at the interface of the high-Z stainless steel and titanium rods.

A larger percentage of the relative dose occurred within 2 mm of the surface interfaces for both the rods and the hip stems attributed to the range of the laterally scattered electrons. Once past the range of the scattered electrons, the dose should remain consistent with the dose found without the presence of a high-Z material. The hip stems had slightly smaller relative dose increase within 2 mm than the rods due to the coating.

The trends gathered in this study for the stainless steel and titanium rods were consistent with trends presented in previous studies, such as *Ding and Yu* and TG-63, and reinforced the need for continued research into the effects of porous coatings used with prostheses (Ding and Yu 2001, Reft, Alecu et al. 2003). The dose distribution perturbations were increased with increasing density of the material used. The results of this study are unique in gathering the dose right at the interface and under the surface of prostheses.

The 85° profiles provided evidence that Gafchromic™ EBT3 film would be applicable in future studies regarding the attenuation of dose through high-Z materials similar to previous studies performed by *Ding et al, Keall, Laub and Nüsslin,* and *Eng* (Ding and Yu 2001, Keall, Chock et al. 2003, Laub and Nusslin 2003, Eng 2000,). Utilizing EBT3 film in determining the attenuation would allow for a more detailed evaluation of the effects of porous coatings on prostheses that have previously been difficult to address.

Future work in this field of study includes feasibility studies into the modeling of the porous coating of hip prostheses in Monte Carlo. If it is determined to be feasible, the Monte Carlo dose calculations could be compared to film measurements and dose values calculated using convolution-superposition methods to further evaluate and potentially develop better solutions to the deficiencies. Convolution-superposition methods are limited in the ability to accurately model the coupled photon-electron transport across the interface.

Another area of future work includes evaluating and quantifying the biological effects of high-Z materials in the body during radiation therapy. This study provided an initial data set with porous coating data. With the ability to gather data including the effects of porous coatings available, it will be possible for radiobiologists to delve deeper into the biological effects. With the growing incidence of patients with hip prostheses, it will be necessary to continue research efforts to fully quantify and understand the effects these high-Z materials have on radiation therapy planning and radiobiology. Developments in the understanding of these effects will lead to higher quality and potentially adaptive radiation therapy treatment plans for patients with high-Z prostheses.

6. Bibliography

Center for Disease Control and Prevention (CDC), C. f. D. C. a. P. (2010). National Hospital Discharge Survey: 2010 Table,
Procedures by Selected Patient Characteristics - Number by Procedure Category and Age.

AAOS. (2014). "Total Hip Replacement - Ortho Info." from http://orthoinfo.aaos.org/topic.cfm?topic=A00377.

Apipanyasopon, L. (2012). Fundamental to Advanced Radiotherapy Treatment Techniques: Dose Calculation Algorithms. 10th SEACOMP and 12th AOCMP, Thailand.

Ashland. (2014). "FilmQA™ Pro User Guide." Covington, KY. www.filmqapro.com.

Attix, Frank H. *Introduction to Radiological Physics and Radiation Dosimetry: Frank Herbert Attix*. Weinheim: Wiley-VCH, 2004. Print.

Baird, E. O. and Q. K. Kang (2009). "Prophylaxis of heterotopic ossification – an updated review." Journal of Orthopaedic Surgery and Research 4(12).

Balboni, T. A., P. Gaccione, R. Gobezie and H. J. Mamon (2007). "Shielding of the hip prosthesis during radiation therapy for heterotopic ossification is associated with increased failure of prophylaxis." Int J Radiat Oncol Biol Phys 67(5): 1499-1505.

Balboni, T. A., R. Gobezie and H. J. Mamon (2006). "Heterotopic ossification: Pathophysiology, clinical features, and the role of radiotherapy for prophylaxis." Int J Radiat Oncol Biol Phys 65(5): 1289-1299.

Borca, V. C., M. Pasquino, G. Russo, P. Grosso, D. Cante, P. Sciacero, G. Girelli, M. R. La Porta and S. Tofani (2013). "Dosimetric Characterization and Use of Gafchromic™ EBT3 Film for IMRT Dose Verification." Journal of Applied Clinical Medical Physics 14(2): 158 - 171.

Butson, M. J., P. K. Yu, T. Cheung and P. Metcalfe (2003). "Radiochromic Film for Medical Radiation Dosimetry." Materials Science and Engineering: R: Reports(41): 61 - 120.

Carolan, M. G. (2010). Pencil Beam Dose Calculation Algorithm. I. C. C. Centre.

Chao, S. T., S. Y. Lee, L. S. Borden, M. J. Joyce, V. E. Krebs and J. H. Suh (2006). "External beam radiation helps prevent heterotopic bone formation in patients with a history of heterotopic ossification." J Arthroplasty 21(5): 731-736.

Childs, H. A., 3rd, T. Cole, E. Falkenberg, J. T. Smith, J. E. Alonso, J. P. Stannard, S. A. Spencer, J. Fiveash, D. Raben, J. A. Bonner, A. O. Westfall and R. Y. Kim (2000). "A prospective evaluation of the timing of postoperative radiotherapy for preventing heterotopic ossification following traumatic acetabular fractures." Int J Radiat Oncol Biol Phys 47(5): 1347-1352.

Cooley, L. M. and R. J. Goss (1958). "The effects of transplantation and x-irradiation on the repair of fractured bones." Am J Anat 102(2): 167-181.

Coventry, M. B. and P. W. Scanlon (1981). "The use of radiation to discourage ectopic bone. A nine-year study in surgery about the hip." J Bone Joint Surg Am 63(2): 201-208.

Craven, P. L. and M. R. Urist (1971). "Osteogenesis by radioisotope labelled cell populations in implants of bone matrix under the influence of ionizing radiation." Clin Orthop Relat Res 76: 231-243.

DesRosiers, C. (2013). Calculation Algorithms in Radiation Therapy Treatment Planning Systems. AAMD Region III Annual Meeting, Indianapolis, IN.

Devic, S. (2011). "Radiochromic film dosimetry: past, present, and future." Phys Med 27(3): 122-134.

Ding, G. X. and C. W. Yu (2001). "A study on beams passing through hip prosthesis for pelvic radiation treatment." Int J Radiat Oncol Biol Phys 51(4): 1167-1175.

Eng, T. Y. (2000). "Dose attenuation through a titanium alloy hip prosthesis." Med Dosim 25(1): 7-8.

Fort Wayne Metals. (2011) “Medical Technical Binder.”

Gregoritch, S. J., M. Chadha, V. D. Pelligrini, P. Rubin and D. A. Kantorowitz (1994).

"Randomized trial comparing preoperative versus postoperative irradiation for prevention of heterotopic ossification following prosthetic total hip replacement: preliminary results." Int J Radiat Oncol Biol Phys 30(1): 55-62.

Healy, W. L., T. C. Lo, A. A. DeSimone, B. Rask and B. A. Pfeifer (1995). "Single-dose irradiation for the prevention of heterotopic ossification after total hip arthroplasty. A comparison of doses of five hundred and fifty and seven hundred centigray." J Bone Joint Surg Am 77(4): 590-595.

Holzwarth, U. and G. Cotogno (2012). Total Hip Arthroplasty: State of the Art, Challenges and Prospects. Luxembourg, Joint Research Centre of the European Commission.

Kantorowitz, D. A., G. J. Miller, J. A. Ferrara, G. S. Ibbott, R. Fisher and C. R. Ahrens (1990). "Preoperative versus postoperative irradiation in the prophylaxis of heterotopic bone formation in rats." Int J Radiat Oncol Biol Phys 19(6): 1431-1438.

Keall, P. J., J. V. Siebers, R. Jeraj and R. Mohan (2003). "Radiotherapy dose calculations in the presence of hip prostheses." Med Dosim 28(2): 107-112.

Khan, F. M. (2003). The Physics of Radiation Therapy. Philadelphia, Lippincott Willaims & Wilkins.

Knoll, G. F. (2000). Radiation Detection and Measurement. New York, Wiley.

Knoos, T. (2003). Review of treatment planning systems - photon planning in commercial systems. Lund University Hospital, Sweden.

Kolbl, O., D. Knelles, T. Barthel, U. Kraus, M. Flentje and J. Eulert (1997). "Randomized trial comparing early postoperative irradiation vs. the use of nonsteroidal anti inflammatory drugs for prevention of heterotopic ossification following prosthetic total hip replacement." Int J Radiat Oncol Biol Phys 39(5): 961-966.

Lange, J., V. G. Briggs, P. D. Franklin, D. C. Ayers and J. M. Drew (2014). Trends In Total Hip Arthroplasty in the United States: The Shift to a Younger Demographic, New Orleans, American Academy of Orthopaedic Surgeons (AAOS).

Laub, W. U. and F. Nusslin (2003). "Monte Carlo dose calculations in the treatment of a pelvis with implant and comparison with pencil-beam calculations." Med Dosim 28(4): 229-233.

Lewis, D. F. (2012). Making Film Dosimetry Easy: Introducing the 'One-scan' Protocol. AAPM, Charlotte.

Lewis, D. F., A. Micke and X. Yu (2012). New Performance Standard: Multi-channel and One-scan Radiochromic Film Dosimetry, Strasbourg.

Lo, T. C., W. L. Healy, D. J. Covall, W. E. Dotter, B. A. Pfeifer, W. R. Torgerson and S. A. Wasilewski (1988). "Heterotopic bone formation after hip surgery: prevention with single-dose postoperative hip irradiation." Radiology 168(3): 851-854.

Maradit-Kremers, H., C. S. Crowson, D. Larson, W. A. Jiranek and D. J. Berry (2014). "Prevalence of Total Hip (THA) and Total Knee (TKA) Arthroplasty in the United States."

Niroomand-Rad, A., C. R. Blackwell, B. M. Coursey, K. P. Gall, J. M. Galvin, W. L. McLaughlin, A. S. Meigooni, R. Nath, J. E. Rodgers and C. G. Soares (1998). "Radiochromic film dosimetry: recommendations of AAPM Radiation Therapy Committee Task Group 55. American Association of Physicists in Medicine." Med Phys 25(11): 2093-2115.

Orthopaedics, D. (2002). AML® Design Rationale. DePuy Orthopaedics. Warsaw, IN.

Orthopaedics, D. (2011). Tri Lock® Design Rationale. DePuy Orthopaedics. Warsaw, IN.

Papanikolaou, Nikos, Jerry J. Battista, Arthur L. Boyer, Constantin Kappas, Eric Klein, T. Rock Mackie, Michael Sharper, and Jake Van Dyk. *Tissue Inhomogeneity Corrections for Megavoltage Photon Beams*. Rep. no. 85. College Park: American Association of Physicists in Medicine, 2004. Web. <https://www.aapm.org/pubs/reports/RPT_85.pdf>.

Pellegrini, V. D., Jr., A. A. Konski, J. A. Gastel, P. Rubin and C. M. Evarts (1992).

"Prevention of heterotopic ossification with irradiation after total hip arthroplasty. Radiation therapy with a single dose of eight hundred centigray administered to a limited field." J Bone Joint Surg Am 74(2): 186-200.

Poppinga, D., A.A. Schoenfeld, K.J. Doerner, O. Blanck, D. Harder, and B. Poppe (2014). “A new correction method serving to eliminate the parabola effect of flatbed scanners used in radiochromic film dosimetry.” Med Phys 41(2).

Reft, C., R. Alecu, I. J. Das, B. J. Gerbi, P. Keall, E. Lief, B. J. Mijnheer, N. Papanikolaou, C. Sibata, J. Van Dyk and A. R. T. C. T. Group (2003). "Dosimetric considerations for patients with HIP prostheses undergoing pelvic irradiation. Report of the AAPM Radiation Therapy Committee Task Group 63." Med Phys 30(6): 1162-1182.

Seegenschmiedt, M. H., L. Keilholz, P. Martus, A. Goldmann, R. Wolfel, F. Henning and R. Sauer (1997). "Prevention of heterotopic ossification about the hip: final results of two randomized trials in 410 patients using either preoperative or postoperative radiation therapy." Int J Radiat Oncol Biol Phys 39(1): 161-171.

Seegenschmiedt, M. H., H. B. Makoski, O. Micke and D. German Cooperative Group on Radiotherapy for Benign (2001). "Radiation prophylaxis for heterotopic ossification about the hip joint--a multicenter study." Int J Radiat Oncol Biol Phys 51(3): 756-765.

Soares, C. G. Radiochromic Film. NIST.

Sylvester, J. E., P. Greenberg, M. T. Selch, B. J. Thomas and H. Amstutz (1988). "The use of postoperative irradiation for the prevention of heterotopic bone formation after total hip replacement." Int J Radiat Oncol Biol Phys 14(3): 471-476.

Washington, C. M. L., Dennis T. (2010). Principles and Practice of Radiation Therapy St. Louis, Mosby Elsevier.

APPENDIX

A. Delivery and Analysis of Pinnacle^3 Plan to EBT3 Film

1. In Pinnacle^3, create a plan with the 8 squares as shown in the following figure:

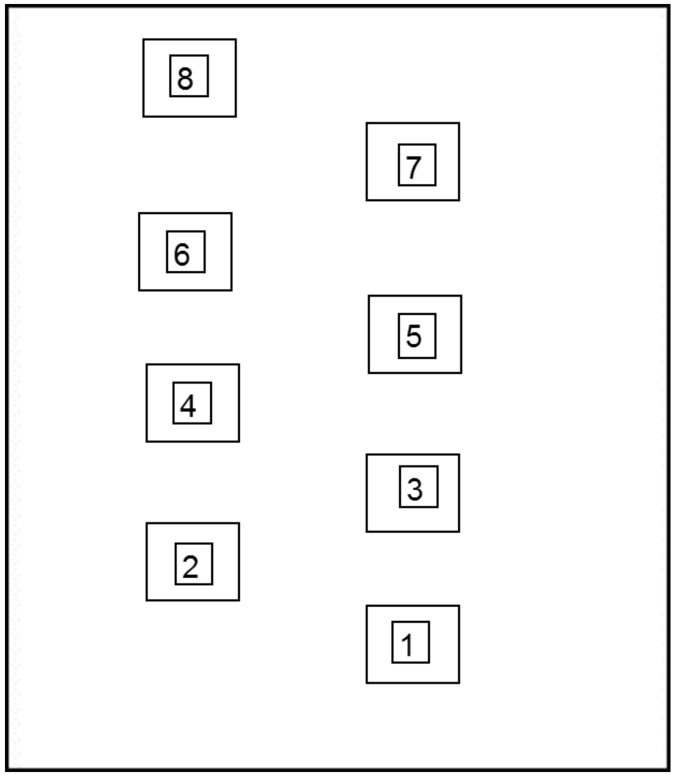

Figure 76: Pinnacle^3 8 Square Plan

2. Each square has dimensions of 2.9 X 2.9 cm^2.

3. Open the 8 square patient plan in Mosaic to deliver the plan.

4. With gloves on, place an entire sheet of Gafchromic™ EBT3 film on top of 10 cm of solid water so that the film in covering the entire treatment field as shown in the following figure:

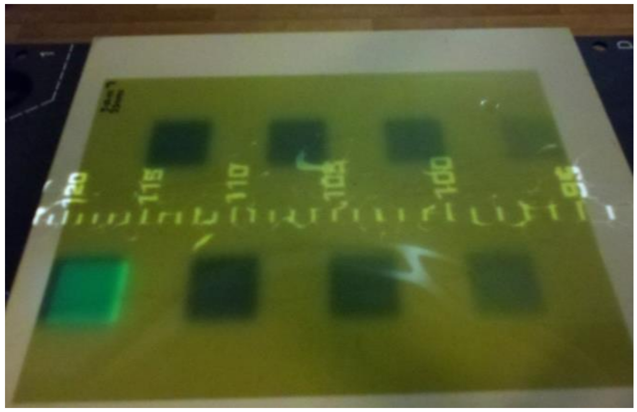

Figure 77: EBT3 Film Placement for Delivery of 8 Square Plan

5. Label the film orientation, the date, and time of exposure.

6. Place 5 cm of solid water on top of the film sandwiching the film.

7. Set the SSD to 100 cm.

8. Deliver the plan to the film.

9. Remove the film, and allow 24 hours to pass before scanning and analyzing the film.

10. When the necessary time has elapsed, turn on the Epson flatbed RGB scanner allowing a minimum of 30 minutes for warm-up.

11. Perform 7 warm-up scans to warm the lamps up.

12. When the scanner is warmed-up, ensure that the scanner configurations are correct with the color correction turned off. The scanner settings should be in professional mode, transparency, positive film, 48 bit color, 75 dpi, and landscape orientation.

13. Open the FilmQA™ Pro software and load the appropriate calibration file for this film batch.

14. Double click on the "Case object management" under "Case Data Selector," and select "Dose map from image (single scan)" from the "Add new case object" drop down list.

15. Place the film on the scanner according to the following figure:

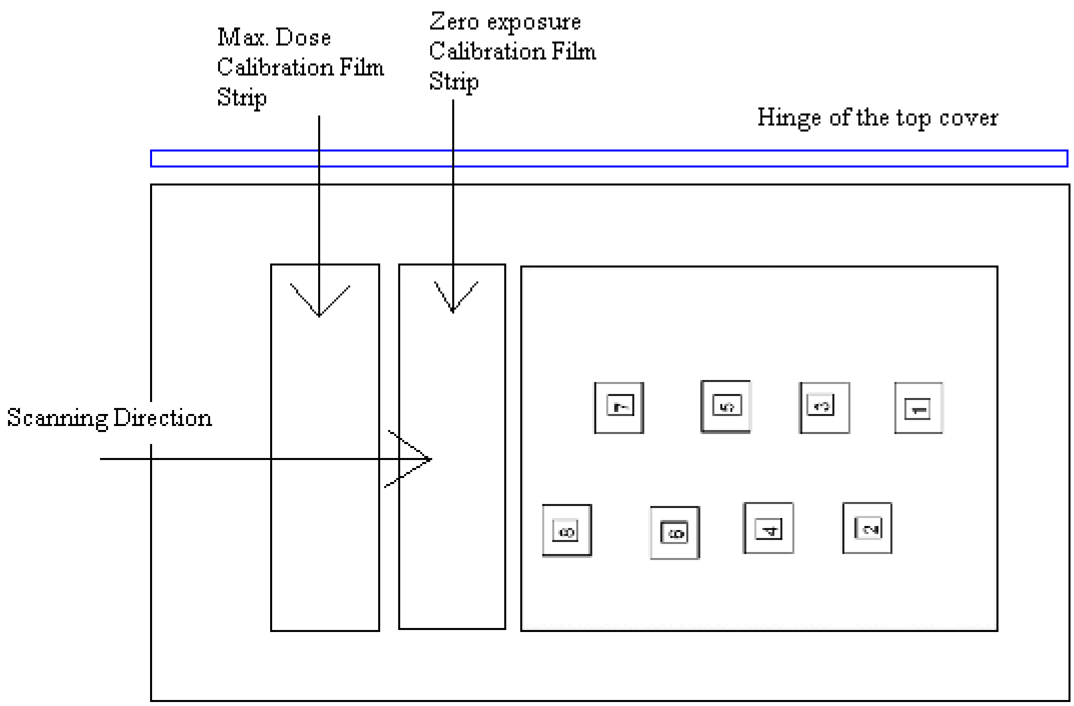

Figure 78: Film Placement and Orientation on the RGB Flatbed Scanner

16. Double click on "Dose map from image (single scan)" and then right click on "Data-Dose film (empty)". Select "Scan image 'Dose Film'".

17. On the Maximum dose calibration strip and zero exposure strip, create calibration regions and assign the corresponding dose to each region (305.2 cGy and 0 cGy).

18. Select the appropriate "Dose mapping method" by right clicking on the "Dose map from image (single scan)".

19. Right click on “Dose map from image (single scan)” and select “Rebuilt ‘Dose Map’” to create a dose map of the image.

20. Save the dose map by right clicking on “Data-dose film” and selecting “Save image as”.

21. Use the “Film Evaluation Panel” tools to evaluate the film.

22. Under the statistics tab, a dose square can be made for each of the 8 squares.

23. Under the profile tab, profiles can be made for each of the 8 squares.

24. When evaluating, look at the red and green channels since the blue channel is only helpful for film thickness/uniformity.

B. Ion Chamber Cross Calibration and Water Tank Measurements Procedure

1. Fill the water tank to the desired level and position the A14 ion chamber in the holder, lowering the ion chamber so it is bisected by the top surface of the water.

2. Set the SSD to 100 cm.

3. Record the water temperature and pressure.

4. Lower the ion chamber 0.6r (1.2 mm for the A14) and zero the crank tank.

5. Lower the ion chamber to 5 cm depth.

6. Connect the ion chamber to the tri-axial cable connected to an electrometer. Be sure to allow the electrometer 15-20 minutes of warm-up time.

7. Deliver 500 MU to the ion chamber to warm-up the beam and the ion chamber/electrometer.

8. Load the 8 square Pinnacle[3] plan to be delivered.

9. Position the ion chamber in the center of the first square.

10. Deliver the plan two times and record the readings (in nC).

11. Repeat steps 7 and 8 for all of the 8 squares.

12. In order to cross calibrate the A14 chamber with the A12 chamber, set the field to 10 x 10 cm^2 at 10 cm depth and 100 cm SSD.

13. With the A14 chamber still in place in the water tank, position the chamber so that is bisected by the water surface.

14. Lower the chamber 0.6r (1.2 mm for the A14) and zero the crank tank.

15. Lower the chamber to 10 cm depth.

16. Beam on three times and record the values measured each time (in nC).

17. When the measurements are complete for the A 14 chamber, remove the ion chamber and replace it with the A12 ion chamber.

18. Position the chamber so the water surface bisects the chamber.

19. Lower the chamber 0.6r (1.8 mm for A12) and zero the crank tank.

20. Lower the chamber to 10 cm depth.

21. Beam on three times and record the values measured each time (in nC).

22. Using the cross-calibration and dose measurement Excel template input the necessary data to determine the dose per MU and the dose measured (in cGy).

C. Gafchromic™ EBT3 Film Calibration

1. While handling the Gafchromic™ film, wear gloves to limit that amount of oils and dust introduced to the surface of the film.

2. Determine the dose range needed for the calibration. For this study, the maximum dose calibrated is 350 MU (305.2 cGy).

3. Five film strips will be needed to complete the calibration.

4. Prepare the film by cutting five strips at least 1.5” x 8”, and mark the orientation of each film strip to ensure each film is exposed and scanned in the same orientation.

5. Each film strip will be exposed to a known dose. The known doses used for this calibration are:
    a. 0% of the maximum dose = 0 cGy = 0 MU
    b. 6.4% of the maximum dose = 20.056 cGy = 23 MU
    c. 16% of the maximum dose = 48.832 cGy = 56 MU
    d. 40% of the maximum dose = 122.08 cGy = 140 MU
    e. 100% of the maximum dose = 305.2 cGy = 350 MU

6. Label each film strip with the orientation, field size (10 x 10 cm^2), SSD (100 cm), time of exposure, and MU. An example of labeling is shown in the following figure:

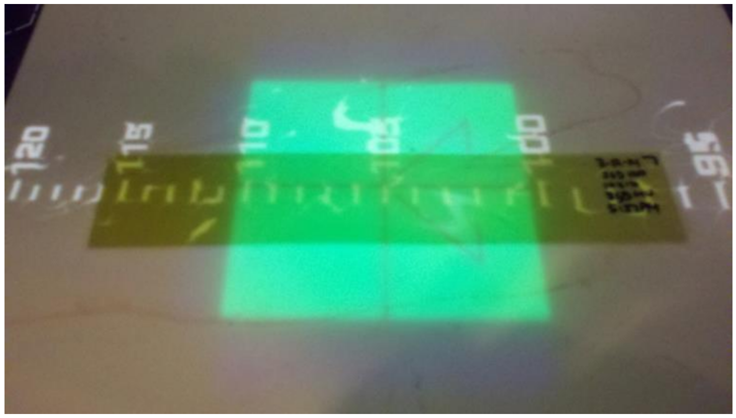

Figure 79: Film Strip Labeling

7. Place the first film in the center of the radiation field perpendicular to the beam on top of 10 cm of solid water.

8. Place 5 cm of solid water on top of the film, so the film is at 5 cm depth. The following figure shows the solid water set up:

Figure 80: Solid Water Setup for Calibration

9. Set the SSD to 100 cm and the field size to 10 x 10 cm^2.

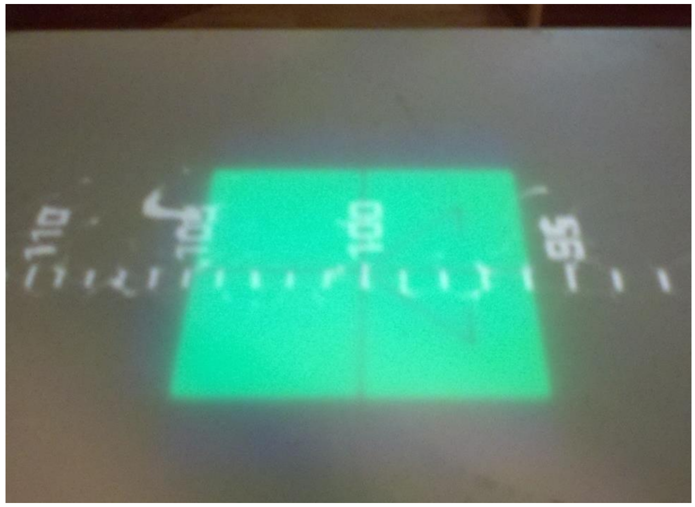

Figure 81: 100 cm SSD and 10 x 10 cm^2 Calibration Setup

10. Set the MU to the desired exposure and beam on.

11. Remove the film from the solid water sandwich, and position the next film.

12. Repeat steps 7 through 11 for each of the desired exposures.

13. Allow 24 hours for the film to develop before scanning.

14. When the necessary time has elapsed, turn on the Epson flatbed RGB scanner allowing a minimum of 30 minutes for warm-up.

15. Perform 7 warm-up scans to warm the lamps up.

16. When the scanner is warmed-up, ensure that the scanner configurations are correct with the color correction turned off.

17. Place the calibration film strips on the scanner as shown in the following figure:

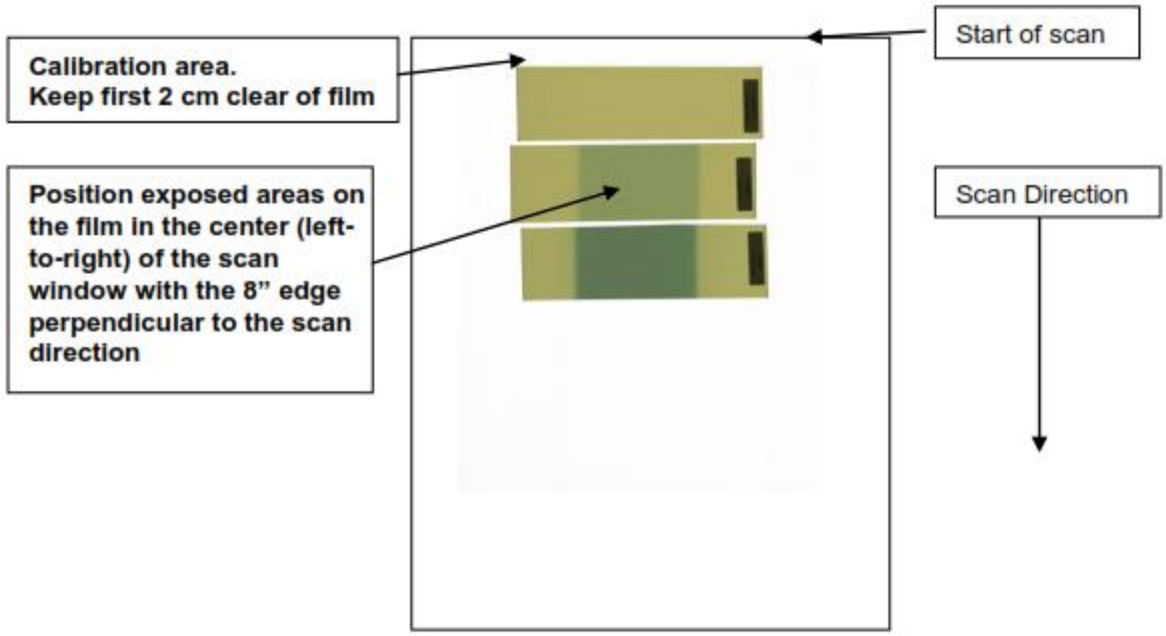

Figure 82: Film Placement on RGB Flatbed Scanner (Ashland 2014)

18. Open the FilmQA™ Pro software.

19. Open a new treatment, and select "Film Calibration (ordinary)" from the drop-down menu under "Case Object Management" as shown in following figure:

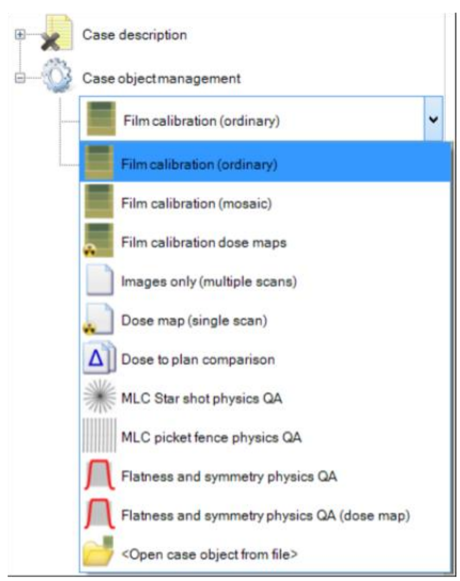

Figure 83: Selection of Film Calibration from Case Object Management (Ashland 2014)

20. Select and click the “Scan Image Calibration Film” by expanding the Film Calibration case object and right clicking on “Data Calibration Film (empty)”.

21. Once the scan is complete and the image is loaded in the FilmQA™ Pro application, use the Frame Tool to mark areas of interest in the center of the calibration film strips.

22. Select the calibration tool in the “Case data selector” as shown in the following figure:

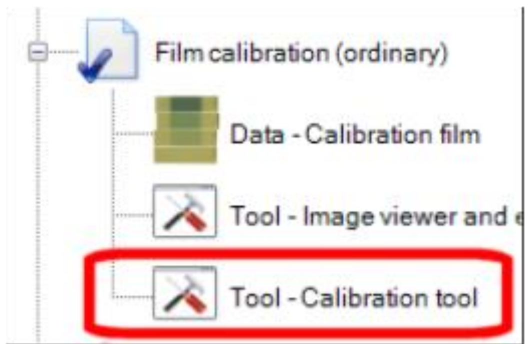

Figure 84: Tool-Calibration tool (Ashland 2014)

23. Following Figure 85 and 86, click the “123” icon on the bottom right corner (Figure 85). Then select the “Color reciprocal linear vs Dose” fitting function (Figure 86) and type in the corresponding dose values in the calibration table.

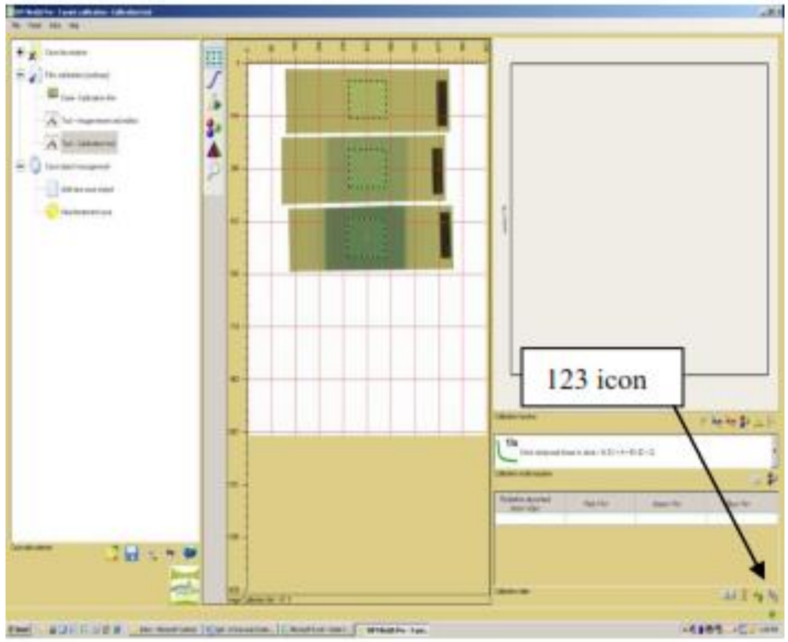

Figure 85: Screen Shot of 123 icon (Ashland 2014)

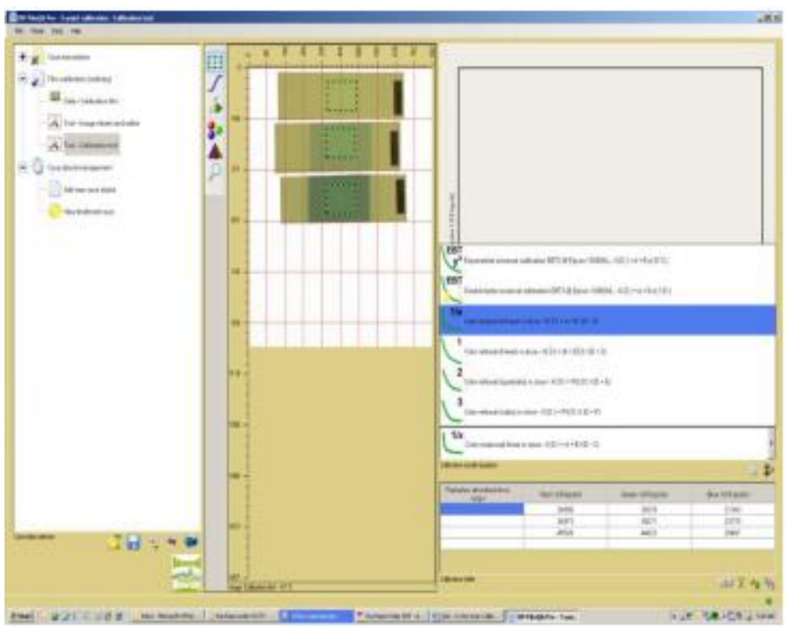

Figure 86: Fitting Function Selection (Ashland 2014)

24. Save the calibration by right clicking the “Film Calibration (ordinary)” data object and selecting “Save as fixed calibration” from the dropdown menu.

D. Stainless Steel and Titanium Rod Measurements with Gafchromic™ EBT3 Film

1. Position the solid water block in the crank tank and fill with water so the top surface of the solid water is at 5 cm depth in water. Ensure no air bubbles are trapped in the solid water block by tilting it in different directions.
    a. Record water temperature and room pressure

2. Place a strip of film between two halves of a ½" rod so it is perpendicular to the rod.

3. Tape the ½" rod together so it does not move or shift while placing it on the solid water block.

4. Place the taped ½" rod with film in the solid water slot. Ensure that the film lies as flat as possible on the solid water block (no gaps). Cerrobend weights may be needed to ensure the entire film remains flat on the solid water block and does not begin to float up at the ends.

5. Adjust the height of the couch so the SSD is 100 cm with a 10 X 10 cm^2 field size.

6. Beam on using 250 MU with the gantry at 0° (perpendicular to film).

7. After the first film measurement, remove the rod, untape it, and remove the film.

8. Label the film strip with the type of rod (SS or Ti), size of rod (1/2" or 1"), orientation, SSD, field size, MU, time taken, gantry position, energy (6X or 18X), and date.

9. Place a second film strip between the same ½" rod as in step 2 and 3.

10. Repeat step 4 with the second film.

11. Move the gantry to 85°.

12. Rotate the solid water block 90° and push it against the water tank closest to the gantry.

13. Set the SSD to the water tank to 100 cm (this will add about 1 cm of acrylic instead of just water and solid water). The surface interface of the 1” rods will be 10.9 cm, and the surface interface depth of the ½” rods will be 11.6 cm.

14. With the gantry at 85° (5° from parallel with film), beam on using 250 MU.

15. After the second measurement, remove the rod, untape it, and remove the film.

16. Label the film strip with the type of rod (SS or Ti), size of rod (1/2” or 1”), orientation, SSD, field size, MU, time taken, gantry position, energy (6X or 18X), and date.

17. With the other ½” rod, perform steps 2 through 14.

18. When the measurements with the ½” rods are completed, flip the top solid water block over to the side with the 1” slots. Ensure no air bubbles are trapped in the solid water block by tilting it in different directions.

19. Place a strip of film between the two halves of one of the 1” rods so it is perpendicular to the rod.

20. Tape the 1” rod together so it does not move or shift while placing it on the solid water block.

21. Place the taped 1” rod with film in the solid water slot. Ensure that the film lies as flat as possible on the solid water block (no gaps). Cerrobend weights may be needed to ensure the entire film remains flat on the solid water block and does not begin to float up at the ends.

22. Check that the SSD is still at 100 cm and field size is 10 X 10 cm^2.

23. Beam on using 250 MU with the gantry at 0° (perpendicular to the film).

24. After the first film measurement with the 1” rod, remove the rod, untape it, and remove the film.

25. Label the film strip with the type of rod (SS or Ti), size of rod (1/2” or 1”), orientation, SSD, field size, MU, time taken, gantry position, energy (6X or 18X) and date.

26. Place a second film strip between the same 1” rod as in step 17 and 18.

27. Repeat step 19 with the second 1” film.

28. Move the gantry to 85°.

29. Rotate the solid water block 90° and push it against the water tank closest to the gantry.

30. Set the SSD to the water tank to 100 cm (this will add about 1 cm of acrylic instead of just water and solid water). The surface interface of the 1” rods will be 10.9 cm, and the surface interface depth of the ½”” rods will be 11.6 cm.

31. With gantry at 85° (5° from parallel with film), beam on using 250 MU.

32. After the second 1” rod measurement, remove the rod, untape it, and remove the film.

33. Label the film strip with the type of rod (SS or Ti), size of rod (1/2” or 1”), orientation, SSD, field size, MU, time taken, gantry position, energy (6X or 18X) and date.

34. With the other 1” rod perform steps 17 through 29.

Images for Setup:

Figure 87: Setup for 0° Gantry

Figure 88: Setup for 85° Gantry

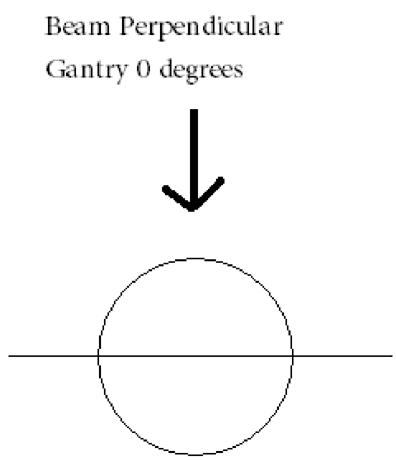

Figure 89: Setup for 0° Gantry

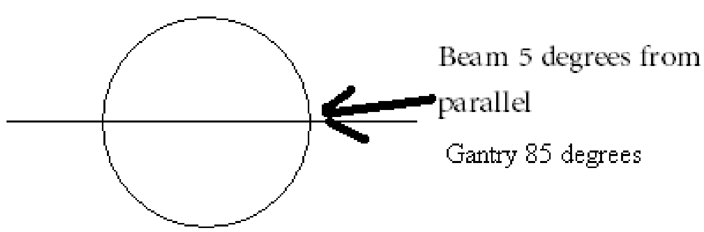

Figure 90: Setup for 85° Gantry

E. CT Simulation of Stainless Steel and Titanium Rods

1. Position the solid water block in the crank tank and fill with water so the top surface of the solid water is at 5 cm depth in water. Ensure no air bubbles are trapped in the solid water block by tilting it in different directions.

2. Position the water tank on the CT couch.

3. The solid water block should be positioned with the rod orientation perpendicular to the CT scanner. (similar orientation of the solid water block as in the 85° orientation)

Figure 91: Solid Water Block Positioning for CT

4. Align the lasers at the center of the 1” rod.

5. Position the couch to the most superior slice to be taken, and zero the couch.

6. Move the couch to the most inferior slice to be taken and note position.

7. At the CT simulation work station, start a new study.

8. Make it an anonymous study, and input the position (supine, head first), adult, and any comments about which rod (Ti quarter, SS quarter, Ti one, SS one).

9. Go to protocols and select Radiation Onco, Onco Chest.

10. Perform the scout scan.

11. Evaluate the scout. If unacceptable, go back and reposition the water tank.

12. If acceptable, move on to the actual scan.

13. Once the scan is complete, send a copy to Pinnacle[3] for planning.

14. Repeat steps 3 through 13 for the other 1” rod.

15. When the measurements with the 1” rods are completed, flip the top solid water block over to the side with the ½” slots. Ensure no air bubbles are trapped in the solid water block by tilting it in different directions.

16. Repeat steps 3 through 13 for each of the ½” rods.

F. Calculated Dose to Stainless Steel and Titanium Rods from Pinnacle[3]

1. Import the CT images to a new plan.

2. Select the correct CT to Density curve and accept.

3. Create a circular ROI (region of interest) contour that matches the rod diameter at one end of the rod.

4. Create an identical circular contour at the other end of the rod for the same ROI.

5. Interpolate the contour so the entire rod is contoured.

6. Create a rectangular ROI contour that encases the rod contour at one end of the rod.

7. Create and identical rectangular contour at the other end of the rod for the same ROI.

8. Interpolate the rectangular contour.

9. Create a density override for the area inside the rectangular ROI to the density of water (1.0 g/cm^3). Set the density override priority to 1.

10. Create a density override for the interior of the circular rod ROI to the density of either titanium (4.54 g/cm^3) or stainless steel (8.0 g/cm^3) depending on which rod CT being used. Set this density override priority to 2.

11. Create two POI's (point of interest) positioned directly at the edge (interface) of the rod contour at 5 cm depth (the center of the rod).

12. Create another POI farther away from the rod, but still within the dose region.

13. Create four trials to cover the four beam setups used:
    - Gantry 0, 6 MV
    - Gantry 85, 6 MV
    - Gantry 0, 18 MV
    - Gantry 85, 18 MV

14. For each trial, add a new beam with the correct parameters (field size, gantry position, etc.)

15. Set the prescription to 250 MU in one fraction.

16. Set the dose grid to encompass the dose region.

17. Calculate the dose for each trial.

18. Determine the interface dose from the POI's at the rod interface and the distant ambient field dose from the POI farther from the rod for comparison to film measurements.

19. Perform steps 1-18 for each of the four rods (1" SS, ½" SS, 1" Ti, and ½" Ti)

G. Hip Stem Film Setup and Measurements

1. Position the Tri Lock® hip stem with Gription® coating in the crank tank using the PVC stand and fill with water so the bisection point of the hip stem is at 5 cm depth in water, as shown in the following figure:

Figure 92: Tri Lock® Hip Stem PVC Stand

   Ensure no air bubbles are trapped on the porous coating of the hip stem. Check that the bisection surface is level with a level.

   a. Record water temperature and room pressure

2. Adjust the height of the couch so the SSD is 100 cm with a 10 X 10 cm^2 field size.

3. Place a strip of film cut to 5 x 10 cm^2 between two halves of the Tri Lock® hip stem so it is perpendicular to the rod. Also, ensure that the film is placed entirely within the Gription® coating on the hip stem, as shown in the following figure:

Figure 93: Tri Lock® Hip Stem Film Placement

4. Place a rubber band around the thin end of the Tri Lock® hip stem to hold the two pieces together during film measurements.

5. Position the couch so the hip stem and film are in the center of the field, as shown in the following figure:

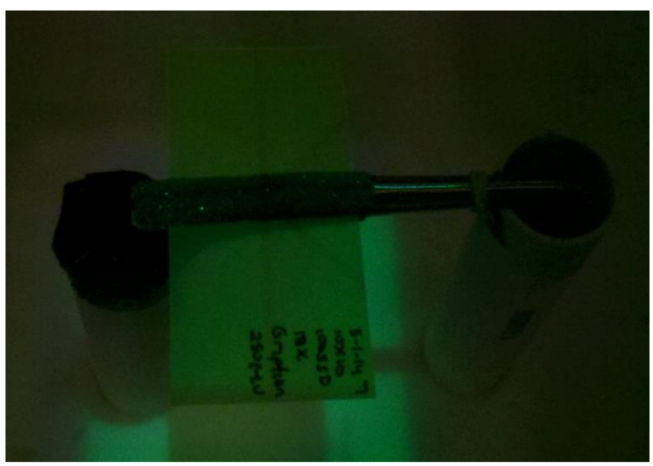

Figure 94: Tri Lock® Hip Stem Field Placement

6. Beam on using 250 MU with the gantry at 0° (perpendicular to film).

7. After the first film measurement, remove the film, dry it, and place it in the appropriate envelope for the designated processing time.

8. Label the film strip with the type of hip stem coating (Gription® or Porocoat®), orientation, SSD, field size, MU, energy (6X or 18X), and date. Also, record the time the film was taken to ensure the designated processing time passes before film analysis.

9. Place the second film strip in the same manner as steps 3 and 4.

10. Repeat steps 5 through 8 with the second film.

11. Remove the Tri Lock® hip stem and PVC stand, dry them, and place them in a safe storage space until the next set of measurements.

12. Position the AML® hip stem with Porocoat® coating in the crank tank using the PVC stand and fill with water so the bisection point of the hip stem is at 5 cm depth in water, as shown in the following figure:

Figure 95: AML® Hip Stem PVC Stand

Ensure no air bubbles are trapped on the porous coating of the hip stem. Check that the bisection surface is level with a level.

a. Record water temperature and room pressure

13. Check that the height of the couch remains at an SSD of 100 cm with a 10 X 10 cm^2 field size.

14. Place a strip of film cut to 5 x 10 cm^2 between two halves of the AML® hip stem so it is perpendicular to the rod. Also, ensure that the film is placed entirely within the Porocoat® coating on the hip stem, as shown in the following figure:

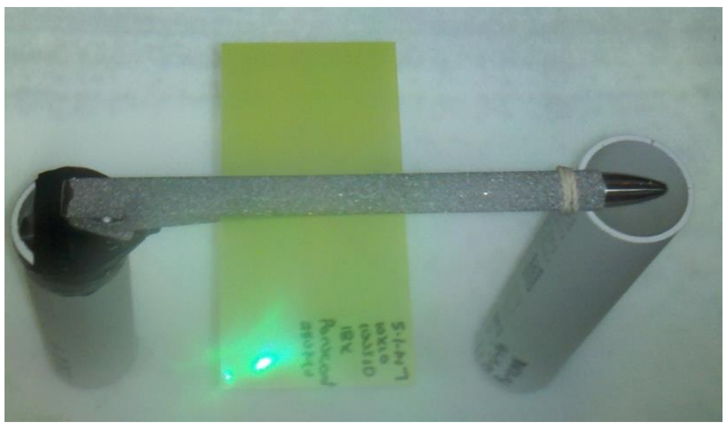

Figure 96: AML® Hip Stem Film Placement

15. Place a rubber band around the thin end of the AML® hip stem to hold the two pieces together during film measurements.

16. Position the couch so the hip stem and film are in the center of the field, as shown in the following figure:

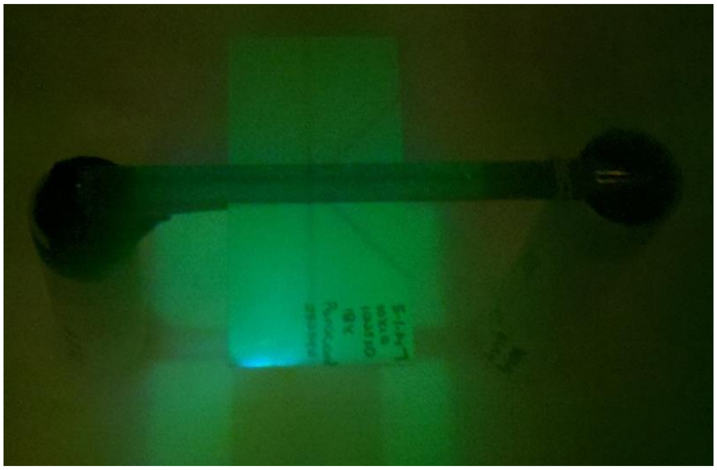

Figure 97: AML® Hip Stem Field Placement

17. Beam on using 250 MU with the gantry at 0° (perpendicular to film).

18. After the first film measurement, remove the film, dry it, and place it in the appropriate envelope for the designated processing time.

19. Label the film strip with the type of hip stem coating (Gription® or Porocoat®), orientation, SSD, field size, MU, energy (6X or 18X), and date. Also, record the time the film was taken to ensure the designated processing time passes before film analysis.

20. Place the second film strip in the same manner as steps 13 and 14.

21. Repeat steps 15 through 18 with the second film.

22. Remove the AML® hip stem and PVC stand, dry them, and place them in a safe storage space until the next set of measurements.